UNIVERSITY OF OKLAHOMA

GRADUATE COLLEGE

EXOTIC DIATOMIC MOLECULES OF CESIUM

A DISSERTATION

SUBMITTED TO THE GRADUATE FACULTY

in partial fullfillment of the requirements for the

Degree of

DOCTOR OF PHILOSOPHY

By

JONATHAN E. TALLANT
Norman, Oklahoma
2012

EXOTIC DIATOMIC MOLECULES OF CESIUM

A DISSERTATION APPROVED FOR THE
HOMER L. DODGE DEPARTMENT OF PHYSICS AND ASTRONOMY

BY

Dr. James P. Shaffer, Chair

Dr. Gregory Parker

Dr. Eric Abraham

Dr. Michael Morrison

Dr. Matthew Johnson

Dr. Charles Rice

This thesis is dedicated to my parents and to the loving memory of my brother, Douglas.

Acknowledgements

I would like to first acknowledge my advisor Dr. James Shaffer. Not only has he been a source of theoretical knowledge, his intuition for solving problems and his drive for solving them proved to be an invaluable skill for experiments and I hope it has rubbed off a bit. Second, I would like to acknowledge Dr. Arne Schwettmann. His sunny disposition always made the long hours in the lab more bearable and with his exhaustive knowledge of computational physics, he could always provide some direction when doing calculations. I would also like to thank my experimental comrade, Don Booth. Without his help on the experiment, progress would be a daunting task, barely conceivable with only one person. His skill set has rapidly improved and I know I have left the experiment in good hands. I would also like to thank Dr. Richard Overstreet for passing on the experimental baton and his skills to me. I would also like to thank Jon Sedlacek. Despite being on a different experiment in our lab, we share the same long hours and it has often been helpful bouncing ideas back and forth off of each other. Finally, I would like to thank Dr. Luis Gustavo Marcassa. One of the most helpful sentences that I heard in my graduate school tenure came from his mouth: "You must have a molasses..." I have accepted a post-doctoral position under his direction at the institute of physics at the University of São Paulo, in São Carlos, Brazil. I am looking forward to living in a new country doing research in the area of ultracold, heteronuclear molecules.

Table of Contents

List of Tables

List of Figures

Abstract

The observation of a new, polar class of homonuclear diatomic molecules, called trilobite molecules, is presented. The molecules have permanent electric dipole moments of $\sim 20 - 100$ Debye. The observations are in agreement with calculations carried out by our collaborators at the Institute of Theoretical Atomic, Molecular, and Optical Physics (ITAMP), at Harvard University. The unique mechanism that binds the molecules will be described. The molecules are not observable inside of a Magneto-Optical Trap (MOT) due to the low density of trapped atoms, $\sim 1 \times 10^{10}$ cm^{-3}. This thesis also describes the improvements to the apparatus in an effort to increase the density of trapped atoms. The improvements are two-fold. First, a system to slow an atomic beam using the Zeeman effect is described. The slowed atomic beam is used to load the MOT instead of from a background vapor, enhancing both the loading rate and the number of trapped atoms. A Monte Carlo simulation of the slowing process is presented. Second, an optical dipole trapping system has been developed and successfully implemented which captures atoms at a temperature of ~ 40 μK and at a density of $\sim 2 \times 10^{13}$ cm^{-3}. The increase in density augments two-body event rates by a factor of $\sim 4 \times 10^6$, and allows experiments to probe smaller interaction distances. This is demonstrated by the photoassociation of these exotic trilobite molecules.

Chapter 1

Introduction

1.1 Rydberg Atoms and Exotic Molecules

This thesis describes the observation of an exotic class of diatomic molecules called trilobite molecules. These homonuclear diatomic molecules uncharacteristically have giant permanent electric dipole moments and are bound by a unique mechanism. For this binding mechanism to function, the diatomic molecule needs to consist of a ground state atom and a highly excited atom called a Rydberg atom. The low-energy scattering of the excited Rydberg atom electron off of the ground state atom leads to a molecular bond. These molecular bonds are extremely weak, ~ 100 MHz (~ 500 neV). Accordingly, ultracold environments, $\sim \mu$K, are required to observe the molecules. The trilobite molecules observed in this thesis are created from an optically trapped sample of ground state cesium atoms at relatively high density ($\sim 2 \times 10^{13}$ cm^{-3}) and low temperatures, ~ 40 μK. This work is an extension of our group's previous studies on ultracold atomic and molecular systems containing cesium Rydberg atoms.

Rydberg atoms are atoms whose valence electron is in a highly excited state, or has a large principal quantum number, n. The general interest in Rydberg atoms stems from the fact that the highly excited electron gives the atom exaggerated properties [1]. Because the electron is far away from the remaining

core, important atomic properties of Rydberg states, such as lifetimes and polarizabilities, scale with n. Also, the large separation between the electron and the core make the electron very sensitive to external perturbations. This makes Rydberg atoms ideal candidates for manipulation with external fields. Coupled with more recent advances in ultracold technology, Rydberg atoms have opened up major areas of research such as quantum information processing [2, 3, 4, 5], and quantum electrodynamics with resonant cavities [6, 7]. Entanglement of mesoscopic quantum systems was finally achieved using Rydberg states [8]. Rydberg atoms can be also used as sensitive experimental tests of theoretical predictions to high accuracy. These range from experimental verification of radiative and blackbody lifetimes [9, 10, 11] to an experimental verification of the existence of a quantized vacuum field [12].

Earlier theoretical work from this group addressed the physics of Rydberg atoms and, in particular, how pairs of ultracold Rydberg atoms interact [13]. We used the theory to accurately predict a kinetic energy gain of a photoinitiated Rydberg atom collision within a magneto-optical trap (MOT), which was measured by our group [14]. The theory also suggested that application of small electric fields could give rise to potential wells at very large, $\sim \mu$m size, distances and that the wells support hundreds of bound states [15]. These exotic "macrodimer" molecular states were then observed by our group in 2009 [16]. The observed macrodimers were bound at extremely large distances, 3 μm - 9 μm, due to interatomic multipolar forces and a background electric field. Because

these molecules are bound at such large distances, they can be created from samples with a relatively small density, $\rho \sim 10^{10}$ cm^{-3}.

The average interatomic spacing, d, of particles with a uniform density can be estimated by $d \sim \rho^{-1/3}$. With typical MOT densities near 1×10^{10} cm^{-3}, the average atomic spacing inside the MOT is $d \sim 5$ μm [17]. This means the probability for a pair of atoms to be within the bonding distance for macrodimer formation is almost unity. The constituents of the trilobite molecules observed in this thesis interact at much smaller distances, ~ 50 nm. This distance is two orders of magnitude larger than the average interatomic spacing in the MOT, so there are almost no pairs of atoms available at this range. The obvious solution to access smaller interaction distances is to increase the initial available density. While it may be straightforward to say, achieving a higher density poses a significant experimental challenge and a large portion of this thesis focuses on the improvements to the apparatus required to do so.

Trilobite molecules have a very unique binding mechanism. This binding mechanism results from the scattering of the Rydberg atom electron off of the ground state atom, see Fig. 1.1. Because the Rydberg atom is so much larger than the ground state atom, the force between the two is largely dominated by interaction of the Rydberg atom electron and the ground state atom and can be described in the context of electron-neutral atom scattering. Low-energy electron scattering off of neutral atoms is an old problem. Its theoretical description first appeared in 1934 by E. Fermi [18]. Fermi described the observed shift of

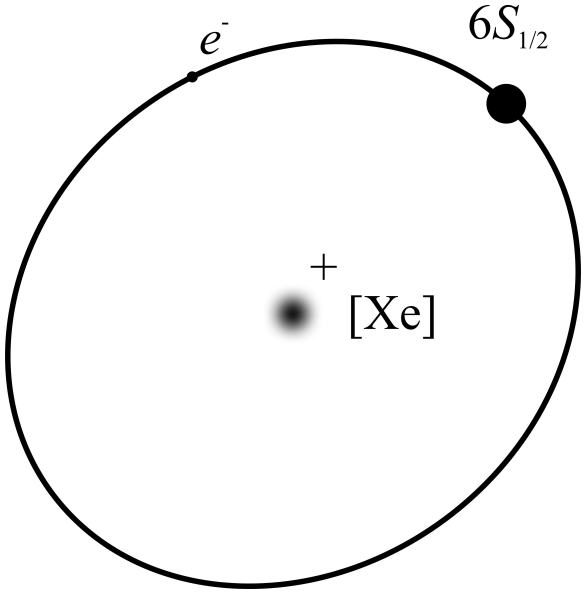

Figure 1.1: A ground state $6S_{1/2}$ cesium atom in the orbit of a cesium Rydberg atom. The remaining core is isoelectronic with xenon.

spectral lines of excited alkali gases due to the presence of other gases at high pressures. He introduced the concept of a scattering length to explain why the sign of the shift depended on the species of foreign gas. Furthermore, due to the frequent scattering of the electron off of the foreign gas particle, the interaction could be described as a mean-field potential whose sign depended on the sign of the scattering length: negative scattering lengths lead to attractive interactions. Using these ideas, Omont further worked out the details of the interaction of Rydberg states with neutral particles in 1977 [19]. By this time, it was already realized that ground state atoms could be bound to Rydberg atoms by this electron scattering mechanism, but the bonds are so weak, it was hard to imagine an experiment that could observe them. After the birth of laser cooling led to

Bose-Einstein condensation in 1995 [20, 21], Omont's work was re-examined by Greene *et al.* in 2000. The authors realized that the newly accessible regimes of density and temperature provided a unique opportunity to exploit this bonding mechanism. They predicted that two classes of these exotic molecules could be formed by this mechanism, polar and non-polar molecules. The non-polar variety contain Rydberg atoms of low angular momentum character, $l < 3$, and the polar class involves Rydberg states of high angular momentum character, $l \geq 3$, so-called trilobite molecules. The polar class of molecules were predicted to have huge permanent dipole moments in the 1 kD range (1 D$\sim 3.34 \times 10^{-30}$ C·m), which make them amenable to electric field manipulation.

In 2009, molecules belonging to the non-polar class were observed in the rubidium system with $l = 0$ [22]. Two years later it was demonstrated experimentally and theoretically that these molecules actually had a small permanent dipole moment of ~ 1 D [23]. The key ingredient in formation of the permanent dipole moment is the accidental degeneracy of the rubidium nS Rydberg states with $(n-3)l$ hydrogenic states. The near-degeneracy leads to a mixing of the high angular momentum states with the parent nS Rydberg state. The mixing of these hydrogenic states leads to the development of a permanent dipole moment [24].

The cesium trilobite states observed in this thesis are different from the rubidium trilobite states for several reasons. First, the $e^- + \mathrm{Cs}(6s)$ system has a

resonance belonging to the $6s6p$ state which is only 8.0 meV above $6S_{1/2}$ [25]. This resonance affects the positions of the potential wells so the observed trilobite states provide indirect evidence of its location. Second, the hydrogenic manifold of high-l states is closer to the nS threshold in cesium compared to rubidium. This causes more of the states to interact with each other and produces avoided crossings between them, producing wells *above* the nS thresholds. Finally, these trilobite states asymptotically correspond to states with high angular momentum, $l > 3$. This leads to the formation of giant permanent dipole moments ~ 2 orders of magnitude higher than the rubidium case. Homonuclear diatomic molecules have symmetry that normally precludes the existence of a permanent dipole moment. These exotic homonuclear diatomic molecules have permanent electric dipole moments $\sim 20 - 100$ D, which should be contrasted to that of sodium chloride, with a permanent dipole moment of 9 D. Understanding how to create these molecules serves as a benchmark for future experiments which exploit their giant dipole moments. Furthermore, understanding how these molecules decay can give insight into other exotic states of matter such as ion pair states.

1.2 Thesis Organization

This thesis is organized as follows. In Chapter 2, the theoretical principles of major laser cooling and trapping experimental techniques used in this thesis are explained. Magneto-optical traps (MOTs) and far-off resonance traps (FORTs)

are theoretically described as well as Zeeman slowing of an atomic beam. A Monte Carlo simulation of the Zeeman slowing process is also presented. Chapter 3 discusses the experimental apparatus. The cesium ovens and vacuum systems for the main chamber and the Zeeman slower are described. The time-of-flight spectrometer used for generation and detection of ions is described as well as the quadrupole-field switching circuit used to control the current in the MOT coils. The home-built diode laser systems and tapered amplifier design are also presented in Chapter 3. Chapter 3 ends with a description of the construction details for the Zeeman slower and FORT, including the alignment procedure used to overlap the FORT and MOT. Rydberg atoms are explained theoretically in Chapter 4 including an experiment that uses Rydberg atoms to determine the velocity resolution of our time-of-flight spectrometer. Photoionization of Rydberg atoms is discussed in Chapter 5. The theoretical principles leading to the decrease in lifetime of the Rydberg state due to photoionization are presented. Chapter 5 also describes an experiment that systematically measures Rydberg atom lifetimes with and without the presence of the photoionizing FORT beam. The observation of cesium trilobite states is the main result of this thesis and is described in Chapter 6. The unique binding mechanism is described theoretically and the experiment carried out to observe the molecules is explained. The experimental observations are compared to theoretical calculations from collaborators at the Institute for Theoretical Atomic, Molecular, and Optical Physics (ITAMP), at Harvard University. Following Chapter 6, the main body

of the thesis is concluded with a look toward future directions in Chapter 7. The details of a two-level atom in the presence of an electromagnetic radiation field are presented in Appendix A. The Mathematica code used to run the Monte Carlo simulation of the Zeeman slowing process is reproduced in Appendix B. Finally, a list of peer-reviewed journal publications as well as a list of presentations to which I contributed is given in Appendix C.

Chapter 2

The Experimentalist's Toolbox: A Theoretical Introduction

2.1 The Magneto-Optical Trap

2.1.1 Introduction

The magneto-optical trap (MOT) has often been called the workhorse of atomic physics. The MOT is a hybrid trap for neutral atoms which relies on optical forces and an inhomogeneous magnetic field to trap the atoms. The MOT is of practical use in the laboratory for a variety of reasons. The trapping ability afforded by the MOT is robust, allowing capture of billions of neutral atoms even from a room temperature vapor [17]. The MOT can therefore also serve as a reservoir of cold atoms with which to load traps having lower trapping potentials. While construction of a MOT is challenging, the technology is well-known and many resources exist to research construction details (see, for example, [17] and references therein). The demands on laser power are small and the required magnetic field gradients are easily achievable. The lasers used for most alkalis (Rb and Cs being amongst the most popular) are inexpensive and can function quite well with relatively simple designs and circuitry. A functioning magneto-optical trap relies on relatively simple theoretical mechanisms, which are described in the next section.

2.1.2 Radiation Pressure and Optical Molasses

Upon absorption of a photon with wavevector $\mathbf{k}$, particles receive a momentum kick of magnitude $\hbar k$ in the direction the photon was traveling. Spontaneous emission of the photon, however, is in a random direction. If a directed beam of photons is used and the process of absorption and emission is repeated several times, the net effect is to put a force on the particles in the direction of the beam. The force is distributed over the surface area of the beam of photons, so this effect is often called *radiation pressure*. The quantitative features of this force may be illuminated by examining a two-level atom in the presence of a laser field (see Appendix A). As shown in Appendix A, the steady-state solutions of the optical Bloch equations yield equilibrium populations in the ground and excited states (see Eq. A.25). The excited state population, ρ_{ee}, may be rewritten by defining the on-resonance saturation parameter, $s_0 = 2\Omega^2/\Gamma^2$, where Ω is the Rabi frequency and Γ is the natural linewidth of the excited state. The excited state population is now given by

$$\rho_{ee} = \frac{s_0/2}{1 + s_0 + (2\delta/\Gamma)^2}, \tag{2.1}$$

where δ is the detuning of the laser frequency from the atomic transition frequency. An atom absorbs photons at the rate $\Gamma\rho_{ee}$, each with momentum of $\hbar k$ so that the force from the laser beam is simply $F = \hbar k\Gamma\rho_{ee}$. If the atom has a velocity, v, the doppler shift must be taken into account by making the replacement $\delta \to \delta - \mathbf{k}\cdot\mathbf{v}$. The force from a single beam on the two level atom is then given

by

$$F = \hbar k \Gamma \frac{s_0/2}{1 + s_0 + (2(\delta - \mathbf{k} \cdot \mathbf{v})/\Gamma)^2}. \tag{2.2}$$

Opposing forces on the atom may be arranged by using a mirror to retroreflect the laser beam. In this case, the forces add and expanding the total force in (kv/Γ) gives

$$\mathbf{F}_{tot} \simeq \frac{8\hbar k^2 \delta s_0 \mathbf{v}}{\Gamma(1 + s_0 + (2\delta/\Gamma)^2)^2} + \mathcal{O}(kv/\Gamma)^4. \tag{2.3}$$

For small velocities, this force is proportional to the velocity and the sign of the force is determined by the sign of the detuning. If the laser detuning is negative (red detuning), the force opposes atomic motion much like friction. This effect of viscous damping led to the term *optical molasses*. If the atom is exposed to near-resonant light from a laser with a linewidth smaller than Γ, the atomic motion is rapidly damped to very small velocities. This notion of using near-resonant laser light to cool atoms is now nearly 40 years old [26, 27].

An optical molasses obviously cannot be used to cool atoms to zero velocity. In addition to cooling the atoms down, the photons also cause heating. The heating is caused by recoil of the atom from the momentum changes associated with absorption and emission. To find the equilibrium temperature of atoms in an optical molasses we can equate the heating and the cooling rates caused by the laser beams. The cooling rate is given by $\mathbf{F}_{tot} \cdot \mathbf{v}$. Heating occurs at the rate 2Γ due to the two opposing beams. When the atom absorbs a photon, it experiences a momentum change $\hbar k$ and a corresponding kinetic energy change

of $(\hbar k)^2/2M = \hbar\omega_r$. The energy removed from the field is then increased by $\hbar\omega_r$. The opposite is true for the emitted photon, with average energy returned to the field decreased by $\hbar\omega_r$. The average loss of energy from the light field is thus $2\hbar\omega_r$. The heating rate is then $4\hbar\omega_r\Gamma$. The equilibrium kinetic energy has a minimum at $\delta = -\Gamma/2$ and its temperature equivalent is given by $T_D = \hbar\Gamma/2k_B$, where k_B is Boltzmann's constant. T_D is called the Doppler temperature and $T_D = 125$ μK for Cs [17]. The Doppler temperature limit is easily overcome with polarization-gradient cooling methods [28, 29, 30]. Temperatures of tens of μK are readily achieved in the laboratory using polarization-gradient cooling. While the atoms are viscously confined within the optical molasses region, they are not localized in space at high density. To trap the atoms, a restoring force around some center is required. This is provided by an inhomogeneous magnetic field, whose field strength is linearly dependent on the displacement from the center. The details of how this provides a restoring force is given in the next section.

2.1.3 Magnetic Field and Laser Polarization Dependence

The magnetic field for the MOT is produced by two coils arranged in anti-Helmholtz configuration. At the geometric center of this configuration the magnetic field is zero. As indicated in Fig. 2.1, the magnetic field increases linearly away from the center with the field lines always pointing toward the center. In the presence of the magnetic field, B, the atomic levels experience

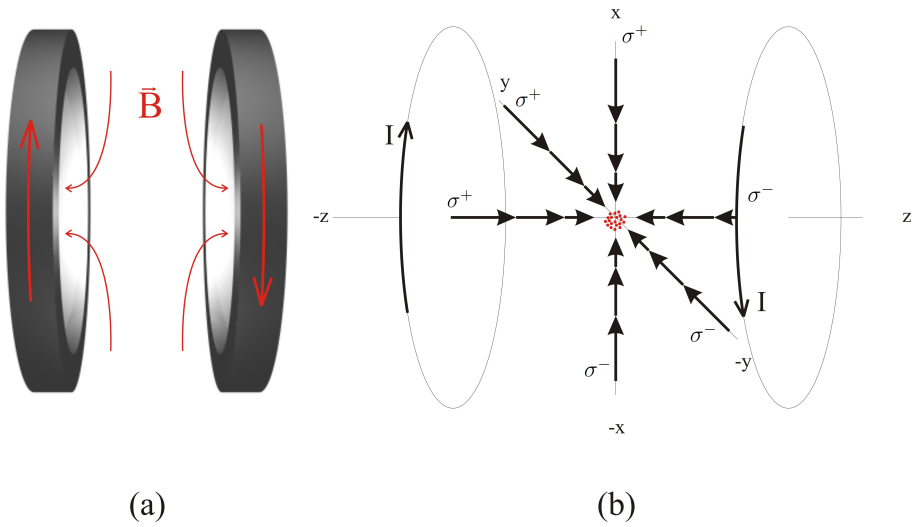

Figure 2.1: (a) Coils arranged in anti-Helmholtz configuration. (b) Arrangement needed for a MOT. The polarizations for each axis are shown. The arrows represent the magnetic field strength.

state-dependent Zeeman shifts. The energies are shifted by an amount

$$E = g_F \mu_B m_F B, \tag{2.4}$$

where F is the total angular momentum (including nuclear spin), m_F is the magnetic sublevel, and μ_B is the Bohr magneton. To understand the effect of the magnetic field, we consider an atom with zero angular momentum in the ground state and one unit of angular momentum in the excited state. The magnetic field shifts the energy of the excited states according to Eq. 2.4, so the shift is linear with distance from the center. For an atom placed at $z < 0$ (see Fig. 2.2), the excited $m_F = 1$ state is closer to resonance with the red detuned laser than the $m_F = -1$ state. Since the atom is in the ground ($m_F = 0$) state, a

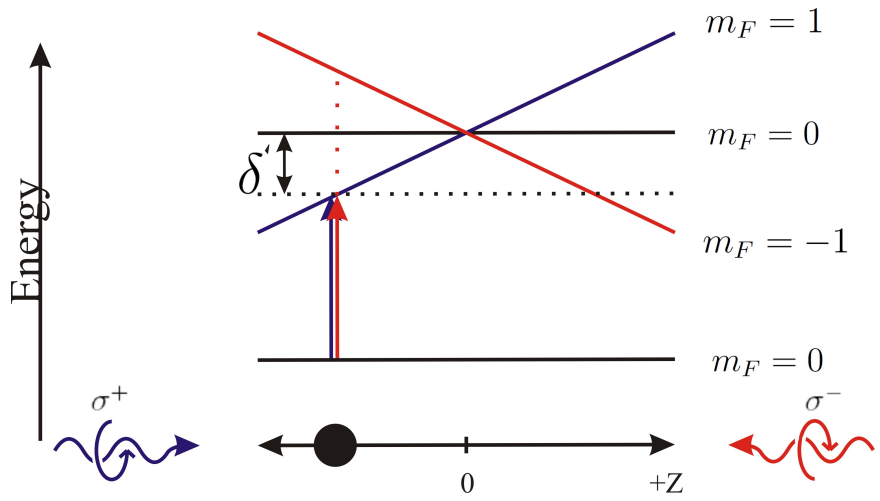

Figure 2.2: An energy diagram of the magneto-optic trap. The atom (located at $z < 0$) is assumed make $F = 0 \rightarrow F' = 1$ transitions. The detuning, δ', is the total laser detuning experienced by the atom. It includes the Zeeman and Doppler shifts; $\delta' = \delta \mp \mathbf{k} \cdot \mathbf{v} \pm \mu' B/\hbar$. μ' is the effective magnetic moment for the transition.

beam with σ^+ polarization ($\Delta m = 1$ transitions) is absorbed more readily and a beam with σ^- polarization. If the beam coming from $z < 0$ has σ^+ and the counterpropagating beam has σ^- polarization, a difference in radiation pressure is generated that always pushes the atom towards $z = 0$. The cloud of atoms is then compressed into a dense region around the magnetic field zero, creating a magneto-optical trap, or MOT. We can find the restoring force of the MOT by examining Eq. 2.3 for stationary atoms. The magnetic field causes an effective detuning of $\delta' = \delta \pm \mu' B/\hbar$, where μ' is the effective magnetic moment of the transition. If we consider the magnetic field along the z axis of Fig. 2.1 to be

$B(z) = B_0 z$, the detuning along the $\pm z$ axis is given by $\delta \pm \mu' B_0 z/\hbar$. The force may be expanded about $z = 0$ to obtain

$$F_z = \frac{\mu' B_0}{\hbar k} \frac{8\hbar k \delta s_0}{\Gamma \left(1 + s_0 + (2\delta/\Gamma)^2\right)^2} z. \tag{2.5}$$

This force also depends on the sign of the detuning and is a restoring force for red detunings. The MOT can therefore be attributed a harmonic potential energy.

$$U(z) = \frac{1}{2}\kappa z^2, \tag{2.6}$$

where $F_z = -\kappa z$ in Eq. 2.5. It should be noted that the magnetic field gradient along the other two axes are half as large as the z gradient, so that the restoring force along those directions is also half as large. This leads to an elongated trapping potential energy surface that is compressed along the z axis. The trap depth of the MOT, or trap potential in temperature units, can be several hundred mK allowing capture of many atoms from the background vapor.

2.2 Zeeman Slowing of an Atomic Beam

2.2.1 Introduction

For a MOT to function, the 3D region of optical molasses must be able to cool the atoms. Because most thermal atoms have high velocities, their Doppler shifts are hundreds of MHz, which is large enough to shift the molasses beams completely out of resonance. This means that the molasses only functions for those atoms

whose velocity is small enough. The natural linewidth of the transition selects an approximate maximum velocity with which the atoms may be captured and cooled by the molasses beams, $kv \sim \Gamma$, $v \sim 4.5$ m s^{-1} for Cs. The number of atoms this represents is described by a Maxwell-Boltzmann distribution. The probability distribution function for a Maxwell-Boltzmann distribution of speeds as a function of temperature is given by

$$f(v,T) = 4\pi \left(\frac{m}{2\pi k_B T}\right)^{3/2} v^2 e^{\left(\frac{-mv^2}{2k_B T}\right)}, \tag{2.7}$$

where m is the atomic mass (133 a.u. for cesium), and k_B is Boltzmann's constant. All of the atoms are contained in the distribution so $\int_0^\infty f(v)dv = 1$, but only $9.5 \times 10^{-4}\%$ of the atoms are moving 4.5 m s^{-1} or slower at room temperature. This means the overwhelming majority of the atoms in the molasses region cannot be captured by the beams and, therefore, lead to collisions with atoms that can. This can be overcome by loading the MOT from an atomic beam rather than background vapor. This has two advantages. First, the background pressure is lowered so trapped atom lifetimes are increased. Second, the loading rate of atoms into the MOT can be greatly increased. Both effects lead to higher steady-state atom numbers. In the following sections, generation of the atomic beam will be discussed followed by our selected method of slowing the beam: Zeeman slowing.

2.2.2 Atomic Beam Generation

A significant vapor pressure of the alkali metals may be developed by heating the solid metal near its melting point. The low melting point of cesium (28.5 ^{o}C [31]), affords significant vapor pressure even at room temperature. The vapor pressure, P_v, as a function of temperature may be calculated in the solid and liquid phases as [31]

$$\begin{aligned} \log_{10} P_v &= 2.881 + 4.711 - \frac{3999}{T} \quad \text{(solid)} \\ \log_{10} P_v &= 2.881 + 4.165 - \frac{3830}{T} \quad \text{(liquid)}. \end{aligned} \tag{2.8}$$

The vapor pressure is in Torr. The number density of cesium atoms in a container may then simply be calculated from the ideal gas law.

$$n_0 = \frac{P}{k_B T} \tag{2.9}$$

If a hole is introduced into the container of cesium, the atoms will leak out of the hole into a region of lower pressure. The mean-free-path of the atoms is related to the density and collision cross section through the relationship

$$\lambda_{mf} = \frac{1}{\sqrt{2}\sigma n_0}. \tag{2.10}$$

The cesium atoms have a mean-free path of several meters for the temperatures and pressures used in this thesis [32], which is much larger than the size of the oven. The oven is therefore operating in the effusive limit, where the cesium atoms are much more likely to collide with a piece of apparatus before another cesium atom.

The flux of atoms out of the aperture, Φ, may be calculated once the density and the average velocity of the atoms are known. The average velocity of the atoms is related to their temperature by

$$v_{ave} = \sqrt{\frac{8k_BT}{\pi m}}. \tag{2.11}$$

Note this is also just $\int_0^\infty vf(v)dv$, using the speed distribution function in Eq. 2.7. The flux out of the aperture is then calculated by [33]

$$\Phi = \frac{1}{4}n_0 v_{ave}. \tag{2.12}$$

The rate at which the number of atoms, N, leave the oven aperture is given by

$$\dot{N} = \Phi A_a, \tag{2.13}$$

where A_a is the area of the aperture. Atoms exiting the aperture in this way will have directions θ, and ϕ, and speed v, such that their rate can be determined by [33]

$$d\dot{N}_{v,\theta,\phi} = \frac{n_0 A_a}{\pi^{3/2}\alpha^3}\, v\, e^{-v^2/\alpha^2} \cos\theta\, v^2 \sin\theta dv d\theta d\phi, \tag{2.14}$$

where $\alpha = \sqrt{2kBT/m}$. The directions are generally distributed over the hemisphere opposite the oven. When loading the MOT from a vapor cell, this is certainly true and atoms are far more likely to hit the walls before drifting into the trapping (molasses) region. If a second aperture is placed further downstream from an oven, the ranges of θ and ϕ can be severely restricted. The atoms exiting the second aperture form an atomic beam, which is highly directional. The

atomic beam has natural cylindrical symmetry. Transforming Eq. 2.14 into cylindrical coordinates yields

$$d\dot{N}_{v_r,v_z} = \frac{2n_0 A_a}{\pi^{1/2}\alpha^3}\, v_r\, e^{-v_r^2/\alpha^2}\, v_z\, e^{-v_z^2/\alpha^2} dv_r dv_z, \tag{2.15}$$

where v_r and v_z are the speeds in the radial and axial directions of the beam, respectively. Integration of Eq. 2.15 yields a loading rate, R, of the atoms due to the atomic beam.

$$R = \dot{N}\left(1 - e^{-v_{z,max}^2/\alpha^2}\right)\left(1 - e^{-v_{r,max}^2/\alpha^2}\right) \tag{2.16}$$

The steady-state number of atoms may be computed by the ratio of the loading and the loss rates. In the vapor cell, the loss rate is relatively high because of the necessary high background pressure required to create many low-velocity atoms capable of capture by the molasses. This loss rate is significantly reduced by using an atomic beam because a significant fraction of all of the atoms in the beam can be slowed. This combined with the high directionality of the atomic beam greatly reduces the background pressure. This means if the loading rate from the atomic beam is even within an order of magnitude of the loading rate from the background vapor, MOTs with substantially higher atom numbers may be generated. The effect of slowing the atoms can be seen in the first exponential term of Eq. 2.16. If $v_{z,max}$ is made large, the loading rate also gets large. The size of the apertures and the distance between them define a maximum v_r, but the ranges of v_z are completely determined by the slowing process, which is considered in the next section.

2.2.3 Zeeman Slowing

The main focus of cooling an atomic beam relies on radiation pressure from a counterpropagating laser beam. The idea is to keep the atomic transition frequency in resonance with the counterpropagating beam at all points along the beam. This is complicated by the fact that the atoms see a varying Doppler shift as they scatter resonant photons. There are several methods of overcoming this difficulty. The frequency of the counterpropagating laser may be changed (*chirping*) to compensate for the change in the Doppler shift. This "chirped slowing" can efficiently be done by use of RF electronics [34], but pulses of slowed atoms are produced rather than a continuous beam. This chirped slowing method was extended by Ketterle *et al.* [35], where the angle between the atomic beam and laser beam was varied instead of the laser frequency. Since this was done with isotropic light, a continuous beam was generated. Continuous atomic beams can also be generated if external fields are used to tune the atomic transition frequency instead of tuning the compensation for the Doppler shift. This has been done in the context of electric fields (Stark slowing) [36] and with magnetic fields (Zeeman slowing) [37]. Because the demands on electrical power can be very high for Stark slowers, we chose to design a Zeeman slower.

The basic idea of Zeeman slowing is to use a spatially varying magnetic field such that the atomic resonance frequency is changed to match the changing Doppler shift as the atoms travel along the atomic beam. According to Eq. 2.4, a

change in m_F is required to change the energy. This means circular polarizations must be used to drive transitions. Two complimentary methods of slowing are used involving orthogonal circular polarizations of laser light [37, 38]. The Zeeman shifts of the stretched states of the D2 transition in cesium are shown in Fig. 2.3, showing the states connected by the polarizations of light. The states

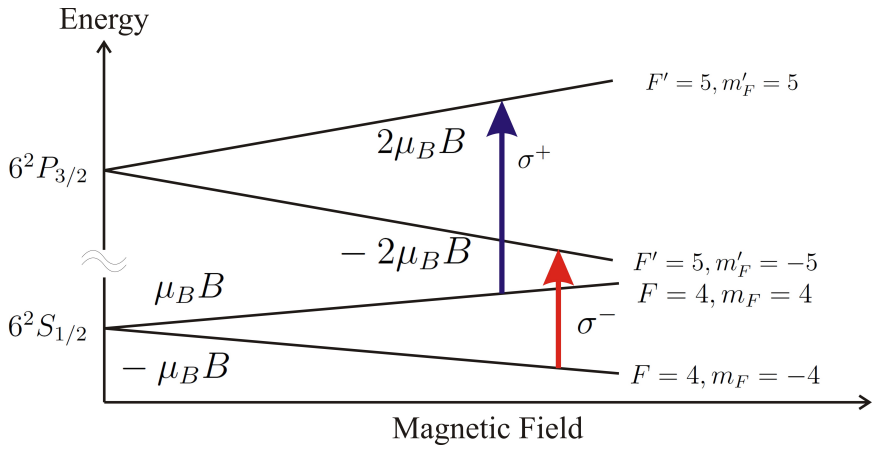

Figure 2.3: Zeeman shifts of the stretched states of the D2 transition in cesium.

connected by σ^+ polarization have a separation that increases with magnetic field as $\Delta E_{\sigma^+} = \mu_B B$, whereas the states connected by σ^- polarization similarly decrease with magnetic field. The fundamental difference in the two choices of polarizations is that σ^+ light must use a decreasing magnetic field to compensate for a decreasing Doppler shift and σ^- must use an increasing magnetic field. The Zeeman slower construction outlined in this thesis is designed for σ^- polarization, so I will focus on the theoretical aspects concerning this polarization, but the results are extendable to σ^+ Zeeman slowers.

In a σ^- Zeeman slower, the resonance condition leading to maximum decel-

eration is $\delta + \mathbf{k} \cdot \mathbf{v} + \mu_B B(z)/\hbar = 0$. Solving for the magnetic field, we arrive at

$$B(z) = \frac{\hbar}{\mu_B} \left(\delta - kv(z)\right). \tag{2.17}$$

This magnetic field assumes constant resonance with the field, which therefore assumes constant (maximum) acceleration provided by the scattering force of Eq. 2.3.

$$a = \frac{\hbar k \Gamma}{2m} \frac{s_0}{1 + s_0 + 4\left(\delta + kv + \mu_B B(z)/\hbar\right)^2/\Gamma^2} \tag{2.18}$$

The maximum acceleration on resonance is then given as

$$a_{max} = \frac{\hbar k \Gamma}{2m} \frac{s_0}{1 + s_0}. \tag{2.19}$$

Simple kinematic equations may then be used to solve for $v(z)$ in terms of the initial velocity of the atoms, v_0.

$$\begin{aligned} v^2(z) &= v_0^2 + 2a_{max}z \\ v(z) &= v_0\sqrt{1 - z/z_0} \end{aligned} \tag{2.20}$$

where $z_0 = v_0^2/2a_{max}$ is the distance required to stop the atoms at this acceleration and is called the *slower length*. For atoms to exit the slower, the acceleration must be some fraction of the maximum, $a_{max} = ca_s$, where now a_s is the designed acceleration of the slower and $c < 1$. This means the previous resonance condition is shifted by an amount Δ placing the new resonance velocity at Δ/k, see Fig. 2.4. Including the extra detuning, Δ, to the magnetic field expression Eq. 2.17, and using the velocity in Eq. 2.20, we arrive at the following expression for the

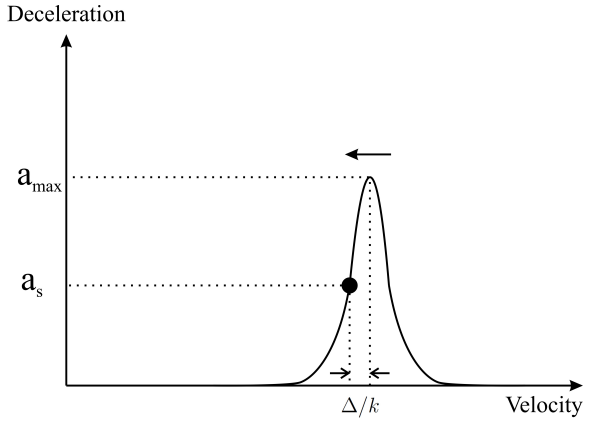

Figure 2.4: Atomic deceleration as a function of velocity. The atom maintains a constant deceleration a_s as the atom is slowed to lower and lower velocities.

ideal magnetic field profile for the Zeeman slower.

$$B(z) = B_b - B_t\sqrt{1 - z/z_0} \tag{2.21}$$

The bias-field is given by $B_b = -\hbar/\mu_B(\delta + \Delta)$ and the taper-field is given by $B_t = \hbar k v_0/\mu_B$. To simulate the slowing process, the ideal field of Eq. 2.21 is used in the acceleration given by Eq. 2.18, and the classical equations of motion can be solved. To fully simulate the slowing, a Monte Carlo simulation was created that allows determination of the optimum slowing profile parameters.

2.2.4 Slowing Efficiency Simulation

Determining the relevant slowing parameters was an iterative process. Three important calculations were required to simulate the successful slowing of atoms. First, a simplified 1D calculation was used to hone in on the correct values of

the bias and taper fields. Second, a program was generated that determines the winding pattern based on the desired magnetic field. The magnetic field from the winding pattern is put back into the 1D calculation to re-optimize other parameters, such as the intensity and detuning of the counterpropagating "slower" laser. The final program does a full 3D Monte Carlo simulation of the slowing process.

The 1D calculation does not take gravity into account, or the effect of a transverse velocity on the slowing process, but it can be used to find the correct parameter space for effective slowing. The program solves Newton's second law along the z-axis, where the acceleration is given in Eq. 2.18 and the magnetic field is replaced by Eq. 2.21. The resulting differential equation is numerically solved with the initial conditions $z(0) = 0$ and $z'(0) = v_0$. The program allows for dynamic manipulation of the relevant parameters for slowing, namely B_b, B_t, s, δ, v_0, and z_0. A screen shot of the output is shown in Fig. 2.5. The position and velocity as a function of time will determine the possibility of capture by the optical molasses. The position as a function of time (top graph in Fig. 2.5) needs to be monotonically increasing, showing that the atoms do not turn around in the slower. Both graphs should also show deceleration followed by a constant final velocity out of the slower toward the molasses region. The desired final velocity needs to be $\lesssim 30$ m s^{-1}, allowing for capture from the power-broadening molasses beams. The stability of the slowing process can also be tested by making small changes in the control settings and observing the

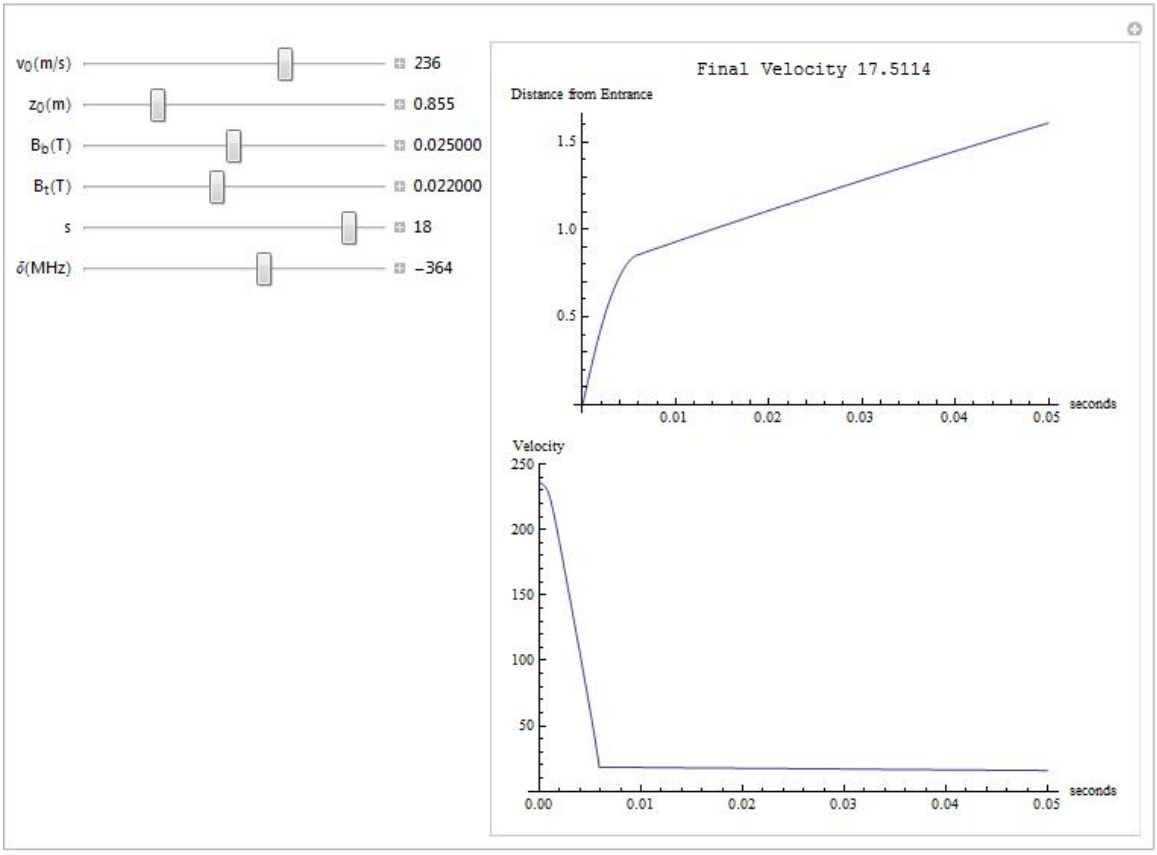

Figure 2.5: Screen shot of the 1D calculation output. The manipulation controls may be used to optimize the final velocity. The top graph shows $z(t)$ and the bottom graph shows $v_z(t)$.

change in final velocity.

In order to physically construct the winding pattern required for the tapered magnetic field, we first chose a slower magnet length. The results from the 1D calculation suggested the slowing process was rather immune to the slower length, provided it was long enough. Available space for the slower system limited the length of the slower to < 90 cm. An eventual slower length of 855 mm was settled on. In order to calculate the winding pattern, the sizes of the

wire and the radius of the slower tube must be defined. By noting that the magnetic field is proportional to the turns per unit length, the number of turns of wire needed to produce the desired field may be estimated. Once a design operating current is chosen, the winding pattern is determined. The magnetic field of each turn is determined by the Biot-Savart law and summed along the length of the slower. The ideal field and the wire-wrapped field are shown in Fig. 2.6. The wire-wrapped magnetic field is a very good approximation to the

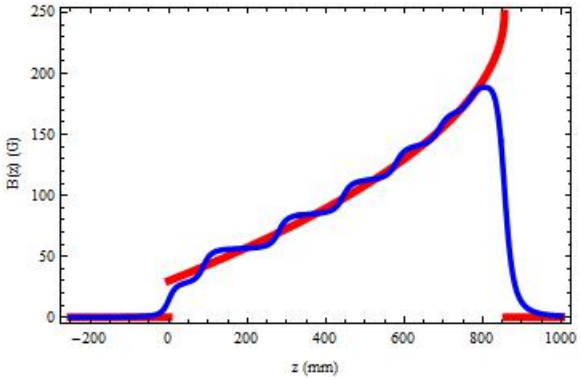

Figure 2.6: Magnetic field profiles for the Zeeman slower. The red curve is the ideal magnetic field. The blue curve is the magnetic field generated from the solenoid winding pattern.

ideal field. The maximum value of the wrapped field is ~ 60 Gauss below the ideal field, however, so the effect on the slowing process must be accounted for. This is done by importing the magnetic field profile back into the program that solves the 1D equation of motion. The result with the winding pattern included is shown in Fig. 2.7. The smaller maximum magnetic field requires a much different detuning to achieve effective slowing. The effect of the wire wrapping

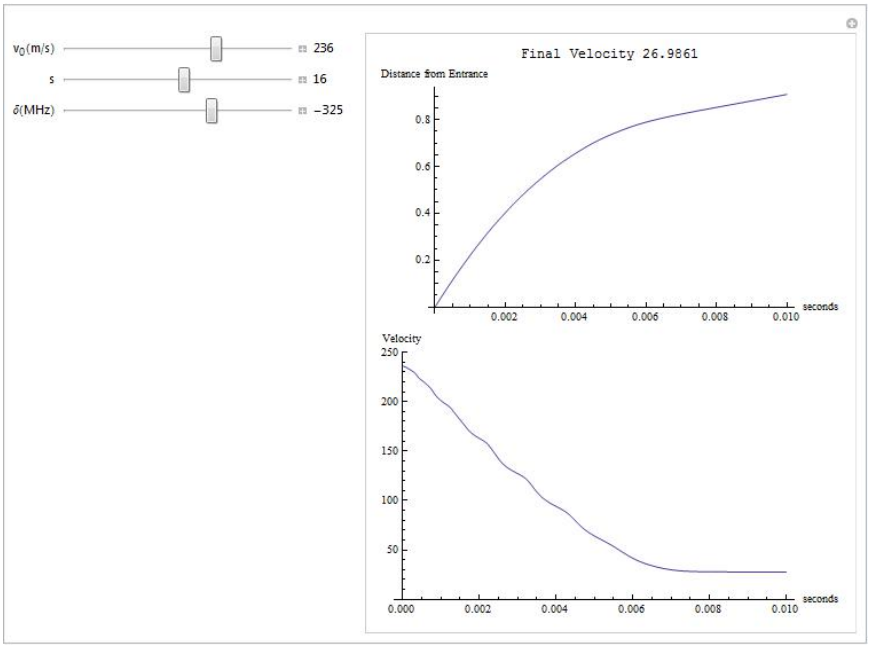

Figure 2.7: Screen shot of the 1D calculation output. The top graph again shows $z(t)$ and the bottom graph shows $v_z(t)$. The structure of the winding pattern is evident in the velocity.

can easily be seen in the velocity of the atom as it travels down the slower. The parameters from this program may be used as input for the full Monte Carlo simulation, which is reproduced in Appendix C.

The Monte Carlo simulation calculates the trajectories of atoms in 3D, including the effects of gravity and a transverse velocity. The initial conditions used for the differential equations are defined from the initial distributions of positions and velocities. The positions are random numbers chosen from a uniform disk with the size of the last aperture. The diameter of the apertures and the distance between them defines a maximum transverse velocity, v_{trans},

that the atoms can have and still exit the oven. The velocities in the x and y directions are random numbers that lie between $\pm v_{trans}$. The velocity in the z direction is a random number that comes from the Maxwell-Boltzmann distribution of speeds for a given temperature (see Eq. 2.7). An example of the initial distributions is shown in Fig. 2.8. The positions are determined from an aperture of 1 mm in diameter and the speeds down the slower are chosen from a Maxwell-Boltzmann distribution at 350 K. We then have all of

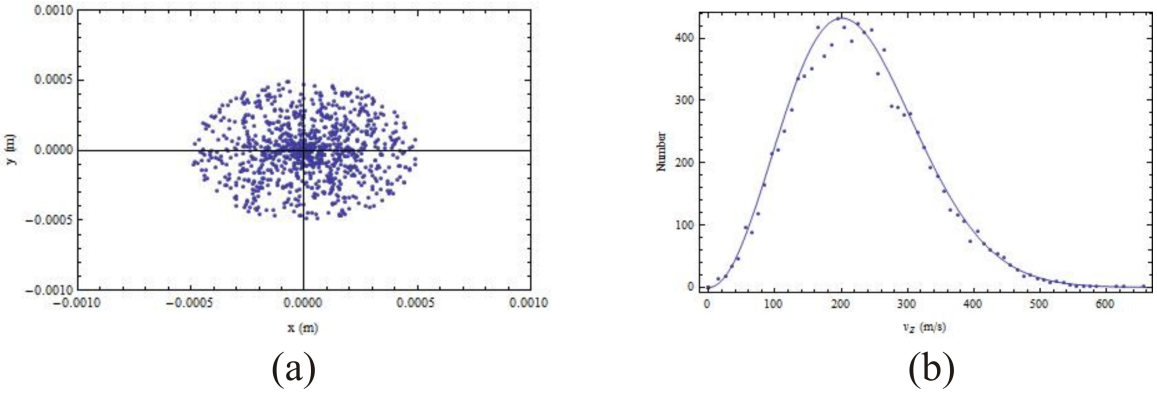

Figure 2.8: (a) The distribution of positions from which $x(0)$ and $y(0)$ are determined. (b) Dots represent random speeds down the slower for $T = 350$K. The curve is a plot of Eq. 2.7 for $T = 350$K.

the initial conditions necessary to solve the 3D equations of motion, $\mathbf{F} = m\mathbf{a}$, where $\mathbf{F} = \langle 0, -mg, F_z \rangle$. The force down the slower, F_z, may be chosen to come from the ideal field or any imported field. The trajectories are then calculated for a given saturation parameter, s, and laser detuning, δ. Any number of atom trajectories may be simulated, but $N_{enter} = 1000$ is enough to accurately estimate the slowing efficiency. The number of atoms captured by the molasses,

N_c, is determined by a capture radius and the final velocity. If the final velocity is below the capture velocity (~ 30 m s^{-1} for our power-broadening beams), and lands in a disk (with the capture radius) at the appropriate distance from the beginning of the slower, the atom is considered captured. The slowing efficiency is then the ratio N_c/N_{enter}.

The slowing process cannot slow all atoms. If the atoms are moving too fast, they will always see the light as too blue and not be slowed. On the other hand, if they are moving too slow, the transverse velocity of the atoms will carry them out of the capture radius. This effect can be seen in the Monte Carlo simulation. Fig. 2.9 shows the position of the atoms in the xy-plane at $z = z_0 + L = 1134.4$ mm, where L is the distance from the end of the slower to the center of the trapping region. The number of atoms falling in the capture radius (yellow dots in Fig. 2.9) is then N_c, and the slowing efficiency may be calculated.

The data in Fig. 2.9 correspond to a simulation with the ideal magnetic field, Eq. 2.21, where $B_b = 250$ Gauss and $B_t = 220$ Gauss. The laser parameters are $s = 16$ and $\delta = -2\pi \cdot 365$ MHz. These parameters were determined from Fig. 2.5. The slowing efficiency in this simulation is 55%. From run to run, the efficiency varies by about 3%.

To simulate real slowing, the wire-wrapped magnetic field profile in Fig. 2.6 is imported and the laser parameters are taken from Fig. 2.7. The results of the Monte Carlo simulation are shown in Fig. 2.10. For these parameters, the simulation predicts a slowing efficiency of 41%. The number is reduced from

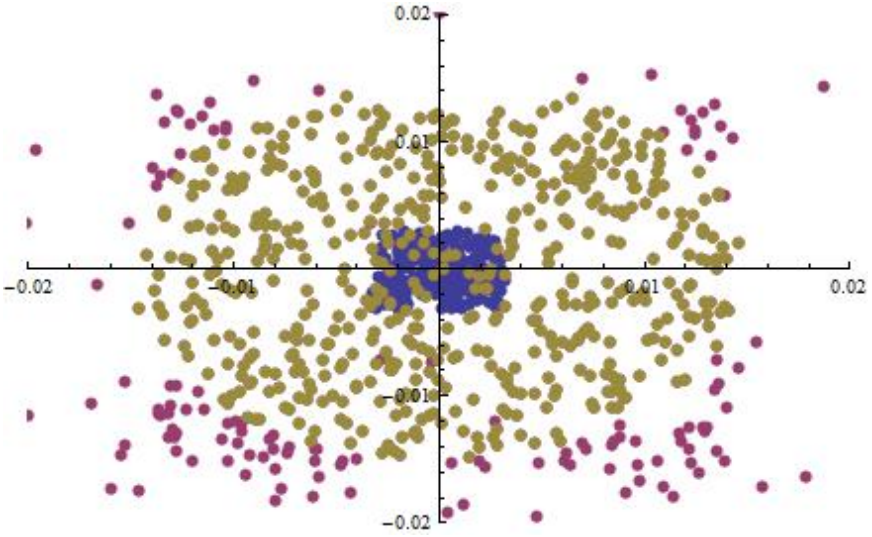

Figure 2.9: Screen shot of the Monte Carlo output for the ideal case. The dots represent the atoms arriving in the plane $z = 1134.4$ mm from the slower entrance. The blue dots are atoms that were moving too fast initially to be caught in the slowing process. The yellow dots are atoms that have been effectively slowed and captured. The magenta dots are atoms that have been slowed, but their transverse velocity has taken them out of the capture radius. Note each atom arrives in this plane at different times.

the ideal case because the slowing laser is closer to resonance, decreasing the maximum velocity of atom that can be slowed.

The final-velocity distribution may recovered by binning the number of atoms according to their velocity as they reach the trapping region. The velocity distribution for 5 m s^{-1} bins is shown in Fig. 2.11. The velocity distribution spikes at $v_z = 24.28$ m s^{-1}, indicating that a large fraction of atoms have been

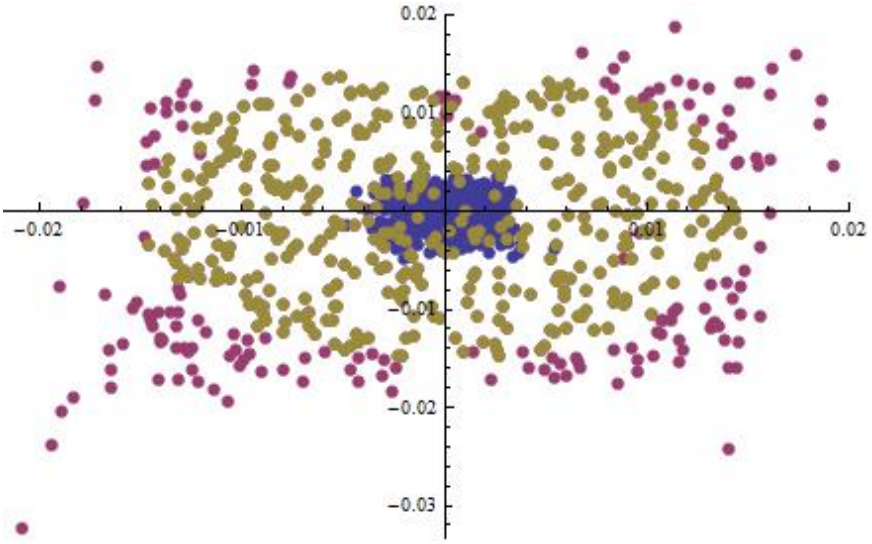

Figure 2.10: Screen shot of the Monte Carlo output for realistic input parameters.

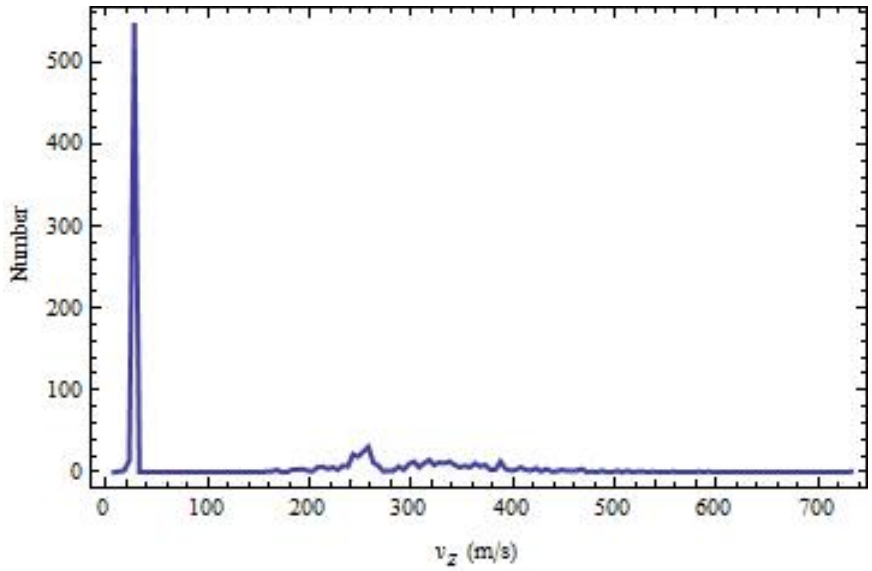

Figure 2.11: Velocity distribution of atoms at the center of the trapping region. A significant fraction of the atoms have been slowed.

slowed to the same final velocity.

The slowing efficiency may be used to estimate the flux of atoms that can be

loaded into the MOT. All we need is the flux of atoms coming out of the last aperture and then the loading rate of atoms into the MOT may be determined and compared with the loading rate into a MOT from the background vapor. Eq. 2.16 may be used to estimate the loading rate of atoms into the MOT. For background vapor loading, the capture velocity of the molasses beams is used to determine $v_{r,max}$ and $v_{z,max}$. Assuming the vapor cell is $T = 25°\text{C}$ and the atoms are effusing from a 1/2" hole, the MOT can load atoms at ~ 20 MHz. Note that this number may also be obtained by scaling the number of atoms exiting the oven per second (Eq. 2.13) by the probability the atoms will have a velocity below the capture velocity.

Using Fig. 2.11 one can see that atoms below $v_z = 180$ m s^{-1} have been effectively slowed, setting the value of $v_{z,max}$. The maximum radial velocity, $v_{r,max}$, is reduced from the value determined by the apertures because as the atoms slow down, they spend more time drifting off of the axis of the beam. Taking these times into account, a conservative estimate for $v_{r,max}$ is 0.3 m s^{-1}. For an oven temperature of $T = 50°\text{C}$ and aperture diameters of 1 mm, the number of atoms exiting the first aperture is given by Eq. 2.13 as 2 x 10^{13} s^{-1}. The loading rate calculated by Eq. 2.16 is then 25 MHz. To compare this value with the simulation, the number of atoms making it through both apertures must be estimated. This is done simply by scaling the number of atoms exiting the first aperture by the relative solid angle available from the second aperture. This represents a factor ~ 1 x 10^{-6}, so atoms are entering the slower at a rate of

$\sim$ 20 MHz. They are roughly slowed with an efficiency of 50%, so the simulation predicts a loading rate of $\sim$ 10 MHz of atoms, which is in good agreement with the rate determined from Eq. 2.16.

As previously described, even if the loading rate into the MOT from the atomic beam is close to that from the background vapor, larger steady-state number MOTs may still be achieved. This is because loading the MOT from an atomic beam can lead to much lower pressures in the MOT region, reducing trap loss due to collisions with background atoms. Loading MOTs with very large steady-state atom numbers opens up the possibility to load atom traps with lower trapping potentials from the MOT. Further, traps which do not rely on the scattering of photons can lead to much higher densities. One such trap which has a low trapping potential and high maximum density is an optical dipole trap, which is described in the next section.

2.3 Far Off-Resonance Traps

2.3.1 Introduction

The force of atoms interacting with an off-resonant laser field is called the optical dipole force. The radiation pressure force relies on the scattering of photons whereas the dipole force originates from the interaction of the induced atomic electric dipole moment with a detuned laser field where the absorption probability is small or negligible. Both forces are present for an atom in a laser

field, but near resonance, the radiation pressure force dominates. When the detuning from resonance is large and the dipole force dominates, optical dipole traps can be realized in which the photon scattering rate from the atoms is very small. Because scattering of photons in these traps can be eliminated, light-induced mechanisms that limit the density are eliminated as well. These traps then open an entire experimental regime not accessible with the MOT (see the comprehensive review of [39]).

The salient features of optical dipole traps may be obtained by considering an atom subject to a classical laser field. The laser field drives the oscillation of the dipole moment in a manner similar to a forced harmonic oscillator. If the driving field is at a frequency higher than an atomic resonance, the atom oscillates out of phase with the field and the atom is repelled from the field. Conversely, if the driving field is below the resonance (*red detuned*), the induced dipole moment will oscillate in phase with the field and the atom will have its energy reduced. The latter case of red detuning is the only type of optical dipole trap considered here and will be assumed throughout the rest of this Section.

For a driving frequency of ω, the laser field is written in complex notation as

$$\mathbf{E}(\mathbf{r},t) = \hat{\epsilon}\tilde{E}(\mathbf{r})e^{-i\omega t} + c.c. \tag{2.22}$$

The atomic dipole moment is similarly given in complex notation as

$$\mathbf{p}(\mathbf{r},t) = \hat{\epsilon}\tilde{p}(\mathbf{r})e^{-i\omega t} + c.c. \tag{2.23}$$

The complex amplitudes $\tilde{E}$ and $\tilde{p}$ are simply related by the complex polarizability,

$\alpha(\omega)$.

$$\tilde{p} = \alpha(\omega)\tilde{E} \tag{2.24}$$

The real part of the polarizability (dispersion) gives rise to the interaction energy and the imaginary part of the polarizability (absorption) is responsible for dissipation of energy through the scattering of photons.

The atomic polarizability may be obtained by modeling the atom as a Lorentz classical harmonic oscillator. In this model, the electron (mass m_e, charge $-e$), is harmonically bound to the infinitely massive nucleus with oscillation frequency equal to the atomic resonance frequency. As a semi-classical extension, we may consider the quantum mechanical decay rate for a two-level atom, Γ (Eq. A.20). The equation of motion then becomes

$$\ddot{x} + \Gamma\dot{x} + \omega_0^2 x = -\frac{e}{m_e}E(t). \tag{2.25}$$

The complex polarizability may then be obtained and is given by

$$\alpha(\omega) = \frac{e^2}{m_e}\frac{\Gamma/\omega_0^2}{\omega_0^2 - \omega^2 - i\,(\omega^3/\omega_0^2)\,\Gamma}. \tag{2.26}$$

The dipole potential, $U_d = -1/2\langle \mathbf{pE} \rangle$, may be written as

$$U_d(\mathbf{r}) = -\frac{3\pi c^2}{2\omega_0^3}\left(\frac{\Gamma}{\omega_0 - \omega} + \frac{\Gamma}{\omega_0 + \omega}\right) I(\mathbf{r}), \tag{2.27}$$

where $I(\mathbf{r}) = 2\epsilon_0 c|\tilde{E}|^2$ is the intensity of the laser field. The dipole force is obtained by taking the gradient of the potential energy $F_d(\mathbf{r}) = -\nabla U_d(\mathbf{r})$. The gradient acts on the laser intensity $I(\mathbf{r})$ so a focusing laser beam can create a

restoring force at the focus if the laser tuned to the red of any atomic transition. The potential energy for this case is shown in Fig. 2.12.

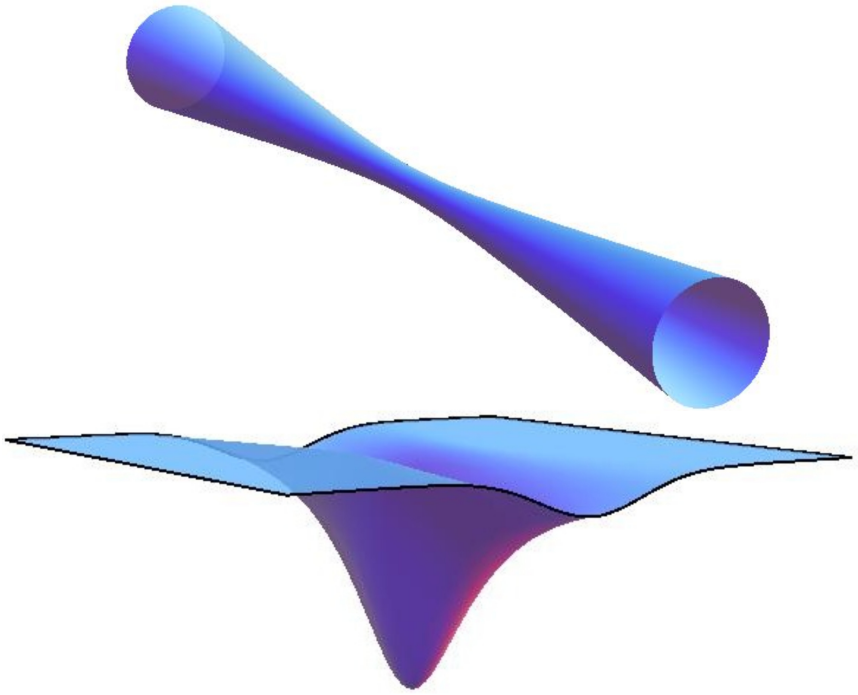

Figure 2.12: A focusing laser beam (top) creates a potential well with which to trap atoms (bottom).

The absorbed power (due to the imaginary part of the polarizability), $P = \langle \dot{\mathbf{p}}\mathbf{E} \rangle$, produces a scattering rate of photons, $\Gamma_{sc}\hbar\omega = P$. Using the previous relation for the intensity of the laser field, the rate of scattering photons from an optical dipole trap is given by [39]

$$\Gamma_{sc}(\mathbf{r}) = \frac{3\pi c^2}{2\hbar\omega_0^3}\left(\frac{\omega}{\omega_0}\right)^3\left(\frac{\Gamma}{\omega_0-\omega}+\frac{\Gamma}{\omega_0+\omega}\right)^2 I(\mathbf{r}). \tag{2.28}$$

Optical dipole traps function in three different detuning regimes. The first type operates close to resonance but with $\delta \gg \Gamma$ so that the rotating wave

approximation is valid (see Appendix A). The proximity to resonance means terms oscillating with $1/(\omega_0 + \omega)$ can be neglected. This near-resonance type of dipole trap was actually the first type of neutral atom trap realized by experiment [40]. A second type of dipole trap is operated when the detuning is so large

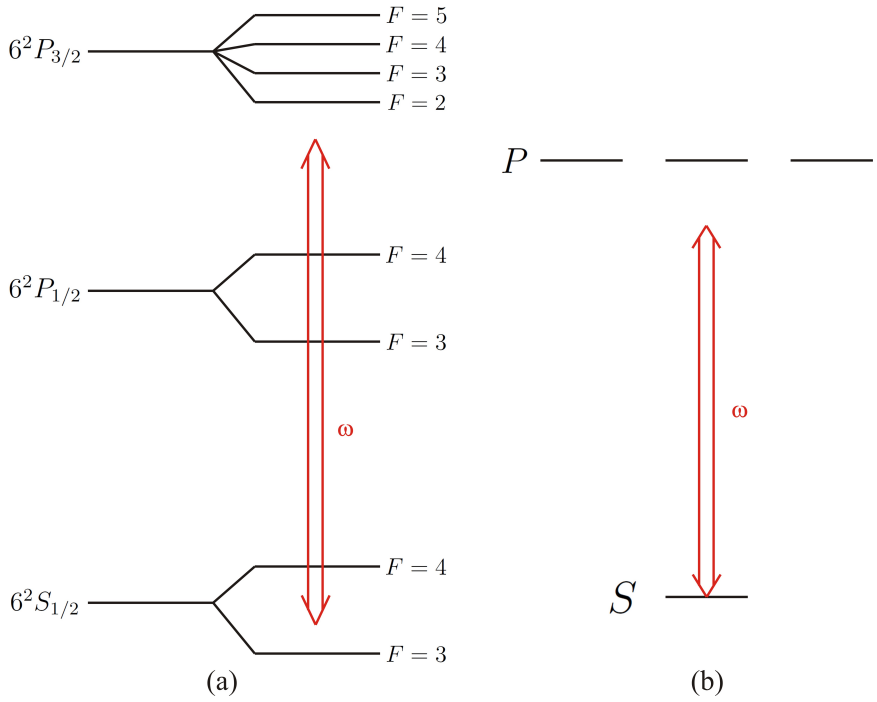

Figure 2.13: Different regimes of the optical dipole force traps. (a) Relevant states and splittings of the D lines of cesium. (b) Simplified levels seen by the optical dipole trapping laser used in this thesis.

that the rotating wave approximation ceases to be valid. This generally occurs when the detuning is larger than the fine structure splitting of the atom (see Fig. 2.13). This far-off resonance trap (FORT) is the main subject of this thesis and will be compared with the third type of dipole trap to further illuminate the properties of optical dipole traps. The third type of optical dipole trap operates

in an extreme detuning regime such that $\omega \ll \omega_0$ and the radiation field appears nearly constant. This quasi-electrostatic trap (QUEST) is compared to a FORT in the next Section.

2.3.2 QUEST vs. FORT

The FORT described in this thesis uses 1064 nm light. This light is sufficiently detuned that the fine structure is not resolved (see Fig. 2.13). We can again approximate this as a two-level atom that has the weighted average of both D lines by defining an effective transition frequency, ω_{eff}, where

$$\omega_{eff} = \frac{1}{3}\omega_{D1} + \frac{2}{3}\omega_{D2}, \tag{2.29}$$

and a corresponding effective linewidth

$$\Gamma_{eff} = \frac{1}{3}\Gamma_{D1} + \frac{2}{3}\Gamma_{D2}. \tag{2.30}$$

The appropriate dipole potential and scattering rate may be obtained by using these new effective parameters in Eq. 2.27 and Eq. 2.28.

$$\begin{aligned} U_{FORT}(\mathbf{r}) &= -\frac{3\pi c^2}{2\omega_{eff}^3}\left(\frac{\Gamma_{eff}}{\omega_{eff}-\omega} + \frac{\Gamma_{eff}}{\omega_{eff}+\omega}\right) I(\mathbf{r}) \\ \Gamma_{FORT}(\mathbf{r}) &= \frac{3\pi c^2}{2\hbar\omega_{eff}^3}\left(\frac{\omega}{\omega_{eff}}\right)^3 \left(\frac{\Gamma_{eff}}{\omega_{eff}-\omega} + \frac{\Gamma_{eff}}{\omega_{eff}+\omega}\right)^2 I(\mathbf{r}) \end{aligned} \tag{2.31}$$

The same equations hold for the QUEST, but because we now have $\omega \ll \omega_0$, the trapping potential may be obtained through Eq. 2.24, using the static value of the polarizability, $\alpha_{static} \equiv \alpha(0)$.

$$U_{QUEST}(\mathbf{r}) = -\frac{\alpha_{static}}{2\epsilon_0 c} I(\mathbf{r}) \tag{2.32}$$

The scattering rate of photons in the QUEST simplifies to

$$\Gamma_{QUEST}(\mathbf{r}) = \frac{6\pi c^2}{\hbar\omega_{eff}^5}\left(\frac{\omega}{\omega_{eff}}\right)^3 \Gamma_{eff}^2 I(\mathbf{r}) \tag{2.33}$$

.

The main difference in the two types of traps is in their scattering rates. For trap depths that are on the order of 1 mK, the scattering rate of photons in the FORT is counted in minutes whereas scattering in the QUEST is counted in days. In both cases, scattering is eliminated enough to provide a large increase in density. Because few-body events occur at rates proportional to powers of the density, the increased density afforded by far-off resonance traps allows for more sensitive detection of these events as well as the ability to probe to smaller interaction distances.

Chapter 3

Experimental Apparatus

Experimental physicists must become very familiar with the various pieces of apparatus required to perform an experiment. The experimental needs can be vast, spanning many different areas of knowledge. This chapter focuses on those aspects of the apparatus which are most important in generation of ultracold samples of atoms.

3.1 Ultrahigh Vacuum System and Cs Ovens

The lifetime of a trap is characterized by the time it takes for a trapped atom to be lost. Collisions with background atoms in the chamber are the major source of trapped atom loss when the density is not too high. If the background pressure becomes too large, collisions become so frequent that a trap cannot be maintained. For this reason traps for neutral atoms must be located in regions of ultrahigh vacuum (UHV). In our experiment the atoms are provided by an oven which heats cesium to a background vapor pressure. The UHV and oven environments for the main experimental chamber and Zeeman slower are different and will be explained separately.

3.1.1 Main Chamber System

Trapped atoms are captured at the center of a stainless steel spherical chamber. The main chamber is evacuated with a series of pumps separated by a system of valves. The valves are controlled by a programmable logic controller that prevents chamber contamination in the event of a power failure. There are two pumps with high pumping speeds attached to the main chamber. A non-evaporable getter (NEG) pump (SAES CapaciTorr 400-2) is attached so that the complete surface area of the getter material is exposed to the interior of the spherical chamber, see Fig. 3.1 A turbo-molecular pump (Leybold TMP340MC)

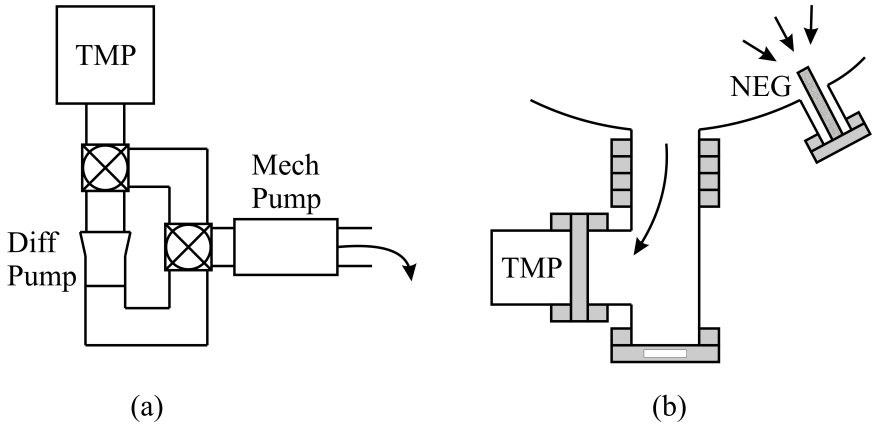

Figure 3.1: (a) Backing system for main chamber turbo-molecular pump (TMP). The TMP can be backed by the mechanical pump or diffusion pump, or both valves can be closed for chamber isolation. (b) Main chamber pumps: Non-Evaporable Getter (NEG) pump and TMP.

is connected to the chamber through an 8" tee. The turbo pump is backed by a

diffusion pump (Varian M2), which is backed by a rotary-vane mechanical pump (Leybold D65B).

Cesium atoms may be introduced into the main chamber through an oven. The oven consists of an ampule of cesium contained in a flexible bellows which is connected to the chamber by a right-angle mechanical valve. When the ampule is replaced, the valve is opened and the oven is baked out with the cesium ampule in tact. When UHV pressures are reattained, the cesium can be exposed to the vacuum by breaking the ampule (a small glass container) and opening the valve. Gently heating the oven ($T \sim 30°C$) produces enough background vapor to form a MOT. If background pressure is not an issue for the experiment, the oven may be exposed to higher temperatures for MOTs with very high atom numbers.

3.1.2 Zeeman Slower System

The frame of the Zeeman slower is a 2.75" stainless steel nipple that is 3 feet long. The slower frame is attached to the main chamber at one end and a mechanical gate valve (VAT 0132-UE08) at the other (see Fig. 3.2). The VAT valve can withstand differential pressures of 2 atm and allows for complete isolation of the slower from the main chamber. A six-way mini (1.33") cross is attached to the VAT valve. Attached to the cross is a 20 L s^{-1} ion pump (Varian VacIon). The cross is fitted with a glass viewport to allow for atomic beam diagnostics. A larger cross (2.75") is attached to the mini cross. This cross contains two more pumps, an ion pump (Gamma Vacuum 40S) and a turbo-molecular pump

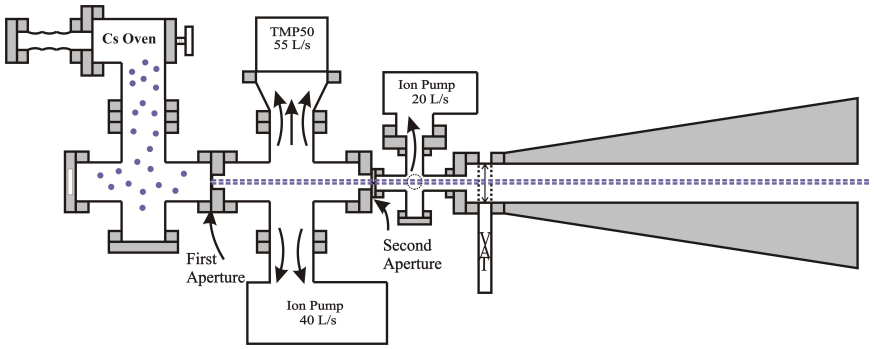

Figure 3.2: Diagram of the Zeeman slower. The pumps and magnetic field taper are shown.

(Leybold TMP50), and also holds the apertures (1 mm diameter) that define the initial size of the atomic beam. The pumping speeds are shown in Fig. 3.2. The oven that supplies the atomic beam is a similar construction to the main chamber oven. The oven is attached to a cross that has a glass viewport to look down the axis of the atomic beam. This viewport is crucial for the initial alignment of the atomic beam to the trapping region located in the center of the time-of-flight spectrometer.

3.2 Time-Of-Flight Spectrometer

The entire chamber system is centered on a time-of-flight spectrometer. The primary function of the spectrometer is to detect positive ions. When a positive ion is created (primarily through field-ionization or photoionization), it can be projected towards a micro-channel plate (MCP) detector. The arrival time-of-flight distributions and positions the ions strike the detector provide information

about the dynamics in the trap. This information can be used in conjunction with high-resolution spectroscopy to learn a great deal about atomic and molecular systems.

3.2.1 Spectrometer and Trap Geometry

The spectrometer hangs from all-thread and extends the length of the spherical chamber. The spectrometer is fixed around the chamber center with aluminum shims. The spectrometer consists of mounts for the magnetic field coils used for the MOT, electric field shaping plates, and a grounded flight tube all situated above a z-stacked MCP detector. The spectrometer is rendered to scale inside the chamber in Fig. 3.3. The magnetic field coils are wound from hollow copper wire that allow water flow for cooling. Three shaping plates surround the trapping region to provide a uniform electric field when a voltage is applied to the top plate. The voltage is delivered to the plates by a high-voltage pulser (DEI PVX-4140) powered from a high voltage power supply (Glassman EK3R200). Resistors are placed between the plates such that the resistance between the top plate and ground (bottom plate) is 3.1 kΩ. Positive ions are accelerated by the applied voltage down a grounded flight tube where they strike a position sensitive z-stacked MCP detector. The detector (Sensor Sciences 40 mm triple z-stack) can spatially resolve ions hitting 8 μm apart and produces fast timing signals $<$ 4 ns wide. The detector allows for very fast acquisition rates and can be used in conjunction with a fast analyzer to reproduce information in

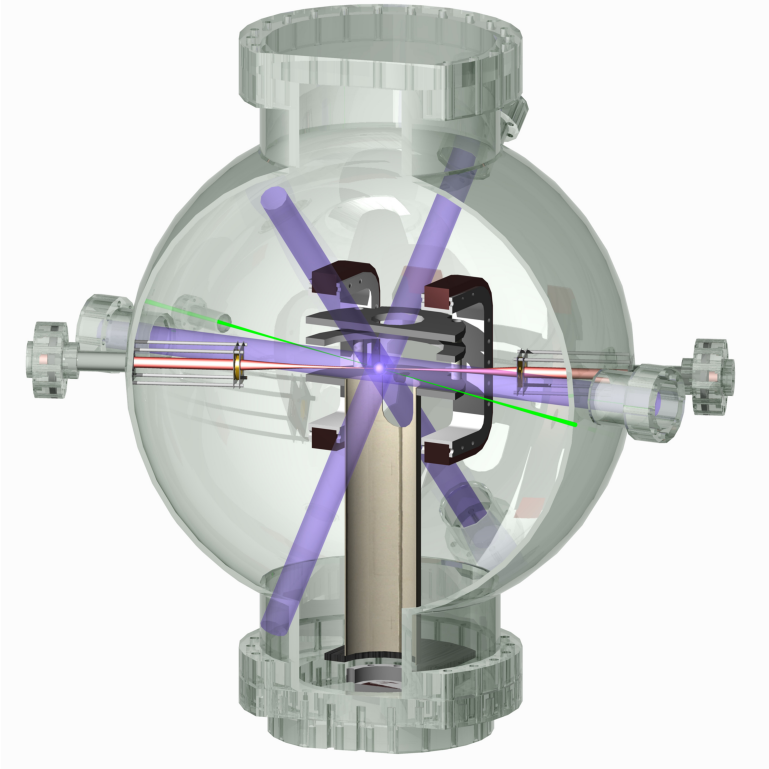

Figure 3.3: Rendering of the main chamber. The spectrometer is shown as a cross-section. The bright sphere at the center represents the MOT.

3D. Signals from the detector are processed with a fast multi-channel analyzer (MCA) card (FastComTec P7886) with 500 ps time resolution.

3.2.2 Quadrupole Field Switching

The presence of magnetic fields are not desirable in many experiments. Because the magnetic fields in these experiments are generated by electromagnets, the time required to switch the field off can be very large due to the large inductance. The quadrupole field required for the MOT can interfere with the loading of

the dipole trap, so we need to turn it off during the dipole trap loading period. This loading period lasts ~ 50 ms, so we want the field to shut off much faster than that time. This required the construction of a fast magnetic field switching circuit.

A relatively simple circuit was constructed based on an insulated-gate bipolar transistor (IGBT). The idea of the circuit is to quickly dissipate the large voltage (back emf) generated by suddenly switching off the magnetic field. Dissipating large voltage spikes is a common practice and can be easily accomplished with transient-voltage suppressors (TVSs). These TVSs are just Zener diodes with high reverse breakdown voltages. This allowed the construction of the simple circuit shown in Fig. 3.4. The IGBT (Semikron SKM200GB) is a voltage (V_{gate}) controlled device that can change its state of conductivity. Once the IGBT stops conducting electricity, a back emf is generated on the coil. Protection diodes (Vishay 40EPS12) are placed in front of the power supply that have a breakdown voltage equivalent to the IGBT. If TVS diodes (Littelfuse 15KP60A) are placed in series as in Fig. 3.4, their reverse breakdown voltages add. When the back emf appears on the coil, the TVS diodes begin conducting and act as a drain for the current in the MOT coil. Several TVS diodes may be added in series to provide a very large breakdown voltage. The back emf is clamped at the summed reverse breakdown voltage, so the time required to drain the current is simply calculated by $V_{emf} = -L\frac{dI}{dt}$. Switching times of 10 μs are easily achievable.

The magnetic field switching circuit was simulated in a free circuit analysis

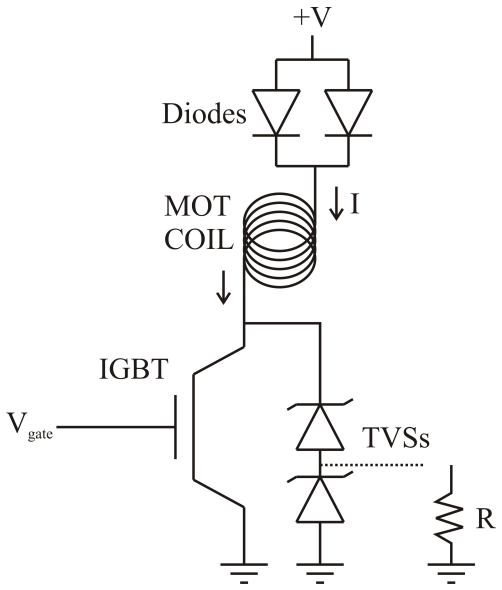

Figure 3.4: Magnetic Field switching circuit. The transient voltage suppressors (TVSs) provide a fast drain for current in the MOT coil when the insulated-gate bipolar transistor (IGBT) gate closes. The switching time is controlled by the series breakdown voltage of the TVSs.

program *5Spice*. In order to test if the circuit was draining the current as planned, a resistive network ($R = 0.02\Omega$, 25W) was inserted into the circuit as shown in Fig. 3.4. This allowed a fraction of the current to move through the resistive network developing a voltage. The time required for the voltage (proportional to the current) to go to zero can easily be measured in this way on an oscilloscope. The oscilloscope reading and associated simulation are shown in Fig. 3.5. The TVS diodes used in Fig. 3.5 sum to 560 V of breakdown voltage. The simulation predicts a smooth decrease of the current to zero in ~ 20 μs,

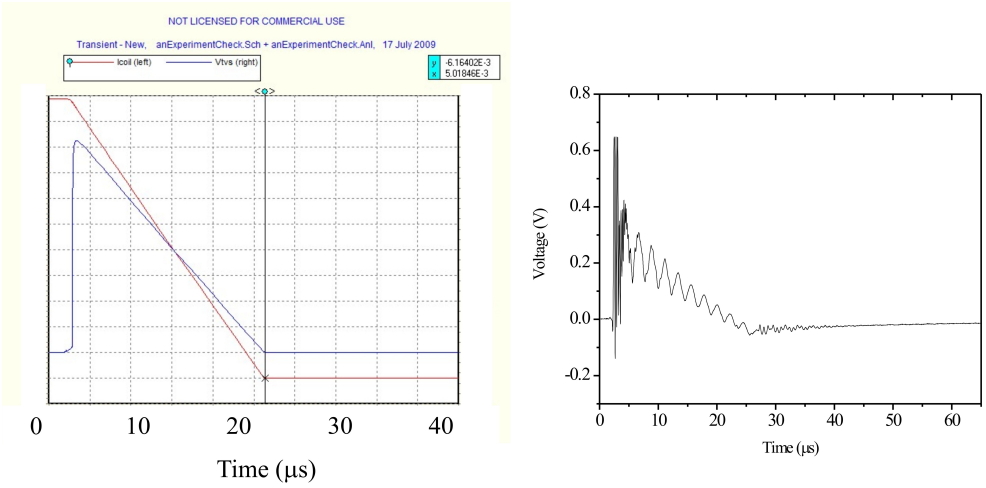

Figure 3.5: (a) Theoretically predicted time response of the switching circuit. Red trace is the current through resistive network and the blue trace is the potential drop across the network. (b) Experimental trace of the voltage drop across the resistive network.

and the experimental value is very close (~ 25 μs). The total breakdown voltage of the TVS diodes can be adjusted so that the magnetic field current may be drained away on any timescale larger than ~ 10 μs.

3.3 Diode Lasers and Tapered-Amplifier

3.3.1 Diode Lasers

Two diode lasers and a tapered-amplifier (TA) are responsible for cooling and trapping cesium and a third diode laser is used as a general purpose laser that can be used for experiments or diagnostics. Because real atoms have more

than two levels, the situation is more complicated than described in Section 2.1. Creating an effective two-level atom that can repeatedly scatter photons requires two different laser frequencies for the alkali metals. Because the laser responsible for cooling the atoms (the "*trapping*" laser) must be detuned, off-resonant excitation optically pumps the atoms into a state that is no longer resonant with the laser, see Fig. 3.6. The atoms may be pumped back into the

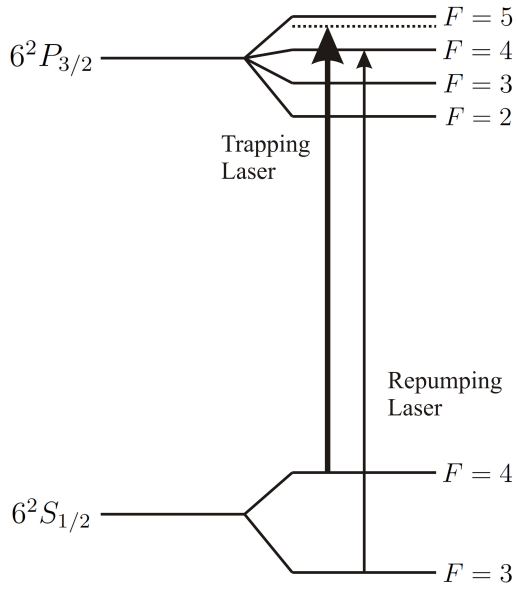

Figure 3.6: Energy levels of the D2 transition in cesium. The indicated laser frequencies are required for our MOT.

cycling transition by the use of a separate resonant laser. This "*repumping*" laser and the general purpose laser are both external cavity diode lasers (ECDLs) in Littrow configuration. The laser diodes (JDS Uniphase SDL-5401-G1) can provide a maximum of 150 mW of power. The laser diodes are housed in an aluminum mount which was machined in the department. The housing is shown

in Fig. 3.7 and is identical for both lasers. The housing is designed to allow

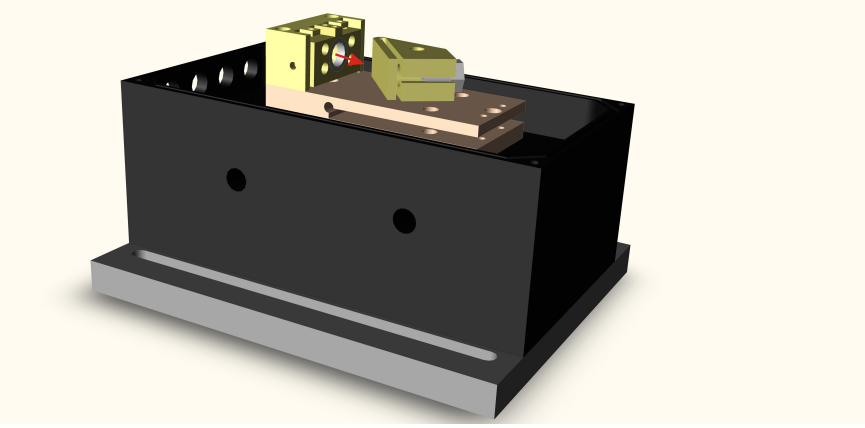

Figure 3.7: Rendering of the external-cavity diode laser (ECDL). Light emitted from the laser diode through collimating aspheres is indicated by the red arrow. Not shown is the holographic grating or the lid.

electrical and thermal control of the laser diode. The external cavity is formed by placing a holographic diffraction grating (Thorlabs GH-180) on the piece opposite to laser emission. Piezoelectric control of the position of the grating allows tunability of the laser. The laser diode and grating all sit on an aluminum piece that is electrically isolated from the base (and table) by thermoelectric coolers (Thorlabs TEC3-2.5). The entire housing may also be evacuated if laser diode temperatures cold enough to condense water are required (sealing lid not shown in Fig. 3.7).

Both lasers are frequency stabilized with a dichroic atomic vapor laser lock (DAVLL) [41]. Briefly, a dispersive signal can be obtained by measuring the

difference in the amount of light with orthogonal circular polarizations that is absorbed passing through cesium vapor in a constant magnetic field. The dispersive signal provides a slope which is approximately linear across the Doppler broadened absorption profile. A proportional and integral gain circuit is used to provide feedback on the laser. High frequency output from the circuit is fed back into the laser diode current and low frequency output is used to control the cavity length with a piezoelectric transducer pressing on the grating. These signals may be used to lock the laser to any desired point on the dispersive signal.

The main trapping laser is a 150 mW commercial distributed-feedback (DFB) laser diode from Toptica (DL100DFB). The DFB laser is a special type of diode laser which has a grating structure etched into the diode facet. This monolithic design is very stable against mechanical vibrations and is continuously tunable (mode-hop free) over several gigahertz using only the current to the laser diode. The frequency is stabilized with commercial circuitry (Toptica Digilock) using a signal generated from a saturated absorption setup. To achieve MOTs with large atom numbers, a large intersection volume of the laser beams is desired. Increasing the size of the beam decreases the intensity of the beam, so large diameter beams require larger powers to scatter the same number of photons per unit area. Larger powers are accomplished with the use of a tapered amplifier (TA).

3.3.2 Tapered Amplifier

The TA is placed in a master-oscillator-power-amplifier (MOPA) configuration where the DFB laser is the master oscillator (also called the *seed* laser). The TA is a semiconductor chip which has a large tapered gain section. If properly aligned, the output power can be greatly amplified while maintaining the spectral characteristics of the seed laser. Our TA is a 500 mW chip (Eagleyard Photonics EYP-0850-00500-3006-CMT03) which accepts a maximum of 50 mW of seed power input and a maximum of 1.5 amps of drive current. The housing for the TA system was also machined by our department and is shown in Fig. 3.8. The

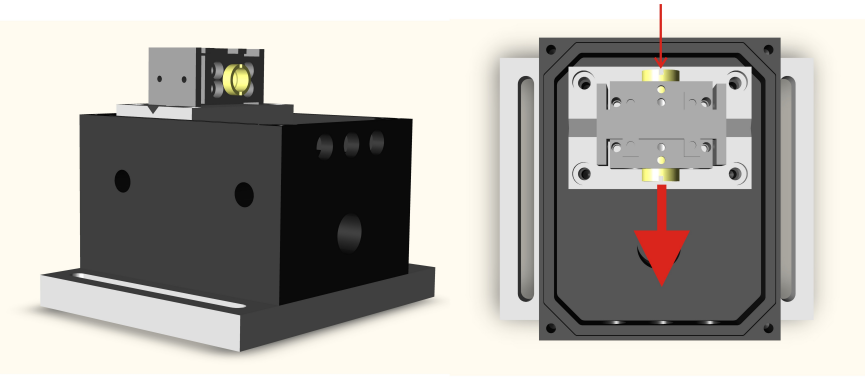

(a) (b)

Figure 3.8: Rendering of the tapered amplifier (TA). Seed light is focused onto the TA chip and amplified light is collimated by a set of aspheres.

TA has a very small input aperture of 3 μm diameter. The input tapers over a 2.75 mm distance to a 190 μm by 3 μm output. The input and output therefore require lenses of high numerical aperture (NA) to focus the incoming light and

to capture as much exiting light as possible. This is done with input ashpere (Thorlabs C330TME-B NA=0.68) and output asphere (Thorlabs C230TME-B NA=0.55). The housing in Fig. 3.8 allows for sensitive adjustment of the aspheric lenses with respect to the stationary TA chip.

Precise alignment of the seed laser to the input of the TA is required for sufficient amplification. As an initial alignment procedure, the TA was not powered by a current, but instead used as a photodetector so the output current from the TA chip could be monitored. This initial alignment is usually good enough to see immediate amplification of seed light. The small input of the TA requires the input seed light to be in TEM_{00} mode (Gaussian), ensuring a tight focus. The TA only accepts a linear polarization as well, so polarization-preserving single-mode fibers were used to deliver the seed light to the TA (see Fig. 3.9). With 25 mW of seed light, a full 500 mW of output power was obtained at 1.4 A of drive current. Experiments are usually operated with 15 mW of seed power and 1.25 A of drive current, which decrease the output power but increase the lifetime of the TA chip. The low demand on seed power also increases the lifetime of the DFB laser. In day-to-day operation, the total power available for the MOT trapping light is ~ 100 mW.

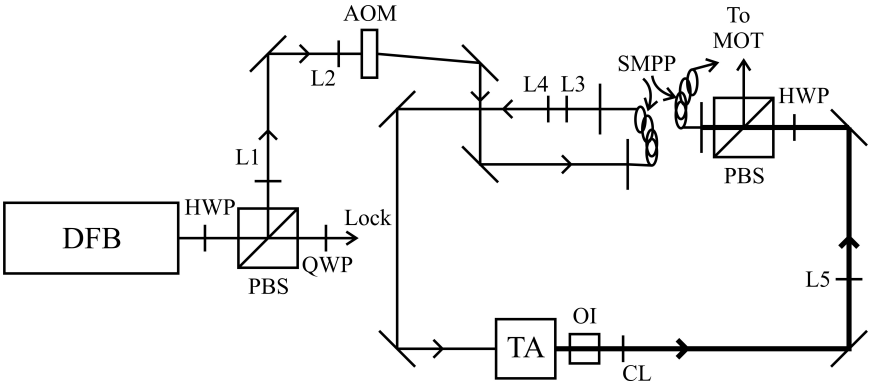

Figure 3.9: Setup for amplification of light. Seed light from the distributed feedback laser (DFB) is delivered to the TA and finally to a single-mode polarization-preserving fiber through the shown system of optics. HWP - Half-wave plate. QWP - Quarter-wave plate. PBS - Polarizing beam-splitter cube. L - Lens. OI - Optical isolator. CL - Cylindrical lens. AOM - Acousto-optic Modulator. SMPP - Single-mode polarization preserving fiber. A small amount of light from the DFB is used to stabilize its frequency.

3.4 Zeeman Slower

3.4.1 Magnet Assembly

The Zeeman slower design parameters were determined by simulating the atomic trajectories in the atomic beam. The designed ideal magnetic field was given in Eq. 2.21 with $B_b = 250$ Gauss and $B_t = 220$ Gauss. The main task of installing the Zeeman slower is the construction of the more realistic wrapping pattern shown in Fig. 2.6. The wire used for the slower magnet (AlphaCore

GP200 AWG 12) has a rectangular cross-section, which allows for smaller gaps between adjacent turns. The winding pattern that was numerically generated was modeled with computer aided design (CAD) and shown in Fig. 3.10. The slower magnet was wound on a lathe. The winding pattern and relevant distances to achieve the correct pattern are shown in Fig. 3.10. After the slower magnet had the desired winding pattern, the magnetic field along the slower had to be tested for accuracy. To measure the magnetic field, a Gauss meter was held in the center of a cylindrical die that was machined to exactly fit in the slower tube. Results are shown in Fig. 3.11. A string was tied to the die which could move the Gauss meter precisely down the slower tube. The experimental winding pattern reproduced the calculated magnetic field almost exactly. Once the field profile was verified, the coil was potted with epoxy and wrapped with kapton tape. The vacuum system (Fig. 3.2) was then attached and the oven was equipped with a cesium ampule. After baking, the Zeeman slower was ready to be tested.

3.4.2 Slower Performance

One important feature the Monte Carlo simulation does not account for is the presence of multiple atomic energy levels. Much like in the MOT, the presence of the extra levels leads to optical pumping into levels that no longer cycle photons. Atoms pumped into these levels must be re-pumped back into the resonant transition. This is accomplished by a second laser frequency that is near the repumping transition for the MOT. A good guess at the appropriate repumping

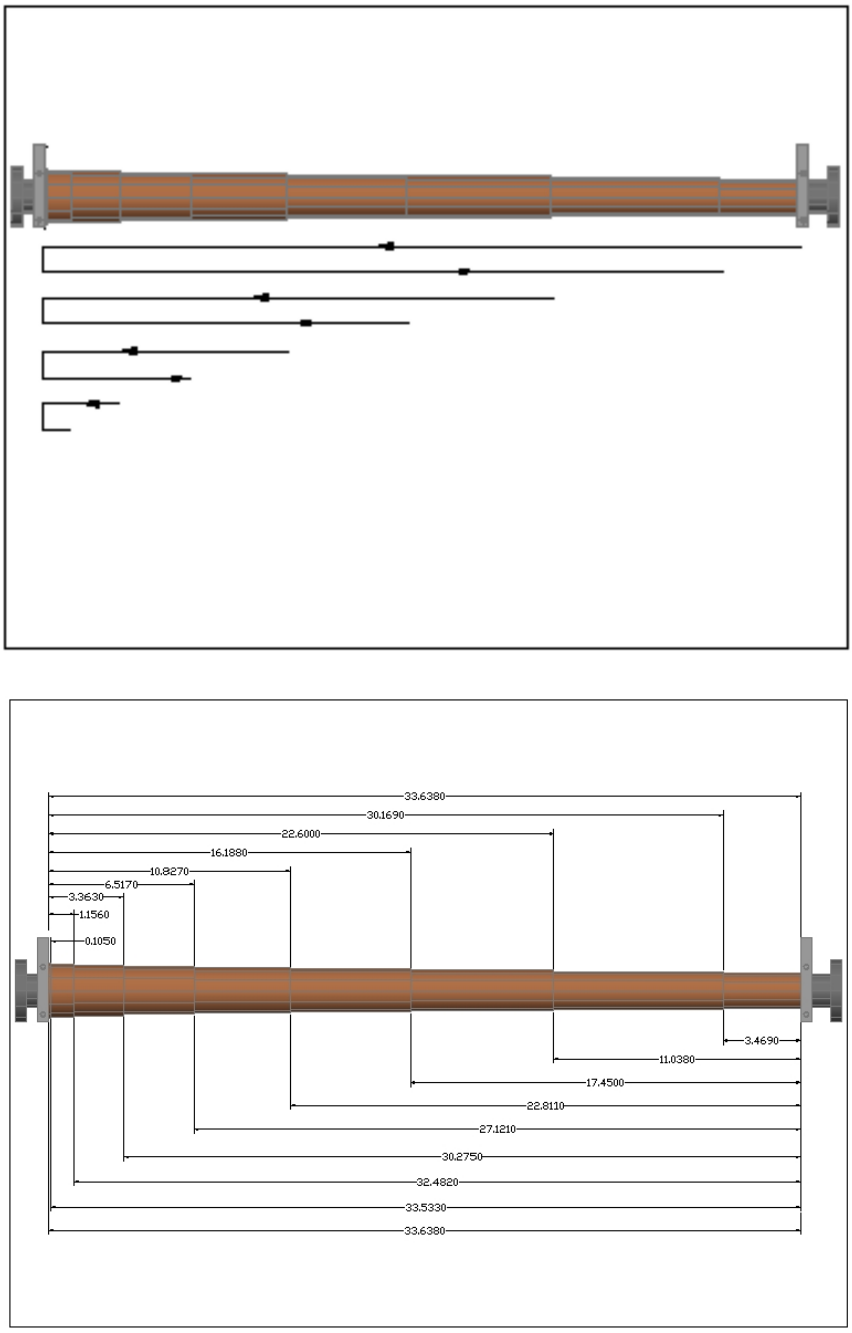

Figure 3.10: Winding of the electromagnet used for Zeeman slowing. (a) Pattern used to wind the electromagnet. Distances depicting the beginnings and the ends of the individual sections.

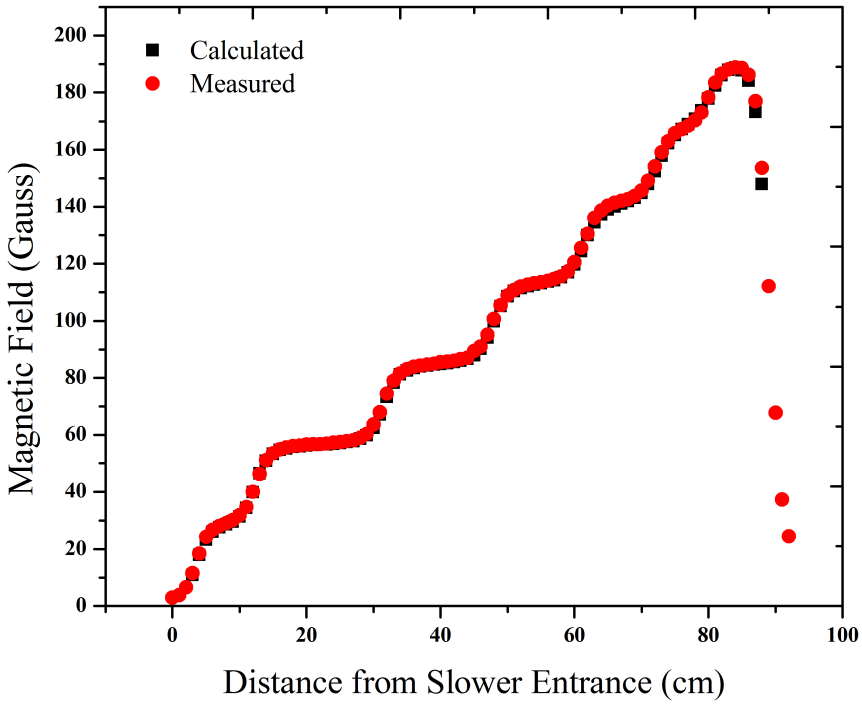

Figure 3.11: Magnetic field profile down the axis of the electromagnet for 6 Amps of current. The black squares represent the calculated profile used in the simulations. The red circles are the experimentally measured magnetic field.

frequency is to match the Doppler shift of atoms with the average speed, v_z, determined by the oven temperature. For $T = 323$ K, $v_z = 226$ m s^{-1}, and the appropriate frequency is 265 MHz red of the $6S_{1/2}(F = 3) \rightarrow 6P_{3/2}(F = 4)$ transition. Because this transition is not the main transition used in slowing, repumping can occur for any laser polarization.

The two lasers required for slowing are copropagated and focused onto the last aperture with a 2 m focal length lens, see Fig. 3.12. The polarizing beam-splitter cube (PBS) ensures the polarization hitting the quarter-wave plate

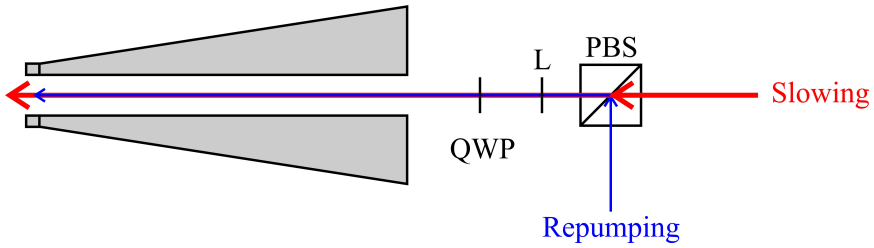

Figure 3.12: Simplified optical setup used for Zeeman slowing. The two lasers are combined on a polarizing beam-splitter cube (PBS). The beams are focused down the slower by a lens, L. The two beams are made circular by the quarter-wave plate (QWP).

(QWP) is linear. The wave plate must be properly adjusted to produce a circular polarization required for slowing. Furthermore, the slowing laser (see Fig. 3.12) must have σ^- polarization (that circular polarization which drives $\Delta m = -1$ transitions).

The Monte Carlo simulation provided the initial parameters to use for slowing. Three main pieces of the slower must be functioning as expected to achieve slowing. First, the magnetic field gradient must be what is expected. This was verified in Fig. 3.11, and now adjustable solely by the current, I, through the slower magnet. Second, the laser beams required for slowing must have known frequencies and polarizations as well as appropriate intensities. Finally, the atomic beam must be providing sufficient flux of atoms and be directed appropriately through the slower. The initial parameters that were determined in the simulation are shown in Table 3.1. Using these initial parameters, no slowing was achieved. It turned out that the malfunctioning piece of the slowing

Table 3.1: Initial Slowing Parameters

T	323 K	oven temperature
I	6 A	current in slower magnet
s	15	saturation parameter
δ_s	- 325 MHz	slowing laser detuning
δ_r	- 265 MHz	repumping laser detuning

Table 3.2: Optimized Slowing Parameters

T	373 K	oven temperature
I	6.9 A	current in slower magnet
s	7.6	saturation parameter
δ_s	- 325 MHz	slowing laser detuning
δ_r	- 285 MHz	repumping laser detuning

system was the atomic beam itself. There was simply not enough flux of atoms in the beam. Increasing the oven temperature to $T = 373$ K alleviated the problem and slowing was achieved shortly thereafter. The increased temperature of the oven required an increased magnetic field gradient and a larger repumping detuning for optimized slowing, which was to be expected. The optimized slowing parameters are given in Table 3.2.

To observe slowing of the atomic beam, the MOT was monitored with a charge-coupled device (CCD) camera that is sensitive to near-infrared light. A

small background pressure of cesium was introduced from the main chamber oven to verify the trapping fields for the MOT were functioning properly. The signature of slowing is an increase in the size (or atom number) of the MOT present from the background vapor. A comparison of the MOT loaded from the background vapor versus the atomic beam is shown if Fig. 3.13. The slower

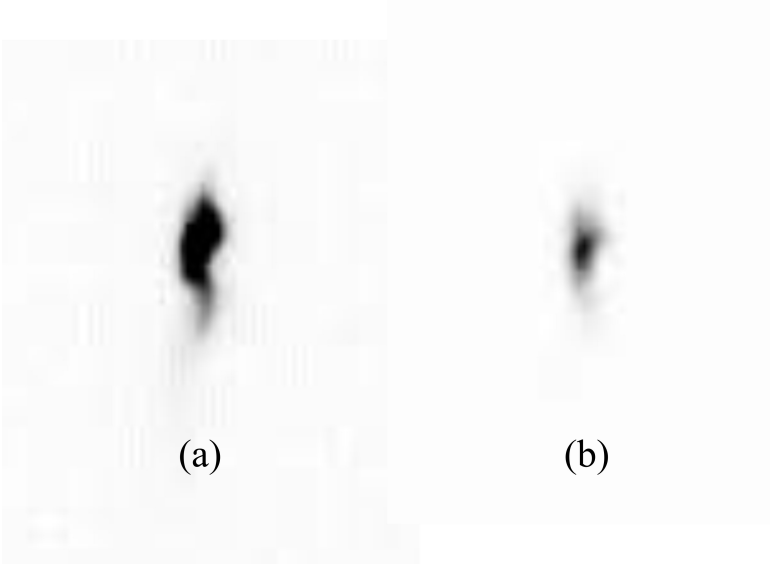

Figure 3.13: MOTs loaded from (a) the Zeeman slower or (b) the background vapor. Images were taken with the same settings.

loaded MOT is much larger and loads much more quickly than the background vapor loaded MOT. I would like to point out that slowing can also be observed, albeit not optimized, with the wave plate at 90° from the optimized setting. This corresponds to σ^+ slowing and uses the fringing fields from the MOT coils as the field gradient.

3.5 Far Off-Resonance Trap

The trapping potential of a far off-resonance trap (FORT) is far below that of a MOT. This means that atoms must be captured and cooled by some other trapping mechanism in order to have a low enough energy to be captured by the (much weaker) FORT. In order to load the most atoms into the FORT, it is advantageous to have a MOT with large atom numbers. A MOT with large atom numbers can be accomplished in our current system by either loading from the background vapor or from a slowed atomic beam. Since loading the MOT is technically easier from the background vapor (requires less equipment), the MOT was loaded in this way for all experiments in this thesis, including any situation requiring the use of the FORT.

A simplified schematic of the optics layout for the FORT is shown in Fig. 3.14. The FORT beam is combined with the z-axis of the MOT beams with a dichroic mirror (DM). The FORT beam is focused onto the MOT with a positive lens ($f = +400$ mm). The optics are arranged so that the FORT beam can be recycled and focused back onto itself creating a crossed FORT. The MOT light gets reflected off of the second dichroic mirror and the FORT light passes through it. The FORT beam is re-collimated and focused onto the first focus with an intersection angle of 22.5°. A beam dump can be inserted after the second dichroic mirror to realize a single FORT.

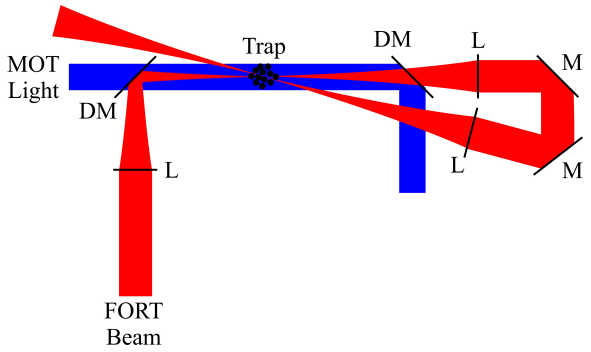

Figure 3.14: Geometry used for creation of the optical dipole traps. The fiber laser beam used for the FORT is combined with the z-axis of MOT lasers. The fiber laser beam is recycled and focused onto the first focus at an angle of 22.5°. The exiting FORT light may be blocked to realize a single FORT. The FORT light is coupled into and out of the MOT laser beams with dichroic mirrors (DM). The same lens (L) is used in focusing and recollimating the FORT light.

3.5.1 Alignment Procedure

Implementing a FORT requires very sensitive alignment of the focusing trapping laser with respect to the MOT. Alignment of the FORT beam focus can be accomplished in a variety of ways, most of which rely on the aid of a laser which is resonant with a cycling transition of the parent trap. The resonant laser is used to visually perturb the atom number in the MOT. If the resonant laser is copropagated with the FORT beam, a spatial location of the axis of the beam is easily identified, see Fig 3.15. In our particular case of a 1064 nm FORT beam and MOT laser fields at 852 nm, a PBS with the same near-infrared (NIR)

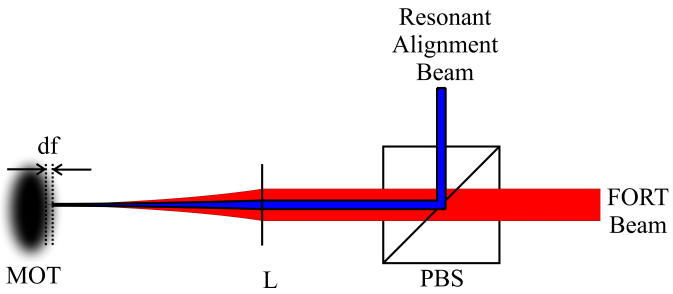

Figure 3.15: Schematic of the procedure used to align the focus of the FORT beam to the MOT. The resonant alignment beam is combined with the FORT beam with a polarizing beam-splitter cube (PBS). The resonant light is focused onto the MOT with a lens (L). The MOT is larger than the difference in focal lengths due to chromatic abberation (df).

coating may be used to combine the beams. If the two beams are carefully overlapped, visual perturbation of the MOT with the resonant laser ensures that focal position of the FORT beam is close enough to the correct position that an ac Stark shift measurement can be used for further improvement. The difference in the focal points of the two beams (df in Fig. 3.15) is smaller than the MOT, so chromatic aberration does not need to be accounted for in order to measure an ac Stark shift of the atoms due to the presence of the intense FORT beam.

The presence of the FORT beam modifies the internal states of the atom. The energy shift of the new internal states from the unperturbed states is called the ac Stark shift. Since the energy of the states is changed by the FORT beam, the beam can be used to modulate the resonance condition of atoms in its path.

The change in the resonance condition can be detected by a separate laser as shown in Fig. 3.16. To detect the ac Stark shift, a laser is scanned in the vicinity

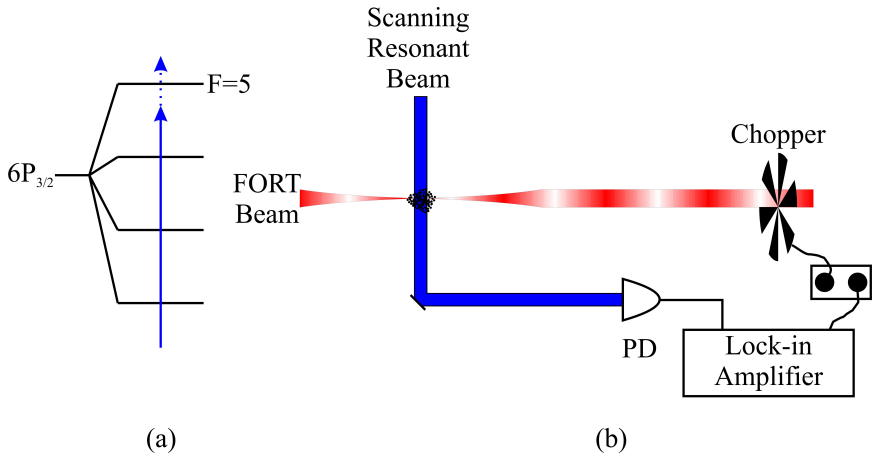

Figure 3.16: Detection of ac Stark shifted MOT atoms. A laser beam is used to scan over the transition shown in (a). The Stark shift is modulated with a chopper and the signal from a photodiode (PD) is processed with a lock-in amplifier.

of the $6S_{1/2}(F = 4) \rightarrow 6P_{3/2}(F = 5)$ transition and passed across the MOT. A very small amount of light is used so that the MOT is not perturbed. The light is detected by a photodiode (PD). As the laser is slowly scanned across the $6S_{1/2}(F = 4) \rightarrow 6P_{3/2}(F = 5)$ transition, light will be absorbed from the beam. This means the voltage signal from the PD mimics the Lorentzian shape of the absorption profile. When the FORT beam is present, the position of the absorption profile changes, which is detected by the PD. Lock-in detection of the change in resonance position is accomplished by quickly modulating the intensity of the FORT beam by passing it through a chopper wheel. The lock-in amplifier

subtracts the PD signals with the FORT beam off and on. This means one should expect to see a dispersive signal if an ac Stark shift is being detected (see Fig. 3.17). The amplitude of the dispersive signal gives information about the

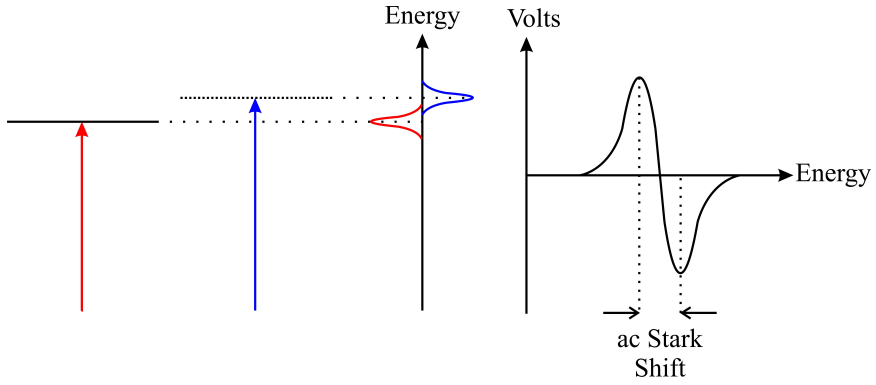

Figure 3.17: Generation of a dispersive signal due to the ac Stark shift. (a) The unshifted level (red) is shifted to a new energy (blue) by the ac Stark shift. (b) The signal with the FORT beam on is subtracted from the signal with the FORT beam off to give a dispersive signal whose peaks are separated by the ac Stark shift.

number of atoms experiencing an ac Stark shift and the separation of the peaks indicates the value of the shift experienced. Once an ac Stark shift is detected, the optics controlling the pointing of the FORT beam can be manipulated to optimize the signal. The signal is optimized when the ac Stark shift is greatest and the peak separation is maximized. An example of an optimized ac Stark shift measurement is shown in Fig. 3.18. Once a good signal-to-noise ratio is obtained, the position of the FORT focus is in an adequate position to try to

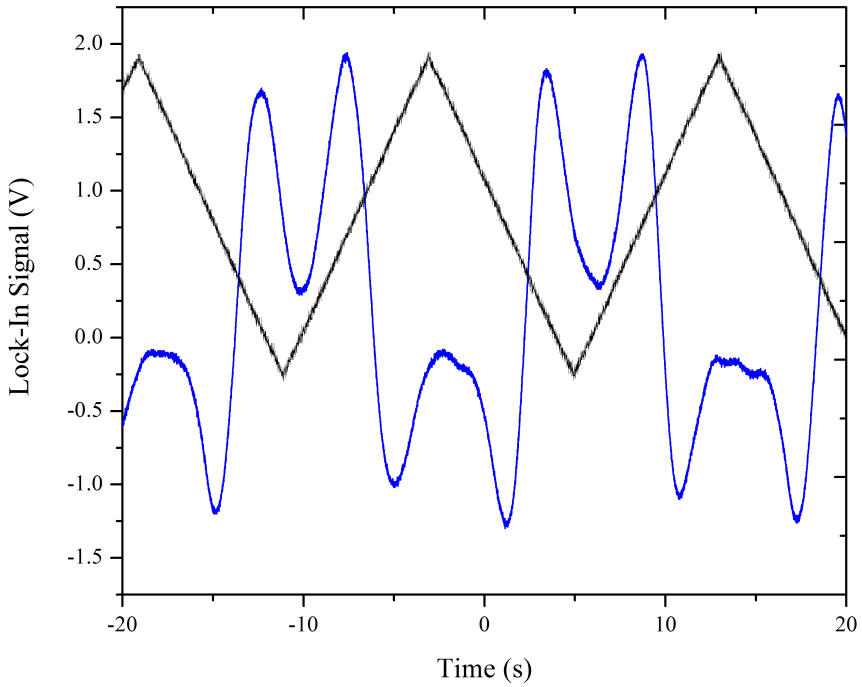

Figure 3.18: Measurement of ac Stark shifted atoms. The blue trace is the expected dispersive signal and the black trace is a voltage proportional to the laser frequency.

load the trap.

3.5.2 FORT Loading

The FORT is loaded best if a cooling stage is applied to the MOT immediately before FORT loading. The cooling stage has two advantages. Lower temperatures are obtained and the atoms are optically pumped into the absolute ground state, $6S_{1/2}(F = 3)$. Lower temperatures allow more efficient filling of the dipole trap and optical pumping suppresses inelastic two-body processes, which leads to a longer lifetime. These effects were extensively studied in the comprehensive

paper [42].

The timing sequence used to observe atoms trapped in the FORT is shown in Fig. 3.19. The MOT is first loaded to maximum atom number for 4 s. The

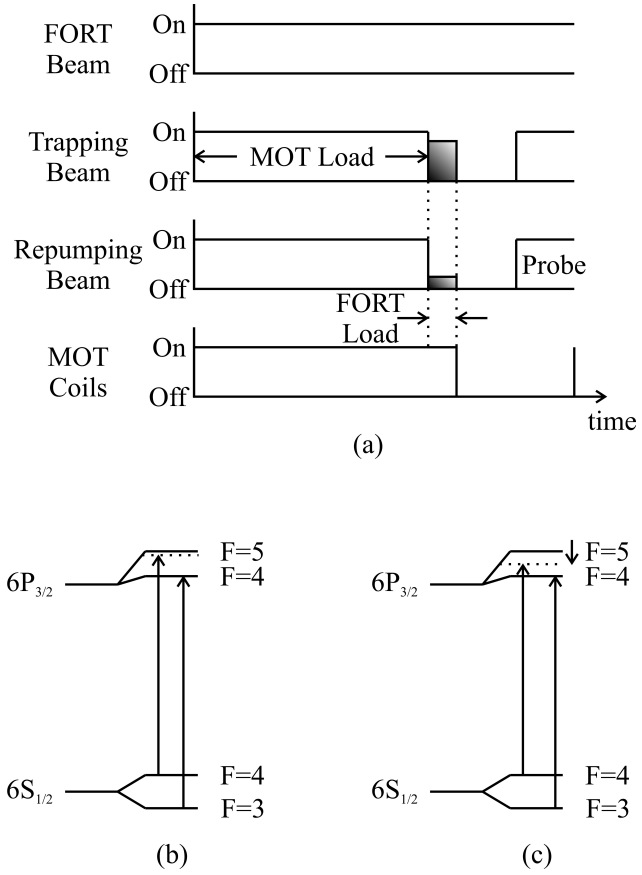

Figure 3.19: (a) Timing sequence for FORT loading and subsequent probing. (b) Laser frequencies used in MOT loading. (c) Laser frequencies used in FORT loading.

cooling stage or FORT loading stage then occurs for 40 ms. During the FORT loading stage, the MOT trapping laser is tuned further to the red by 15 MHz while simultaneously decreasing its intensity by a factor of ~ 3. The repumping

laser stays on resonance, but its intensity is reduced by a factor of ~ 100. After that time all trapping fields required for the MOT are extinguished and atoms remain trapped inside the FORT.

A fluorescence image of the atoms trapped in the FORT may then be obtained by turning on the MOT lasers (at the MOT loading parameters), but not the magnetic field. This causes resonant scattering of photons inside an optical molasses and subsequently destroys the FORT. A CCD camera can be triggered to only have exposure over this time frame acquiring a fluorescence image of the atoms as they are being expelled from the FORT. A 20 ms exposure of the

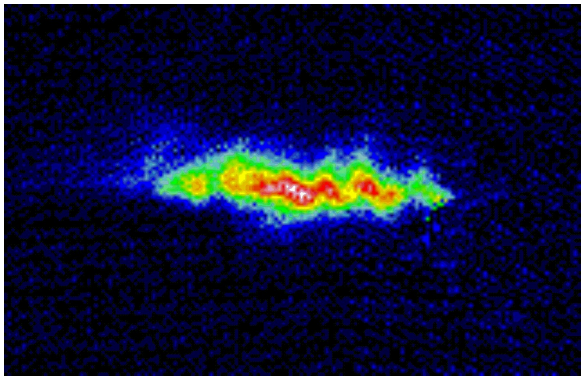

Figure 3.20: False color image of a single FORT atom fluorescence. The exposure time was 20 ms.

trapped atom fluorescence is shown (in false color) in Fig. 3.20. Because the fluorescing atoms are being pushed out of the FORT, the size of the FORT in Fig. 3.20 is somewhat inflated.

3.5.3 Trap Characterization

The geometry of the focus and power at its location determine the maximum temperature an atom can have and still be trapped. This is characterized by a parameter called the trap depth and can be calculated using the potential energy in Eq. 2.31. If an atom has exactly this much energy, it will take up the entire volume of the FORT as it is barely trapped back into oscillation about the center. Atoms with lower energies (i.e. from lower temperature distributions) than this will occupy a smaller spatial distribution. The size of the distribution generally decreases as $\sqrt{T}$ [39]. This means a FORT loaded with colder atoms or larger trap depths will generally be more dense.

The density of the single focused-beam FORT can be increased by overlapping two FORTs at an angle, creating a crossed FORT. This not only confines the atoms more tightly, but the trap depth also increases from the additional laser power. Both effects lead to an increase in density. In our system, a crossed FORT is easily realized by recycling the first FORT beam, as depicted in Fig. 3.14. Important parameters which characterize a FORT include the trap depth, trapping frequencies, lifetime, and maximum densities. These parameters are compared for a single beam FORT and a crossed beam FORT.

The trap depth of the crossed FORT is augmented only by the fact that twice the power is available. Since the trap depth of the FORT is linear in the intensity (see Eq. 2.31), the crossed FORT only has twice the maximum trap

depth of a single beam FORT. For a focused spot size of $\omega_0 = 86$ μm and 10 W of power, the single FORT trap depth is $T_{sing} = 686$ μK and $T_{cross} = 1.37$ mK. The trap depths for both configurations are shown in Fig. 3.21. The

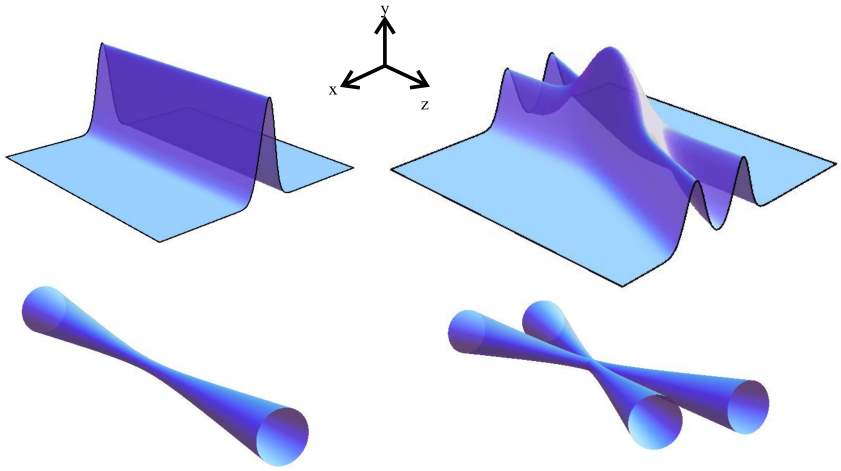

(a) (b)

Figure 3.21: Trap depths for a single FORT (a) and the crossed FORT (b). The coordinate system shown is used to calculate the trap frequencies.

trap frequencies of the single-beam FORT are readily calculated [39] with the trap depth and the spot size. The radial trap frequency is $\omega_r = 2\pi \cdot 1511$ Hz and the longitudinal trap frequency is $\omega_z = 2\pi \cdot 8.4$ Hz. To obtain the trap frequencies for the crossed-beam FORT, the trap depth (potential) minimum was fit to a harmonic oscillator. Using the coordinate system of Fig. 3.21, the trap frequencies are shown with the fits to the potential energy in Fig. 3.22. The lowest trap frequency increased from 8.4 Hz for a single beam to 481 Hz

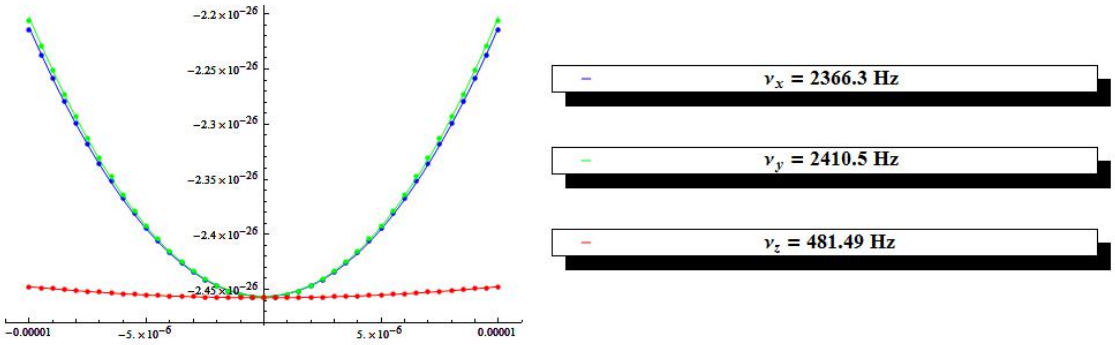

Figure 3.22: Potential energies along the three orthogonal directions shown in Fig. 3.21. Corresponding trap frequencies are shown on the right.

for the crossed configuration. The increase in trap frequencies in the crossed configuration is advantageous in applications such as evaporative cooling due to faster re-thermalization.

The lifetime of the FORT is determined by measuring the amount of fluorescence the trapped atoms produce for various holding times in the trap. The fluorescence is measured with a photo-multiplier tube (PMT). The peak voltage produced by the PMT is used as the indication of the number of atoms in the trap [43]. The lifetimes for a single FORT and a crossed FORT are compared in Fig. 3.23. Because both trapping configurations were loaded in the same way with equivalent background pressures, the difference in lifetime is attributed to density dependent effects such as three-body recombination. The maximum density can be estimated from the measured number of atoms and the size of the trapping region. The maximum density in a single FORT is $\sim 2.5 \times 10^{12}$

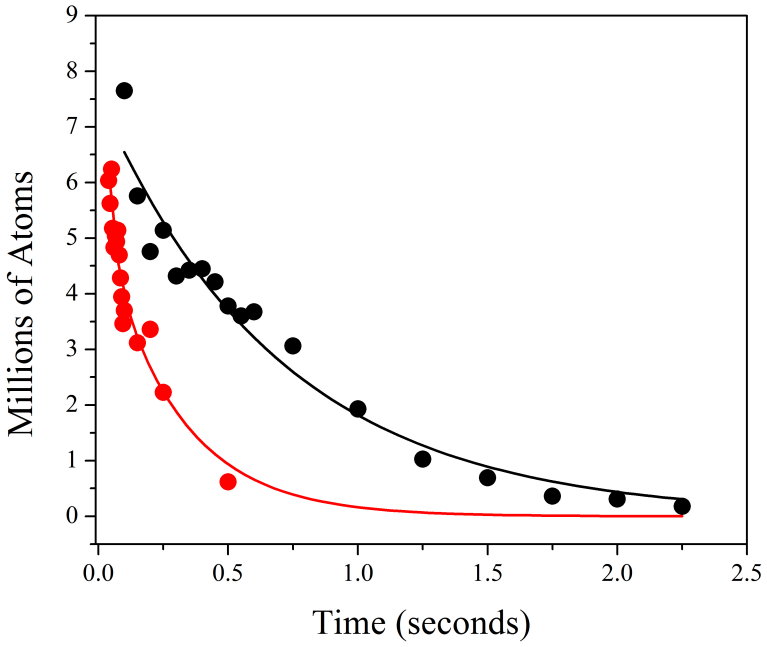

Figure 3.23: Measurement of the lifetime of atoms trapped in the FORT. The black circles are for a single FORT and the red circles are for the crossed FORT. The curves are exponentially decaying fits to the data. The single FORT $(1/e)$ lifetime is 800 ms and the crossed FORT lifetime is 190 ms.

cm^{-3} and the maximum density available in the crossed FORT is $\sim 2 \times 10^{13}$ cm^{-3}. An absorption image of the crossed FORT is shown in Fig. 3.24.

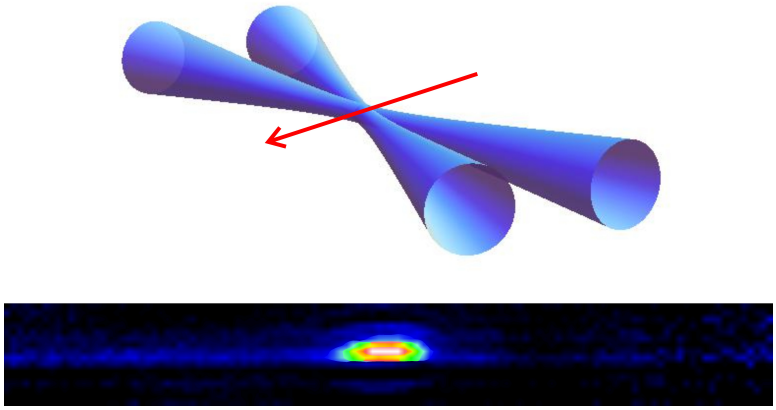

Figure 3.24: Absorption image of the crossed FORT. *top* Both arms of the crossed FORT and the absorption imaging beam are in the same plane. *bottom* False color absorption image of the crossed FORT. From this angle the plane containing all of the lasers is a line in the center of the image.

Chapter 4

Rydberg Atoms and Rydberg Tagging

4.1 Introduction

Rydberg atoms are atoms with large principal quantum number n. In highly exited states, an electron will be very far away from the nucleus. For this reason Rydberg atoms have exaggerated properties. These include large atomic radii, long lifetimes, and large transition dipole moments to nearby states. Rydberg atom interactions with external fields and with each other have opened up new and exciting avenues of research including quantum computation schemes [2, 3, 5, 44] and ultra-sensitive electric and magnetic field sensors [45]. Because Rydberg atoms can be perturbed at large distances, exotic diatomic molecules involving Rydberg atoms can be created. *Macrodimers* are Rydberg atom - Rydberg atom molecules with bonding lengths on the order of microns [16]. So called trilobite states have recently received much attention as well [24, 23, 22]. These strange molecules contain a ground state atom bound to a Rydberg atom through the scattering of the Rydberg atom electron off of the ground state atom. These trilobite states are homonuclear diatomic molecules with permanent electric dipole moments. The qualitative features of most of these systems can be ascertained by relatively simple approaches.

4.2 Physics of Rydberg Atoms

4.2.1 Quantum Defects

The Rydberg atoms described in this thesis are cesium Rydberg atoms and therefore only have one valence electron. This similarity to hydrogen lead to the description of the alkali Rydberg atoms in terms of quantum defects [1]. When comparing hydrogen and cesium Rydberg states (see Fig. 4.1), the main difference is the presence of an ionic core in cesium containing 55 protons and 54 electrons. If the excited electron is very far away from the core, it is only sensitive

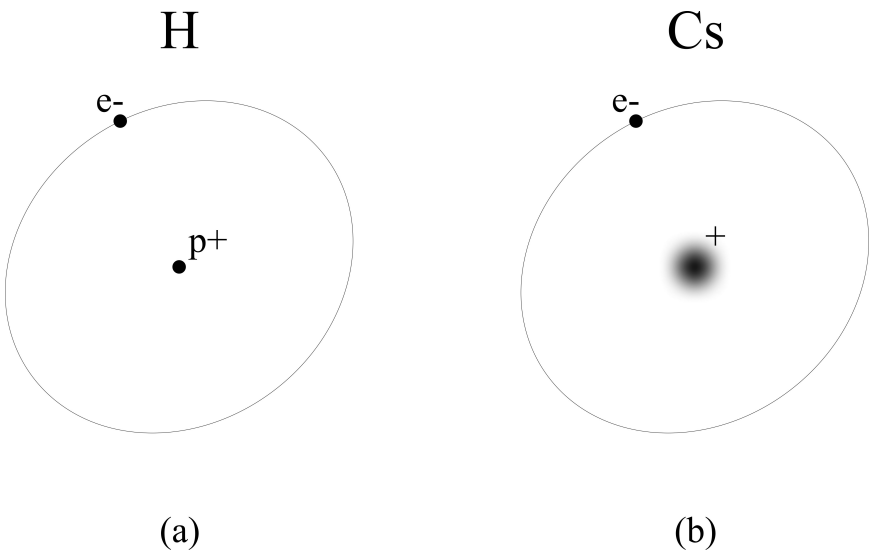

Figure 4.1: (a) A hydrogen Rydberg atom. At the center of the atom, only the nucleus is found. (b) A cesium Rydberg atom. At the center of the atom is a core of 54 tightly bound electrons around a nucleus with 55 protons.

to the net charge of the core so we would expect hydrogen and cesium Rydberg

states to behave similarly. On the other hand, if the electronic wavefunction has significant probability to approach or even penetrate the core, we would expect the exact distribution of charge in the core to have an effect. This is indeed the case for the lower angular momentum Rydberg states ($l \leq 3$), whose wavefunctions have maxima very close to $r = 0$ (or at $r = 0$ in the case of nS Rydberg states). The excited electron in these low l states can polarize and penetrate the ionic core, leading to lower energies of the alkali Rydberg states compared to the hydrogen counterparts. The Rydberg atom energies, E_{nlj}, are given by

$$E_{nlj} = -\frac{Ry}{(n - \delta_{nlj})^2}, \tag{4.1}$$

where Ry is the atomic Rydberg constant ($Ry_{Cs} = 3.29 \times 10^9$ MHz) and δ_{nlj} are the quantum defects. The quantum defects not only depend on l and j, but are also weakly dependent on n.

$$\delta_{nlj} = \delta_0^{(lj)} + \frac{\delta_2^{(lj)}}{(n - \delta_0^{(lj)})^2} + \frac{\delta_4^{(lj)}}{(n - \delta_0^{(lj)})^4} + \ldots \tag{4.2}$$

The quantum defects are determined empirically to high accuracy with high resolution spectroscopy. The values of the quantum defects for cesium were determined in [46, 47] and are summarized in Table 4.1.

4.2.2 General Properties

More generalized properties of Rydberg atoms can be calculated with the wavefunction of the excited electron. In order to compute the wavefunction, a model

Table 4.1: Cesium Quantum Defects

	$S_{1/2}$	$P_{1/2}$	$P_{3/2}$	$D_{3/2}$	$D_{5/2}$	$F_{5/2}$	$F_{7/2}$
δ_0	4.049	3.592	3.559	2.475	2.466	0.033	0.033
δ_2	0.237	0.360	0.374	0.555	0.014	-0.199	-0.191

potential for the core must be used that accurately reproduces the empirically measured energies. We adopt the l-dependent parametric model potential given by Marinescu *et al.* [48], which is shown below.

$$\begin{aligned} V_l(r) &= \frac{Z_l(r)}{r} - \frac{\alpha_c}{2r^4}\left[1 - e^{-(r/r_c)^6}\right] \\ Z_l(r) &= 1 + (Z-1)e^{-a_1 r} - r(a_3 + a_4 r)e^{-a_2 r} \end{aligned} \tag{4.3}$$

The core has a static polarizability, α_c, and contains Z protons. The a_i are fitting parameters used to match the empirically measured energies. The non-physical effects of the model potential at $r = 0$ are removed by a cutoff radius, r_c. Parameters for all of the alkali metals at all values of l are given in [48]. This model potential is put into the existing RADIAL [49] program. The modified program is used to solve the 1D Schrödinger equation and obtain radial wavefunctions of any Rydberg state of interest. Using the Rydberg atom wavefunctions and energies, useful n scaling laws may be generated. Important parameters characterizing Rydberg states and how these parameters scale with n are shown in Table 4.2. It should be noted that when considering Rydberg states with quantum defects, n in the Table 4.2 should be replaced with $n^* = n - \delta_{nlj}$.

Because Rydberg atoms have large transition dipole moments to neighboring

Table 4.2: Scaling laws of alkali Rydberg atoms.

Quantity	Symbol	Scaling
Radius	$\langle r \rangle$	n^2
Transition Dipole	$\langle nl \vert er \vert nl' \rangle$	n^2
Polarizability	α	n^7
Van der Waals Interaction	C_6	n^{11}
Radiative Lifetime	τ_r	n^3

states, their lifetime can be greatly shortened due to the interaction of the Rydberg state with thermal background radiation. Objects (like pieces of apparatus) emit blackbody radiation that is characteristic of its temperature. At room temperature, significant power density lies in the millimeter and radio-frequency ranges and can easily couple to nearby Rydberg states. This depopulation leads to a shorter lifetime and can be expressed as

$$\tau = \left(\frac{1}{\tau_r} + \frac{1}{\tau_{bb}} \right)^{-1}. \tag{4.4}$$

The lifetimes, including blackbody radiation, are calculated in this thesis as recently described in Beterov *et al.* [50]. The radiative and blackbody contributions have empirically based expressions given by

$$\begin{aligned} \tau_r &= \tau_s \left(n^*\right)^{\delta} \\ \tau_{bb} &= \frac{A}{\left(n^*\right)^{D}} \frac{2.14 \times 10^{10}}{\exp(315780 B / \left(n^*\right)^{C} \times T/K) - 1}, \end{aligned} \tag{4.5}$$

where, τ_s, δ, A, D, and C are optimized parameters that depend on the atomic species as well as the angular momentum of the electron l, and j. Note the

exponent in the radiative lifetime is remains within 1% of 3 for all l and j, as indicated in Table 4.2. As will be shown in Chapter 5, the beam used for the far off-resonant trap causes significant photoionization of the Rydberg atoms, shortening their lifetime even further.

4.3 Rydberg Tagging Time-of-Flight Imaging

Rydberg atoms were used to establish the velocity resolution of our system. Creating Rydberg states for the purpose of ionizing in a weak electric field is sometimes called Rydberg tagging and the ability to measure product yield and velocities is well established [51, 52, 53, 54]. Rydberg tagging is used in the present experiment to measure the temperature of atoms in the MOT. We demonstrate that sub-Doppler temperatures are easily measured with this experimental technique and that the temperature of the MOT may be determined non-destructively, in contrast to standard imaging techniques.

The temperature of trapped atoms inside of a MOT varies linearly with light-shift when the light-shift is small and does not contribute to multiple scattering of photons [28]. The temperature may be written

$$\begin{aligned} T(\Lambda) &= T_0 + 2C_\sigma T_D \Lambda, \\ \Lambda &= \frac{\Omega^2}{|\delta|\Gamma} \end{aligned} \tag{4.6}$$

where the light-shift parameter, Λ, is the ac Stark shift of the atoms due to the trapping light (in units of $\hbar\Gamma$). T_0 is the minimum temperature attainable, T_D

is the Doppler temperature (125 μK for Cs [31]), and C_σ is a constant to be determined and compared with previous values. The Rabi frequency for the transition, Ω, is computed from the intensity of the trapping beams, I, as

$$\Omega = \Gamma\sqrt{\frac{I}{2I_s}}, \tag{4.7}$$

where $I_s = 1.1$ mW cm^{-2} is the saturation intensity for the transition and $\Gamma = 2\pi \cdot 5.22$ MHz is the natural linewidth.

The general method to measure the temperature is to excite Rydberg atoms within the MOT and let them expand for a variable time before acquiring arrival time-of-flight distributions. The expansion of the time-of-flight distribution with variable expansion time indicates the temperature.

4.3.1 Experimental Setup

Because the temperature depends on the light-shift parameter, the detuning and intensity of the trapping laser must be accurately known. The intensity of the trapping laser is measured with a power meter and the beam size was measured with an iris. The detuning of the trapping laser is monitored with a 2 MHz scanning Fabry-Pérot interferometer (FPI). Atoms are excited to $89D_{5/2}$ Rydberg states with linearly polarized green light from a narrow linewidth (~ 1.4 MHz) Coherent 699-21 ring dye laser operating at 508.66 nm. The green light is sent through an acousto-optical modulator (AOM) for switching and coupled into a single-mode polarization-preserving fiber. The output of the fiber is focused

through the MOT with a focal spot of $\Delta z_0 = 104\ \mu\text{m} \pm 7\mu\text{m}$, verified by a CCD camera, see Fig. 4.2. The intensity of the green light is adjusted so that $\ll 1$ Rydberg atom is detected per pulse.

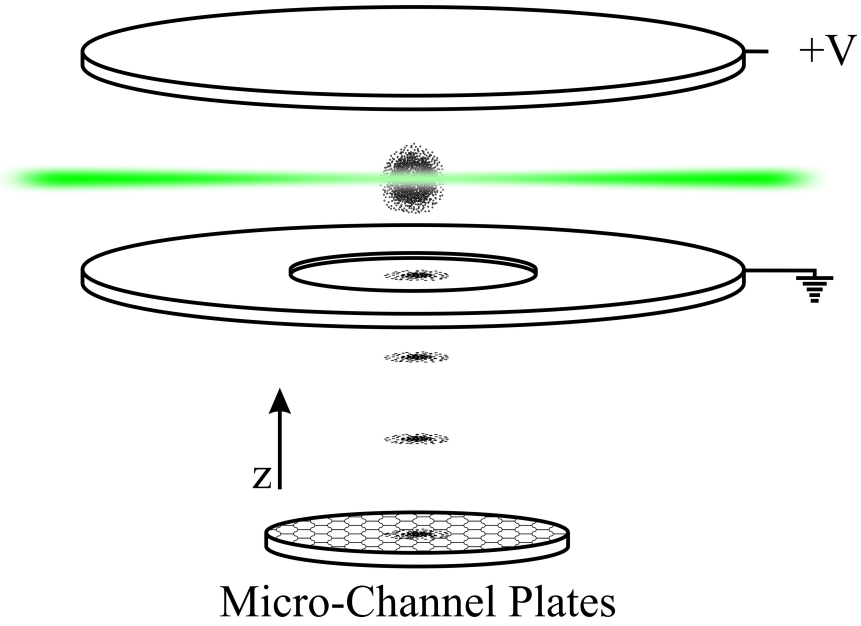

Figure 4.2: Cartoon of the excitation region. The green laser excites Rydberg atoms (one at a time) and the Rydberg atom begins drifting away at its thermal velocity. The expansion takes place for variable amounts of time before pulsed-field ionization (PFI) is used to project the positive ion downward to get detected. The size of the cloud hitting the detector is indicative of the atomic temperature.

Once a Rydberg atom is created, it is decoupled from the MOT trapping potential and begins expanding at its thermal velocity. After a variable time, $\Delta\tau$, the Rydberg atom is projected onto the micro-channel plates (MCPs) by pulsed-field ionization (PFI). This is repeated several times to accumulate a

time-of-flight (TOF) distribution. Because the atom is in a high-lying Rydberg state, a small electric field pulse is used (53 V cm^{-1}) for ionization of the Rydberg state which has negligible effects on the trapped atoms. The weakly bound Rydberg electron also gives a negligible recoil to the atom as it is ripped away, which does not alter the time-of-flight. The ionizing electric field pulse delivers a momentum kick to the (positive) ion. Because the ions are only accelerated for a small time, there is a linear mapping of the velocity onto the width of the TOF distribution.

Extreme care must be taken to ensure that only one Rydberg atom is created with each laser pulse. If two Rydberg atoms are present, PFI will create two ions and they will repel each other during their time-of-flight and lead to wider TOF distributions. For this reason, the detection rate of the ions ($\lesssim$ 25 Hz) is made much less than the repetition rate of the experiment (1 kHz), by adjusting the green laser intensity. Multiple ion counts are also filtered out electronically, see Fig. 4.3. The MCP detector generates fast timing signals and a signal proportional to the amount of charge striking it. When two ions hit the detector, the height of the charge signal is twice as high as a single ion count. The charge signal is analyzed with a single-channel analyzer (SCA) which can differentiate single ion counts from multiple ion counts with voltage thresholds. Single ion counts are accepted by the SCA and subsequently trigger a gate from a waveform generator. The gate and processed fast timing pulses arrive at a delay generator.

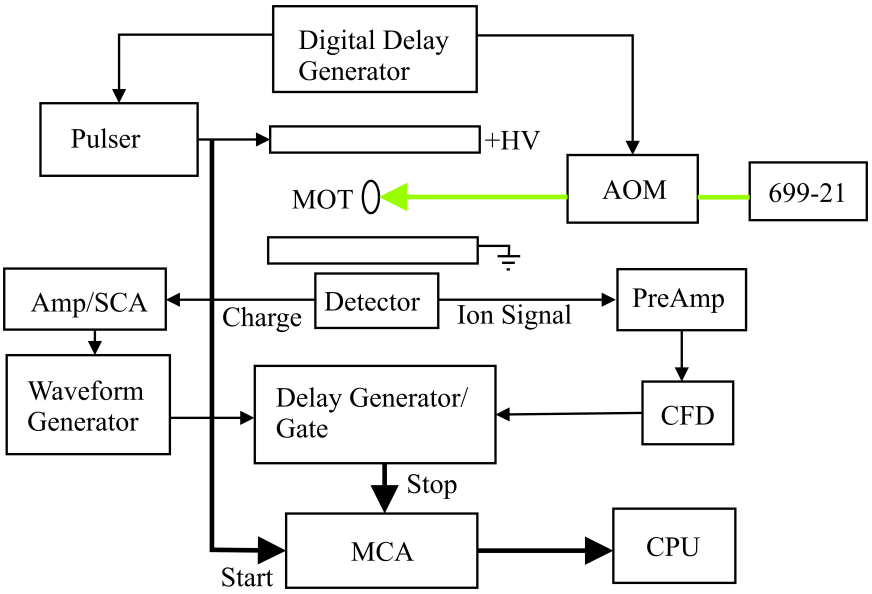

Figure 4.3: Experimental signal processing. Ions hit the detector and two signals are generated: a fast timing signal (right side) and a charge signal (left side). The Amp/SCA filters out charge signals corresponding to too much charge. Charge signals passing through the filter create a gate that is sent to a delay generator. Here, the gate picks out the fast timing signals with the correct charge signal amplitude. A stop is generated for the MCA if the charge corresponds to a single ion hitting the detector. The critical timing interval is between the starts and stops for the MCA because this interval is the ion TOF and determines the velocity distribution. CFD is the constant fraction discriminator, AOM is the acouso-optic modulator, CPU is the central processing unit, and Computer, PD is the photodiode.

A digital AND circuit is used to accept only those fast timing pulses that correspond to single ion detections. The MCA starts recording the time-of-flight at the beginning of the PFI pulse and stops recording when a single ion fast timing pulse is received. Several TOF distributions are recorded on the computer for each value of expansion time, $\Delta\tau$. An example of an experimental TOF distribution is shown in Fig. 4.4. The distribution in Fig. 4.4 corresponds to an

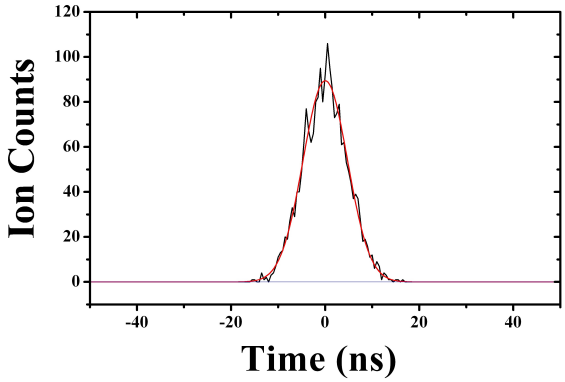

Figure 4.4: A TOF distribution taken at $\Delta\tau = 220$ μs with 3019 total ion counts. The smooth solid curve is a Gaussian fit to the experimental data. These data are taken from a curve with $T = 40$ μK.

expansion time of $\Delta\tau = 220$ μs from a $T = 40$ μK measurement. The spatial extent of the time-of-flight distribution may be obtained by multiplying with width of the distribution in time by the velocity of the ions as they travel down the flight tube. The velocity of the ions is found by dividing the distance they travel to the detector (~ 265 mm) by the average time-of-flight (26.958 μs). The full-width at half-maximum (FWHM) in time of the distribution shown in Fig.

4.4 is 11.01 ns ± 0.04 ns, as determined by a Gaussian fit. The spatial extent of the cloud is then 109.0 μm ± 0.5 μm, indicating an expansion of 5 μm in 220 μs. Several TOF Distributions acquired at different expansion times are used to obtain the temperature.

In order to deduce the temperature, the change in the cloud size, Δz, must be related to the expansion time, $\Delta\tau$. The relation may be found by examining the theoretical distribution in phase space. A cylindrical excitation region is formed by the overlap of a focused Gaussian beam and the MOT, see Fig. 4.2. The thermal distribution for the atoms inside the excitation volume is modeled as

$$f(\mathbf{r};\mathbf{v},\Delta\tau) \propto \prod_{i=x,y,z} e^{-(i-v_i\Delta\tau)^2 4\ln(2)/\Delta i^2} e^{-mv_i^2/2k_BT}. \tag{4.8}$$

Δi is the FWHM of the focal spot size in the i direction, $\Delta\tau$ is the delay time of the extraction pulse, k_B is Boltzmann's constant and T is the temperature of the atoms in the trap. If we choose the pulsed-field to be in the z direction, then the spatial distribution is obtained by integrating Eq. 4.8 over all velocities and x and y. The resulting spatial distribution is

$$f(z,t) \propto e^{-mz^2 4\ln(2)/\Delta z^2}. \tag{4.9}$$

This distribution is Gaussian with a FWHM of [55]

$$\Delta z = \sqrt{\Delta z_0^2 + \frac{8\ln(2)\,k_BT}{m}\,\Delta\tau^2}. \tag{4.10}$$

Here Δz_0 is identified as the Rydberg cloud FWHM at zero expansion time, or

the focal spot size of the excitation laser. Eq. 4.10 is the non-linear fit function used to determine the free parameters Δz_0 and T.

Many TOF distributions are acquired for different expansion times for a given value of Λ. An example of the expansion of the Rydberg atom cloud for $\Lambda = 0.56$ is shown in Fig. 4.5. At each value of $\Delta\tau$ several TOF distributions

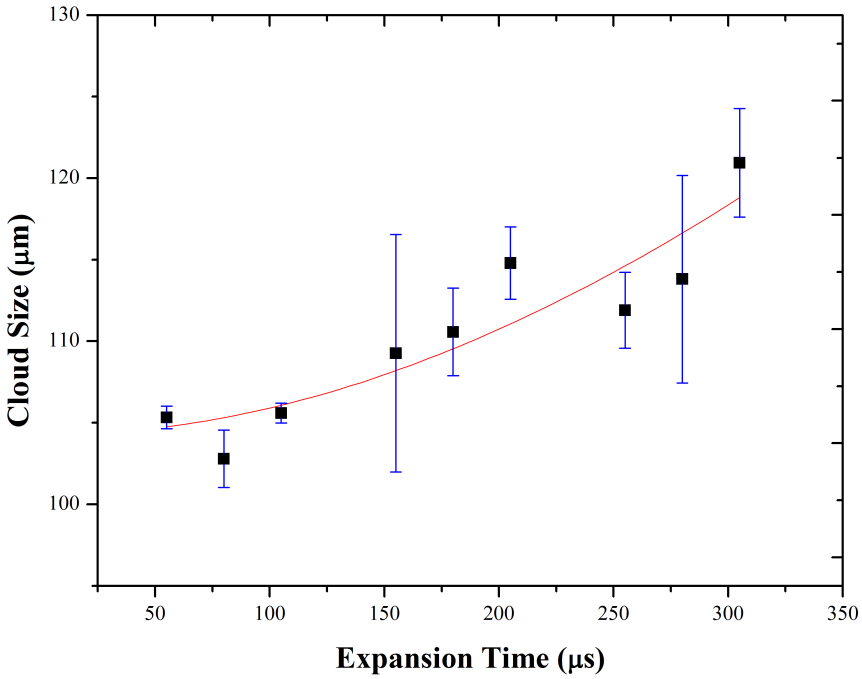

Figure 4.5: An experimental measurement of the temperature for $\Lambda = 0.56$. The error bars represent the standard deviation of at least three identical measurements. The data are fit to Eq. 4.10 with T= 84 μK $\pm$ 7 μK and $\Delta z_0 = 104$ μm $\pm$ 1.4 μm .

are acquired. The error bars in Fig. 4.5 represent the standard deviation of the measured widths. The data are fit to Eq. 4.10 with T=84 μK $\pm$ 7 μK and $\Delta z_0 = 104$ μm $\pm$ 1.4 μm. This measurement demonstrates that sub-Doppler

temperatures may be measured with the Rydberg tagging technique presented here, but its accuracy and limits must be tested. In order to test both of these aspects, temperature measurements were carried out at many vales of Λ in order to compare results with the literature. It is also interesting to note that this measurement of the spot size of the laser is more accurate than the CCD camera measurement.

The detuning and intensity of the trapping laser are used to change the light-shift parameter. For each value of Λ, the temperature is measured several times to acquire a standard deviation. Many values of the light-shift parameter are studied to produce a graph of T vs. Λ. The results are shown in Fig. 4.6. The data are fit to Eq. 4.6 to extract the free parameters T_0 and C_σ. These parameters have been measured before for Cs [56, 43] and are compared with results from the fit in Table. 4.3. The values of the slopes (C_σ) for all

Table 4.3: Sub-Doppler Cooling Parameters

C_σ	T_0	Ref.
0.24±0.07	2.6±0.4 μK	[56]
0.28±0.05	1.2±0.4 μK	[43]
0.25±0.05	3.8±3.3 μK	This Work

measurements agree. Our experimental setup (at the time) did not allow trapping laser detunings larger than -5Γ, so the minimum light-shift parameter accessible was ~ 0.15. Previous experiments [56, 43], were able to access much lower values

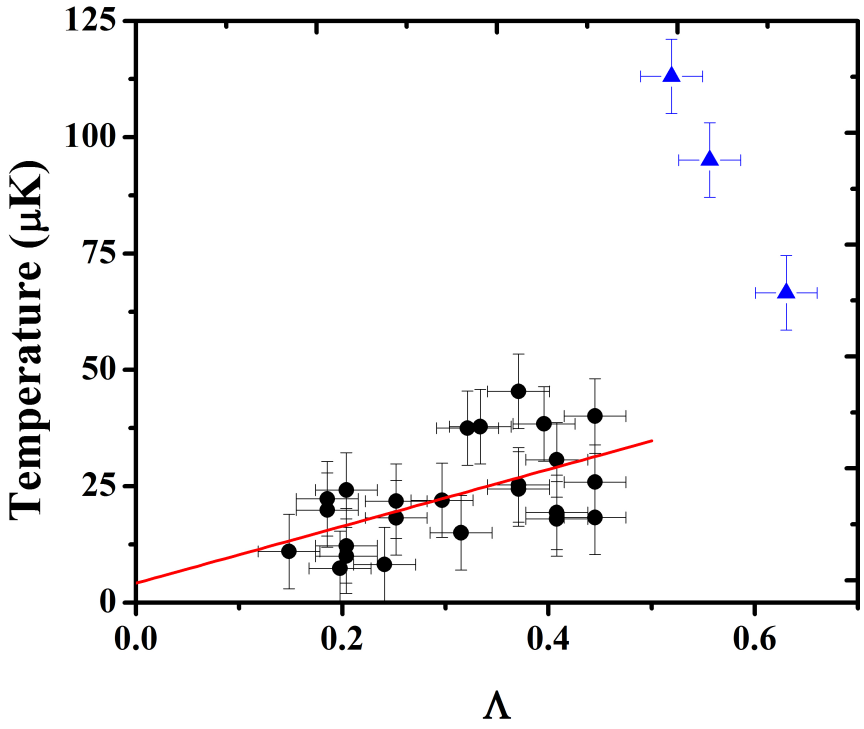

Figure 4.6: Temperature vs light-shift parameter. Several values of detuning are included. The solid line represents a fit of the data to Eq. 4.6. Data taken in the multiple scattering regime where the sub-Doppler mechanisms are not as effective are labeled by blue triangles. The error bars reflect the estimated experimental error at each different laser detuning.

of Λ and could locate the intercept, T_0, with much higher accuracy. Our value of T_0 agrees, but encompasses both previously measured values.

The Rydberg tagging method demonstrates the capability to measure very low temperatures with high accuracy. The lowest temperatures measured are $T = 7\ \mu\text{K} \pm 3\ \mu\text{K}$, corresponding to a velocity of < 3 cm s^{-1}. This is the highest

velocity resolution achieved by Rydberg tagging to date [51, 52, 53] and sets a benchmark for our velocity resolution for further experiments.

Chapter 5

Photoionization of Rydberg Atoms

5.1 Introduction

As shown in the previous chapter, most properties of Rydberg atoms can be calculated using the atomic wavefunctions and energies. The energies are calculated from the quantum defects and the wavefunctions are calculated using a parameterized potential energy function. Both the quantum defects and the potential energy have empirical input so experimental tests of their accuracy are very important. One such experimental test is measurement of the Rydberg atom lifetimes. This was done using ultracold rubidium atoms by three groups [9, 10, 11, 57]. The study of the Rydberg lifetimes in ultracold cesium was limited to the principal quantum numbers $30 \leq n \leq 40$ [58].

Rydberg atoms have recently received much attention for their roles in exotic molecules [16, 22, 59, 23]. High densities are a requirement for investigating these molecules, and far off-resonance traps (FORTs) provide high density and do not require the ground state (trapped) atoms to be spin-polarized. However, the intense trapping field from the FORT beam can photoionize the Rydberg atoms, so it is important to measure this effect.

Rydberg atoms are also being used in the development of neutral atom quantum gates [2, 60, 4, 61]. For quantum gate schemes such as [4, 61], single

qubit operations are performed in a 1064 nm FORT or lattice using high-lying Rydberg states. The performance of multiqubit gates depends strongly on the lifetime of the Rydberg atoms, which is substantially modified by photoionization. In fact, photoionization of Rydberg states serves as a method of detection in these experiments [2, 60, 4, 61].

This chapter describes the measurement of cesium Rydberg atom lifetimes inside of a MOT and inside a FORT, where photoionization plays an important role. A systematic study of the Rydberg atom lifetimes of cesium $nD_{5/2}$ states where $50 \leq n \leq 75$ is performed with and without the presence of the FORT beam to extract the Rydberg atom depopulation rates just to photoionization. The results are compared with theoretical values [50, 60].

5.2 Modification of the Rydberg Atom Lifetime

Inside of the MOT (with no FORT beam), the total decay rate out of the Rydberg state is the sum of the radiative decay rate, γ_r, and the blackbody decay rate, γ_{bb}. The lifetime of Rydberg atoms in the MOT, τ_{MOT}, is the inverse of this decay rate and is given in Eq. 5.1.

$$\tau_{MOT} = (\gamma_r + \gamma_{bb})^{-1} \tag{5.1}$$

Inside of the FORT, the intense field of the trapping laser causes significant photoionization of Rydberg atoms, which leads to a decreased Rydberg atom lifetime. To calculate the effect of photoionization on the Rydberg atom lifetime,

the photoionization cross section, σ_{PI}, is calculated according to [1],

$$\sigma_{PI} = \frac{2\pi^2}{c}\frac{\hbar e^2}{m}\frac{df}{dE}\bigg|_{E=E_r+\hbar\omega}. \tag{5.2}$$

E_r is the energy of the Rydberg state, $\hbar\omega$ is the photon energy of the FORT laser and the electron mass and charge are given respectively by m and e. This form of the photoionization cross section sums over the magnetic sublevels. The oscillator strength distribution, df/dE, can be expressed as [1, 62]

$$\frac{df}{dE} = \sum_{L=L_r-1}^{L=L_r+1} \frac{2m\omega L_{max}}{3\hbar(2L_r+1)}\left|\int \psi_{n,l}(r)\, r\, \phi_{L,E}(r) dr\right|^2. \tag{5.3}$$

L_r is the orbital angular momentum of the Rydberg state, L is the orbital angular momentum of the continuum state, and L_{max} is the greater of L and L_r. The wavefunction of the Rydberg state is $\psi_{n,l}(r)$, and $\phi_{L,E}(r)$ is the continuum wavefunction at energy, E.

The bound and continuum wavefunctions are calculated numerically with RADIAL [49], modified with the l-dependent potential [48]. The continuum wavefunctions are normalized per unit energy according to,

$$\phi_{L,E} = \sqrt{\frac{2m}{\pi\hbar^2 k}}\Phi_{L,E}(r), \tag{5.4}$$

where $\Phi_{L,E}(r)$ is the continuum wavefunction from RADIAL and $k = \hbar^{-1}\sqrt{2mE}$. Using the photoionization cross section from Eq. 5.2, the average photoionization rate, γ_{PI}, is given by

$$\gamma_{PI} = \frac{I}{\hbar\omega}\sigma_{PI}. \tag{5.5}$$

The average intensity of the trapping laser over the excitation region is I. Since the intensity of the laser is a function of space, atoms at different locations in the trap will have different photoionization rates. A Gaussian intensity distribution for the FORT laser is used to compute the average intensity.

Inside the FORT, the photoionization rate adds to the existing radiative and blackbody decay rates so that the reduced Rydberg atom lifetime in the FORT is simply expressed by

$$\tau_{FORT} = \left(\gamma_r + \gamma_{bb} + \gamma_{PI}\right)^{-1}. \tag{5.6}$$

Since the MOT and the FORT are in the same locations, the radiative and blackbody decay rates for a given Rydberg state can be determined by measuring the lifetime in the MOT from Eq. 5.1. By measuring the lifetime of the same Rydberg state in the FORT, the photoionization rate may be determined and compared to theory. In the next Section, I will describe the experimental details of the FORT preparation and the method used to extract the photoionization rate.

5.3 Experimental Details

5.3.1 FORT Preparation

To prepare the FORT, a MOT is prepared with cesium atoms loaded from a background vapor. The trapping light is provided by the tapered-amplifier system described in Sec.3.3.2. The repumping light is provided by the external-

cavity diode laser system shown in Sec.3.3.1. The frequency and intensity of all MOT lasers are controlled with acousto-optic modulators (AOMs). The magnetic field at the MOT location is minimized by three sets of orthogonal coils. Canceling the magnetic field maximizes the viscous damping provided by the MOT lasers when the quadrupole field is off (optical molasses).

A FORT is prepared at the focus of a 10 W fiber laser operating at 1064 nm. The focused $(1/e^2)$ spot size is 86 μm $\pm$ 1.1 μm, which was measured with a CCD camera. For 7.5 W of power at the MOT location, the FORT depth is 670 μK. The radial trap frequency is $\omega_r = 2\pi \cdot 1.5$ kHz and the axial trap frequency is $\omega_z = 2\pi \cdot 8.4$ Hz. To load the FORT, the MOT is loaded to maximum atom number in 1.36 s. The FORT is loaded with the additional cooling phase described in detail in Sec. 3.5.2. At the end of the cooling phase, the quadrupole field is shut off in 220 μs by the insulated-gate bipolar transistor (IGBT) circuit described in Sec. 3.2.2. The FORT is loaded to a maximum number density of 2.5×10^{12} cm^{-3}. This is the density of a single beam FORT, as opposed to the crossed FORT used later.

5.3.2 Experimental Method

To measure the depopulation rate of $nD_{5/2}$ Rydberg atoms due to photoionization, γ_{PI}, the Rydberg atom lifetime is measured twice for each state; once in the MOT and once in the FORT. The lifetime in the MOT measures the depopulation due to radiative decay to the ground state, γ_r, as well as blackbody decay to

other Rydberg states and serves as a control experiment for the FORT lifetime measurement. The lifetime in the FORT is decreased only by the additional photoionization depopulation rate so a lifetime measurement in the FORT yields γ_{PI}.

Atoms prepared either in the MOT or in the FORT are excited to high-lying $nD_{5/2}$ Rydberg states, $50 \leq n \leq 75$, by a two-photon process. The first step of excitation is an infrared (IR) photon and final Rydberg excitation is achieved by absorption of a ~ 509 nm, green photon. The excitation frequencies required for the MOT and FORT lifetime measurements vary slightly, see Fig. 5.1. The IR light in the MOT experiment is provided by the trapping laser. An independent external-cavity diode laser (exactly the same as the repumper design) is used for the IR light in the FORT experiment. The green light has a linewidth of ~ 1.5 MHz and is linearly polarized. The laser beam passes through an AOM before being coupled into a single-mode polarization preserving fiber. The fiber output is focused through the trapped atoms with a spot size of 58 μm $\pm$ 1.0 μm. The two-photon intensity is adjusted so that, on average, one Rydberg atom is excited per laser shot.

After Rydberg excitation, the atoms are ionized by an electric field ramp that is nearly linear in time. This is done with two series capacitors (0.1 μF 3000V) used to integrate a square electric field pulse. The linear ramp temporally separates different principal quantum states in the time-of-flight (TOF) distribution. The amplitude of the electric field ramp is set just above

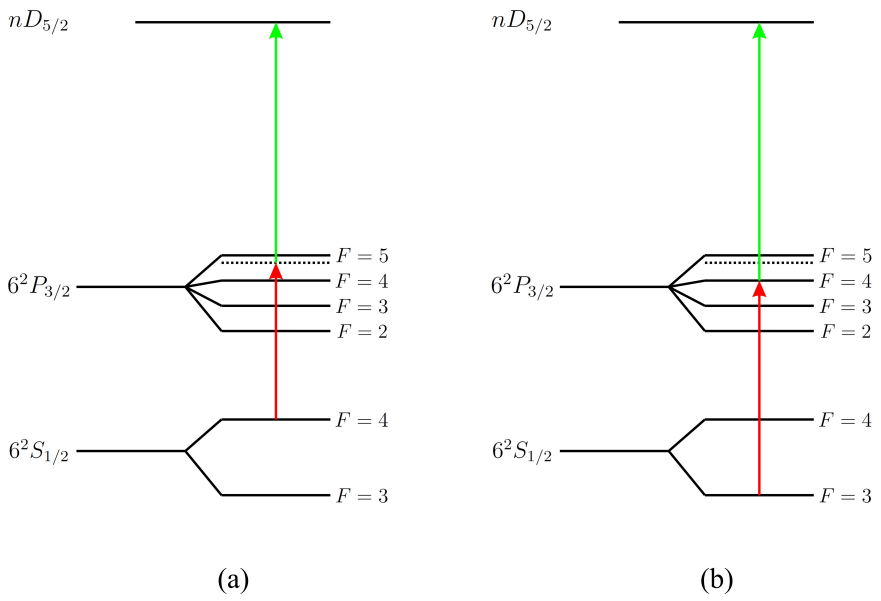

Figure 5.1: (a) Excitation scheme used in the MOT Rydberg atom lifetime measurements. The MOT trapping laser is used as the IR photon. (b) Rydberg atom excitation scheme used in the FORT. A separate laser is used as the IR photon which is tuned to compensate for the local ac Stark shift of the atoms.

the ionization threshold for the target Rydberg state. Much like the previous Rydberg tagging experiment (see Sec. 4.3), resulting ions are projected onto a microchannel plate detector and the signals are processed through a constant-fraction discriminator and their arrival-time distribution is recorded with a multi-channel analyzer on a computer. In the previous Rydberg tagging experiment, a delay between Rydberg excitation and ionization was introduced in order to map out the velocity of the Rydberg atoms using the width of the TOF distributions. In the present experiment a delay between excitation and ionization is also

introduced, but here we are interested in counting the number of Rydberg atoms detected in the TOF distribution and not its shape. The number of Rydberg atoms detected as a function of the delay time maps out how the Rydberg atoms decay in time and is a measurement of the lifetime.

An ideal measurement of the Rydberg atom lifetime inside of the MOT would proceed as indicated in Fig. 5.2. After excitation of the Rydberg atoms, the atoms are ionized by the electric field some time, Δt, later and detected. The total number of counts per second hitting the detector is proportional to the number of Rydberg atoms left Δt seconds after excitation. The lifetime is then mapped out by measuring the number of ions per second as a function of the delay time, Δt.

This ideal experiment is complicated by a number of issues. While the intention is always to carry out the experiment in exactly the same way every time, imperfections exist in the experiment which make this impossible. First, the number and density of the atoms in the excitation volume is nearly constant, but always fluctuating around some average. The intensities of the Rydberg excitation lasers also slightly fluctuate around some average. A more serious experimental issue (in the context of measuring lifetimes) lies in the switching of the green excitation laser. The laser is passed through an AOM to control the timing of the light pulses. The main issue here is that the AOM never turns the laser completely off and a small amount of light constantly leaks through the AOM. If this effect is not accounted for in some way, the lifetime data become

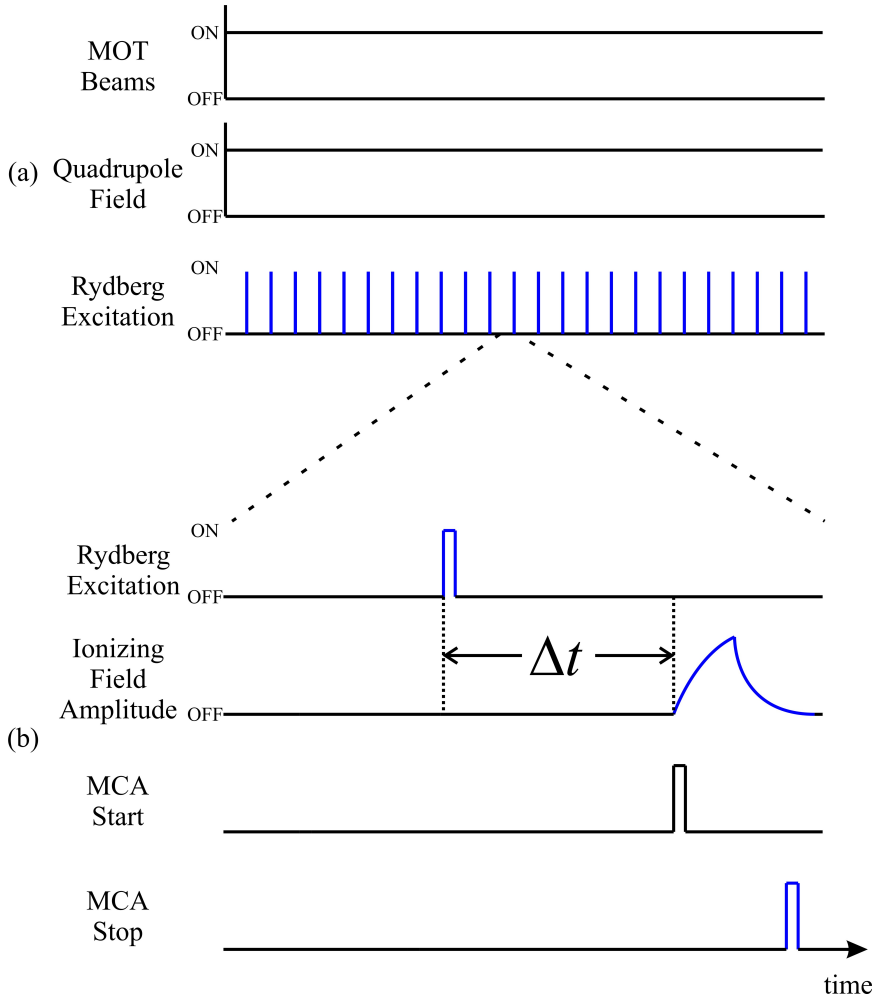

Figure 5.2: (a) Ideal Rydberg atom lifetime measurement inside the MOT. (b) Magnified view of Rydberg atom excitation and subsequent detection. An electric field ramp is used to ionize the Rydberg atoms after Δt seconds from excitation.

polluted with Rydberg atoms that were unintentionally created at unknown times.

These effects are compensated for by using an additional excitation and ionization pulse immediately preceding the excitation pulse used for lifetime

analysis, see Fig. 5.3. The additional excitation produces an additional TOF

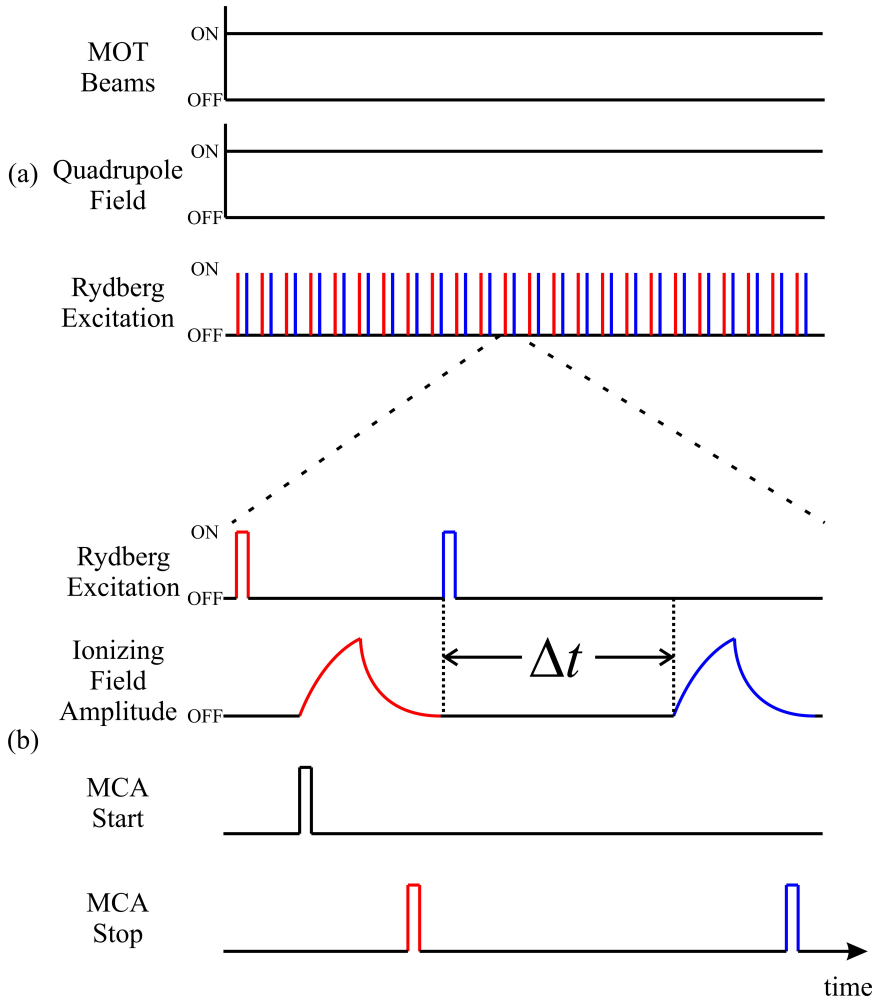

Figure 5.3: (a) Modified Rydberg atom lifetime experiment in the MOT. (b) Magnified view of the excitation and detection, which is valid in both lifetime experiments. Distributions from the red pulses are used to normalize the distributions acquired from the blue pulses (see text).

distribution which contains information about the instantaneous trap density and excitation intensities. The number of counts appearing in this additional

TOF distribution is used to normalize the number of counts appearing in the (original) TOF distribution of interest. Furthermore, this "normalizing" pulse clears out all of the Rydberg atoms which could have been created by leakage light since the previous ionizing electric field ramp. The amount of time for leakage light to have an effect is then limited by Δt and not the repetition rate of the experiment.

To measure the Rydberg atom lifetime inside the MOT, the timing sequence above was used at a repetition rate of 500 Hz. The time between the normalizing pulse and the subsequent green laser pulse is held constant. The excitation pulses are 1 μs wide. The green laser is held on resonance with the $nD_{5/2}$ Rydberg state and TOF distributions are acquired for 100 s at various values of the delay, Δt. Two TOF distributions result; an earlier one corresponding to the normalizing pulse and a later one that corresponds to the distribution used for lifetime analysis. The with of each of the distributions is ~ 30 μs. The total number of ions falling in a narrow window (1 μs $-$ 5 μs) centered on the later TOF peak is divided by the total number of counts appearing in the earlier normalizing distribution. The resulting value represents the normalized number of Rydberg atoms detected per second. Three of these measurements are performed at each value of Δt. The resulting data for the $50D_{5/2}$ Rydberg state are shown in Fig. 5.4. The error bars are the standard deviation of the measurements at each value of Δt. The data are fit to a decaying exponential function, $Ae^{-\Delta t/\tau}$, shown in blue. The amplitude of the decay is A, Δt is the delay time between excitation

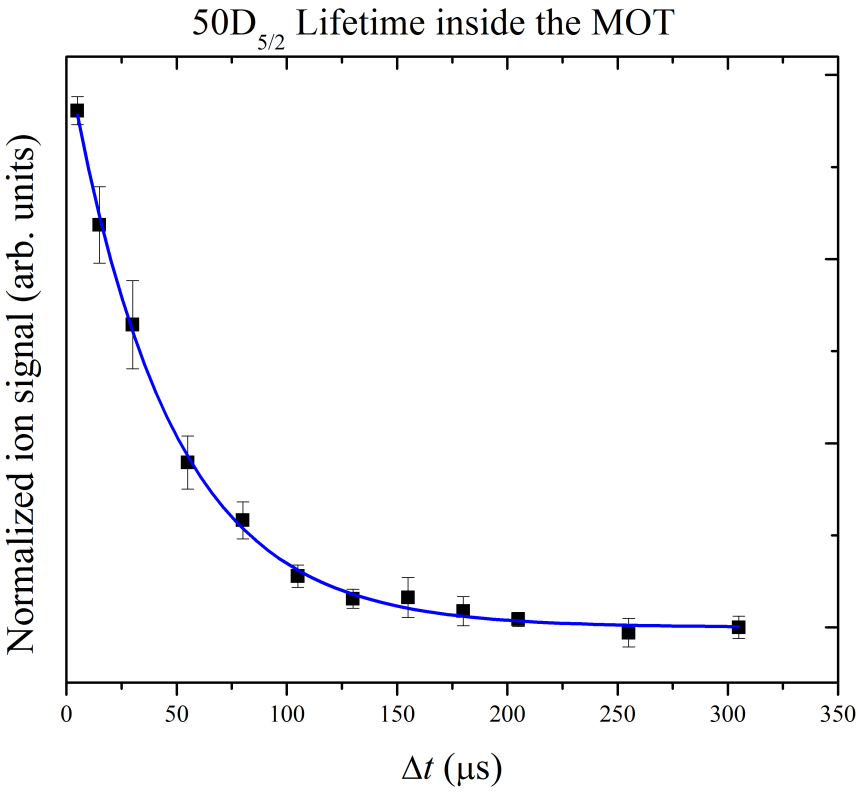

Figure 5.4: Experimental lifetime data for the $50D_{5/2}$ Rydberg state in the MOT. The solid blue line is an exponentially decaying fit function which yields $\tau_{MOT} = 46\ \mu\text{s} \pm 3\ \mu\text{s}$.

and ionization, and τ is the $1/e$ lifetime of the Rydberg state. The amplitude and the Rydberg lifetime are the only free parameters. The result from the fit is a Rydberg atom lifetime in the MOT of $\tau_{MOT} = 46\ \mu\text{s} \pm 3\ \mu\text{s}$. Theoretical calculation of the $50D_{5/2}$ lifetime predicts a value of $\sim 47\ \mu\text{s}$ [50].

The lifetime measurement in the MOT serves as a control measurement for the FORT experiment. The MOT lifetime determines the sum of the radiative and blackbody decay rates, as indicated by Eq. 5.1, which remain constant in the

corresponding FORT experiment. Repeating the experiment in the FORT then determines the depopulation due to photoionization, which can be compared against theory. In order to conduct a similar experiment in the FORT, the experimental timing shown in Fig. 5.3 had to be modified. The modified experimental timing sequence is shown in Fig. 5.5. After the FORT is loaded,

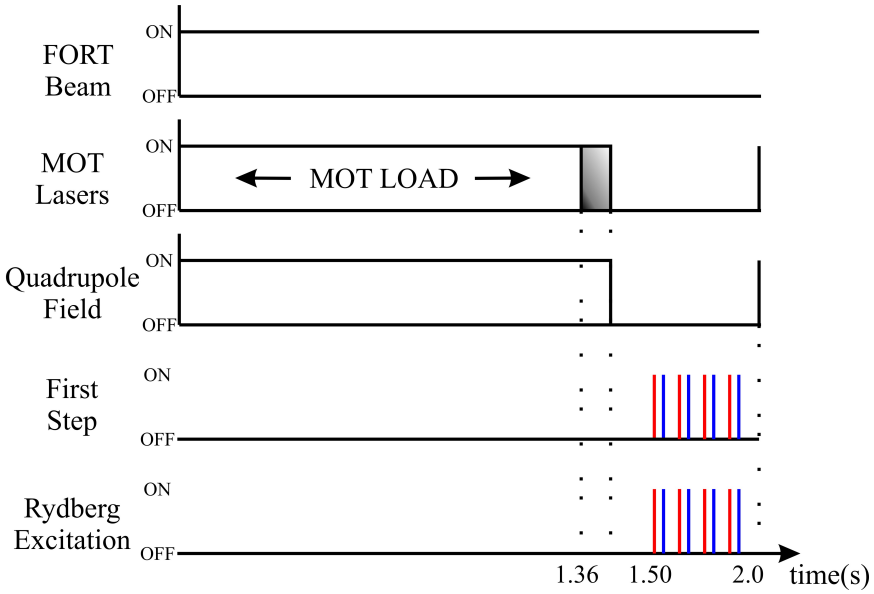

Figure 5.5: Timing for FORT loading and Rydberg atom excitation. Subsequent ionization and detection is identical to the MOT experiment.

the untrapped MOT atoms are allowed to fall away for 100 ms. After that time, the excitation and ionization pulses begin. Excitation and ionization are identical to the MOT experiment, Fig 5.3. As mentioned earlier, this experiment requires an extra laser that is nearly resonant with the repumping transition to excite Rydberg states, see Fig. 5.1. The IR laser is tuned to compensate for the

local blue ac Stark shift of the D2 transition. The IR laser is sent through an AOM for switching and coupled into a single-mode polarization-preserving fiber. The output is copropagated with the green excitation light and focused onto the FORT with a size of 86 μm $\pm$ 0.8 μm. The Rydberg excitation lasers intersect the FORT at an angle of $\sim 112.5°$. The normalized data for the $50D_{5/2}$ Rydberg atom lifetime measurement in the FORT are shown in Fig. 5.6. Rydberg atom

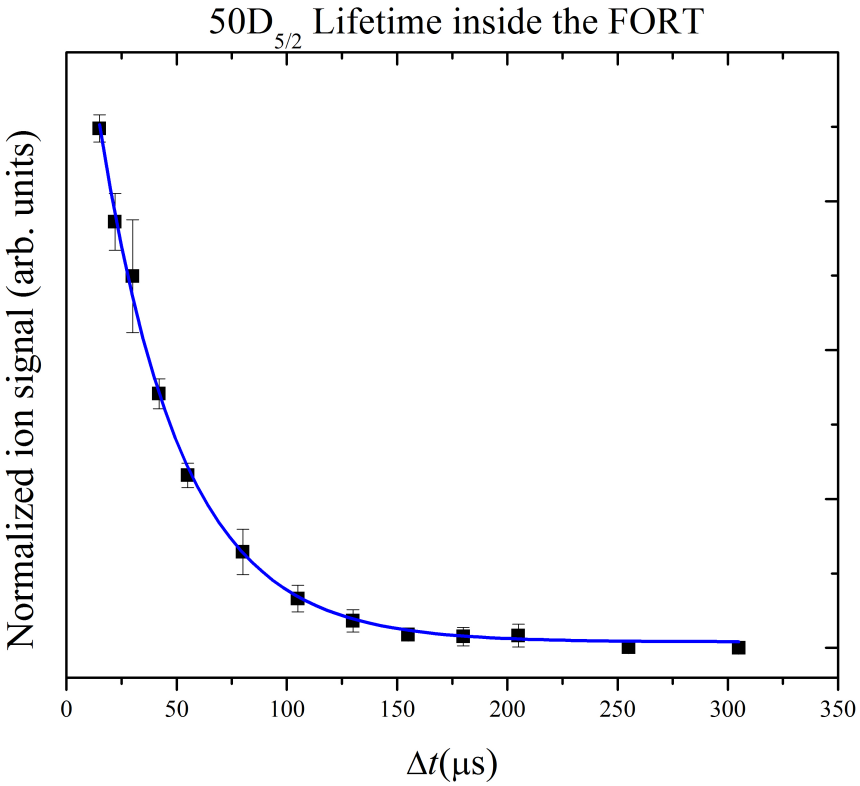

Figure 5.6: Experimental lifetime data for the $50D_{5/2}$ Rydberg state in the FORT. The solid blue line is an exponentially decaying fit function which yields $\tau_{FORT} = 37$ μs $\pm$ 3 μs.

lifetime analysis is carried out in the same way for the MOT experiment and the

FORT experiment. The fit to the data gives the shortened lifetime of $\tau_{FORT} = 37$ μs $\pm$ 3 μs, which is in theoretical agreement with predictions from [60]. Rydberg atom lifetimes are measured inside the MOT and inside the FORT for 11 different values of n in the range $50 \leq n \leq 75$. The lifetimes are used to extract the depopulation rates. The lifetimes and depopulation rates are compared to theory in the next Section.

5.4 Discussion of Results

There is a subtle issue involved in this experiment. The $nD_{5/2}$ Rydberg states addressed in this experiment are low-field seekers. This means that the trapping potential experienced by the ground state atoms becomes a repulsive potential once the Rydberg atom is excited. To estimate the magnitude of the repulsive effect, we assume the polarizability of the Rydberg states correspond to the polarizability of the free electron [60], $-e^2/m\omega^2$, where ω is the angular frequency of the FORT beam. This assumption overestimates the repulsive effect by $\lesssim 5\%$. Using this estimate, the nD states would be expelled from the FORT in ~ 1 ms if they traveled directly along the radial dimension of the FORT. This has the largest effect for the $75D_{5/2}$ state, which has both the largest polarizability and the longest lifetime. Because the atoms must accelerate along the gradient of intensity out of the trapping volume, the force of Rydberg atoms in the center of the FORT is initially very small. The repulsive force moves the Rydberg atoms

< 1 μm in 500 μs. A cesium Rydberg atom at ~ 40 μK moves ~ 25 μm in 500 μs. Thus, for times $\lesssim 1$ ms, the Rydberg atom motion is dominated by the initial temperature.

Lifetimes were measured for 11 $nD_{5/2}$ Rydberg states inside of the MOT and compared with identical measurements and inside the FORT. The experimental lifetimes are compared to the theoretical lifetimes in Fig. 5.7. The theoretical error bars include the quoted $\pm 5\%$ accuracy [50]. The experimental error bars come from a convolution of the lifetime error from the fit and the 1 μs excitation time. Agreement between experiment and theory is excellent.

The depopulation rates may be obtained with the lifetimes and Eq. 5.6. The theoretical and experimental depopulation rates are shown in Fig. 5.8. The sum of the radiative and blackbody decay rates is determined from the lifetime measurement in the MOT and Eq. 5.1. The total decay rate in the MOT is subtracted from the total decay rate in the FORT to yield the measured photoionization rate, γ_{PI}. The error in the photoionization rate is generated from an estimated uncertainty in the trapping beam intensity of 14 kW cm^{-2}. The uncertainty corresponds to the measured uncertainty in the waist radius of 43 μm $\pm$ 0.6 μm, and an estimated power at the trap location of 7.5 W $\pm$ 0.2 W. Again, there is very good agreement between experiment and theoretical predictions.

Equation 5.5 indicates that the photoionization rate is linear in the trapping laser intensity. To verify this, the photoionization rate of the $50D_{5/2}$ state was

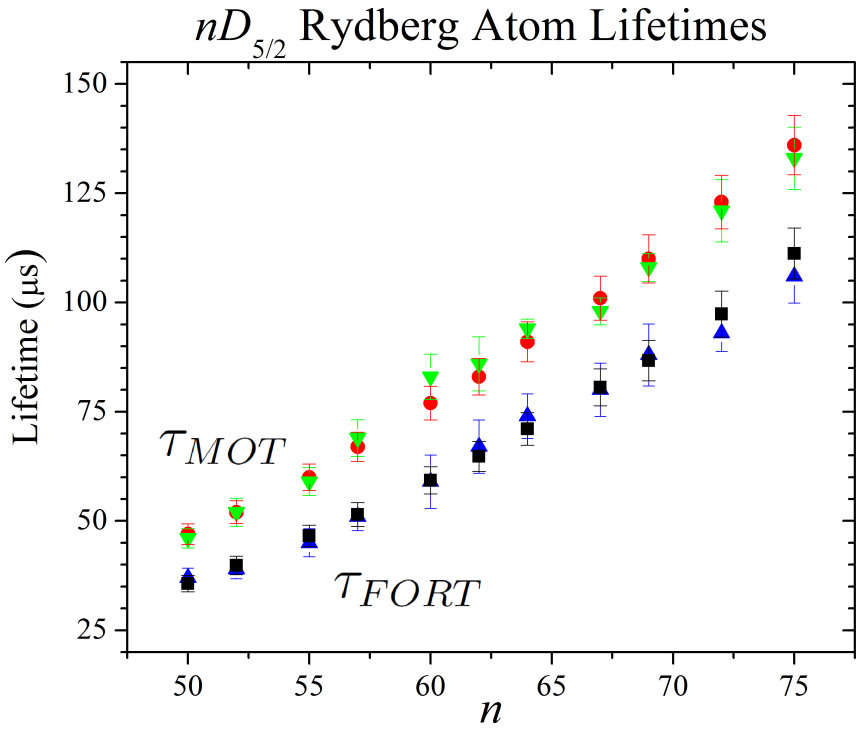

Figure 5.7: Experimental and theoretical Rydberg atom lifetimes as a function of principal quantum number. Green inverted triangles are the experimental lifetimes in the MOT. Red circles are the theoretical lifetimes in the MOT. Blue triangles are the experimental lifetimes in the FORT. The black squares are the theoretical lifetimes in the FORT for 258 kW cm^{-2} of FORT light.

measured as a function of the FORT laser power. The electric field amplitude of the ionizing pulse is lowered far below the ionizing threshold of the Rydberg state, so ions are only produced through photoionization due to the FORT beam and counted. The data are shown in Fig. 5.9. The data shown are the average of three measurements and the error bars represent the standard deviation. The

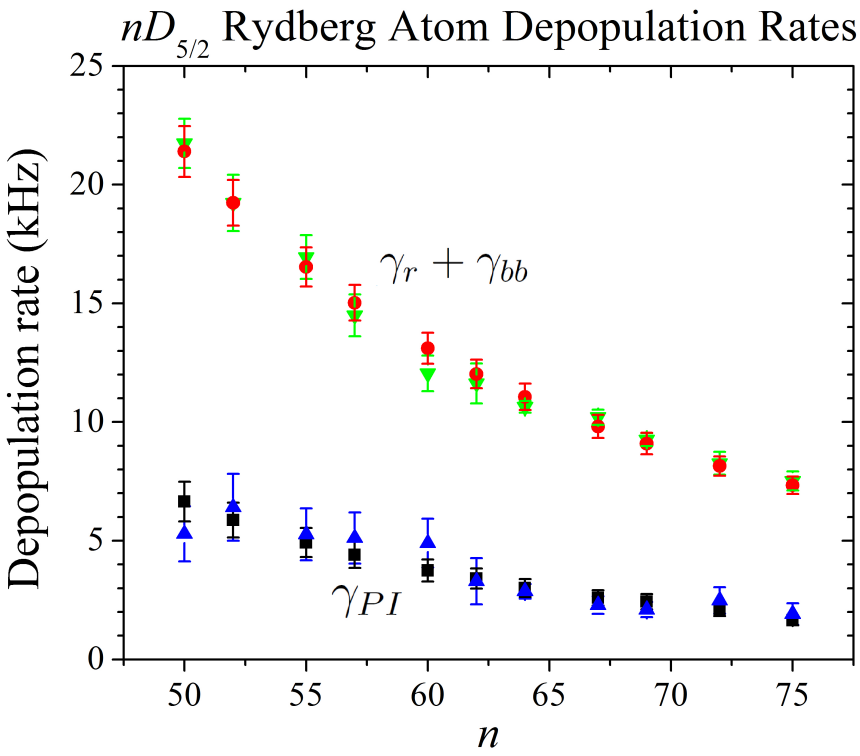

Figure 5.8: Experimental and theoretical depopulation rates as a function of principal quantum number. Green inverted triangles are the experimental sum of the radiative and blackbody decay rates in the MOT. The red circles are the theoretical depopulation rates. Blue triangles are the experimental photoionization rates. The black squares are the theoretical photoionization rate for 258 kW cm^{-2} of FORT light. The error bars include a 14 kW cm^{-2} uncertainty in intensity at the trap location.

data were fit to a line. The intercept of the fit corresponds to the observed background ion count rate of 8 Hz $\pm$ 1 Hz. The data were also fit to a quadratic function, but the value of the quadratic term from the fit is zero within the

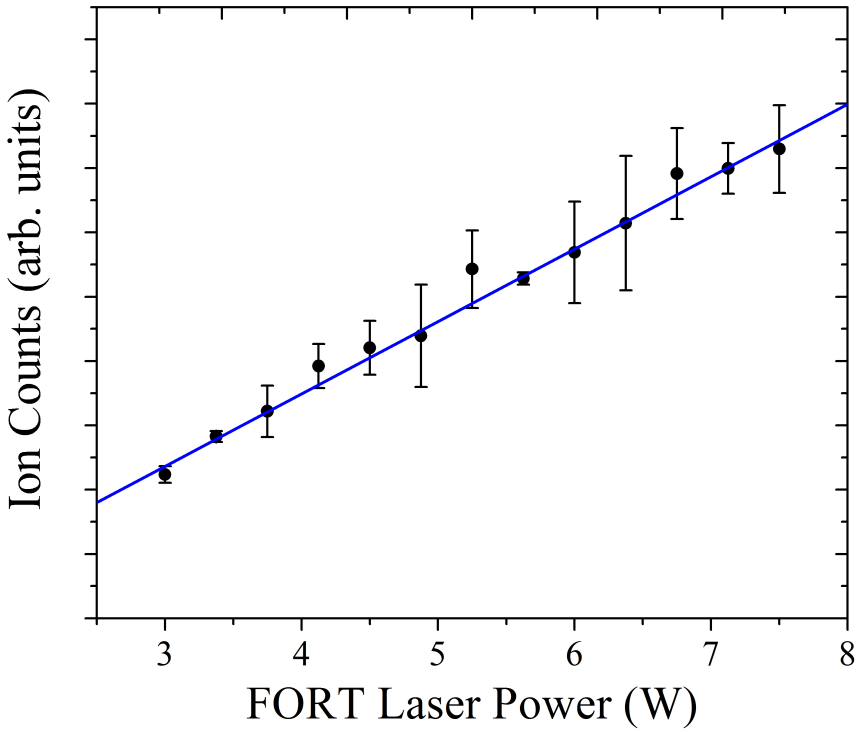

Figure 5.9: Photoionized $50D_{5/2}$ Rydberg atom counts as a function of FORT laser power. The error bars represent the standard deviation from three measurements. The solid blue line is a linear fit to the data. The intercept corresponds to the experimentally observed number of background ion counts within the error from the fit.

fitting error, indicating the data are best described by a line. This leads to the conclusion that ionization of the Rydberg state occurs through the absorption of a single 1064 nm photon.

The experimental lifetimes in the MOT experiments agree very well with the theoretical predictions from [50], which suggests the experiments are also in agreement with the earlier experimental work in rubidium [9, 10, 57, 11],

and the lower-lying states of cesium [58]. The consistency with theoretical predictions and experimental work of other groups provides confidence that the depopulation rates measured in the MOT experiments can be used to determine photoionization rates in the FORT experiments. The experimental photoionization rates also agree well with our calculations following [60]. Over most of the range of validity of the model by Beterov *et al.* [50], our experimental results show that photoionization rates from a FORT can be generated from principles following references [60, 62].

Chapter 6

Trilobite Molecules

6.1 Introduction

When Rydberg atoms are the constituents of molecular systems, interesting and exotic molecules can result. The interest in these types of molecules stems mostly from the fact that the Rydberg atoms provide these molecules with very high sensitivity to external perturbations. One class of these exotic molecules, "macrodimers", are homonuclear diatomic molecules that contain two Rydberg atoms [63, 16]. These exotic molecules are very fragile, with binding energies in the tens of MHz, and have extremely long bond lengths, 3 μm - 9 μm. Calculations including the dominant multipole-multipole interactions between pairs of Rydberg atoms revealed that wells can appear in the potential energy curves at very large distances [13] and that these wells can support many bound states [15]. The calculations suggested that the molecular bond could be stabilized by an electric field and macrodimers were finally experimentally observed in the presence of a background electric field in 2009 [16].

A second class of exotic diatomic molecule has recently been observed which contains one Rydberg atom and one ground state atom [22]. These so-called trilobite molecules (nomenclature soon to become clear) have a unique binding mechanism that relies on the scattering of the Rydberg atom electron off of the

ground state atom. The fascination with these trilobite molecules originates in the prediction that they can posses massive permanent dipole moments, ~ 1 kD (1 Debye $\sim 3.34 \times 10^{-30}$ C·m), which makes them amenable to electric field manipulation [24]. The molecules observed in Ref.[22] were bound by this scattering mechanism, but the $^3\Sigma(5S + nS)$ molecules were only expected to have an induced dipole moment [22]. It was later demonstrated theoretically and experimentally that the molecules possessed an observable permanent dipole moment of ~ 1 D [23].

The main result of this thesis is the observation of trilobite molecules in cesium with permanent electric dipole moments of $\sim 20-100$ D. The observations are compared to theoretical results. The theoretical principles dictating the binding mechanisms are sufficiently simple to describe here, however, due to the interaction of many different potential energy curves, full multichannel calculations had to be carried out for an accurate description of the molecules. These theoretical calculations were carried out by our collaborators at the Institute of Theoretical Atomic, Molecular and Optical Physics (ITAMP) at Harvard University, the details of which will not be described in this thesis. With the theoretical description that follows, the salient features of the theoretical calculation may be ascertained.

6.2 Theoretical Description

The size of the Rydberg atom is much greater than the size of the ground state atom in the molecule. Accordingly, the interaction of the Rydberg atom and the ground state atom is dominated by the interaction of the ground state atom with the highly excited Rydberg electron. The electron-ground state atom interaction is short range and highly localized in space. Since the spatial extent of the Rydberg atom electron wavefunction is very large, the perturbation to the wavefunction due to the presence of the ground state atom is weak. Furthermore, the Rydberg atom electron has very low kinetic energy so the interaction may be written in terms of a Fermi pseudopotential interaction of a low energy electron with the ground state atom [18, 19]. In atomic units, the interaction potential is written

$$V_{ea}(\mathbf{r},\mathbf{R}) = 2\pi A_s(k)\delta(\mathbf{r}-\mathbf{R}) + 6\pi A_p(k)^3\delta(\mathbf{r}-\mathbf{R})\overleftarrow{\nabla}\cdot\overrightarrow{\nabla}, \tag{6.1}$$

where the s and p-wave (momentum dependent) scattering lengths are $A_s(k)$ and $A_p(k)$, respectively. The nl Rydberg atom electron is a distance $\mathbf{r}$ from the remaining core and the ground state atom is a distance $\mathbf{R}$ away, see Fig. 6.1. The interaction potential is then attractive for negative electron-ground state atom scattering lengths. The momentum of the electron, k, is $\mathbf{R}$ dependent through a semiclassical analysis of the energy given below.

$$\frac{k(R)^2}{2} = -\frac{1}{2n^2} + \frac{1}{R} \tag{6.2}$$

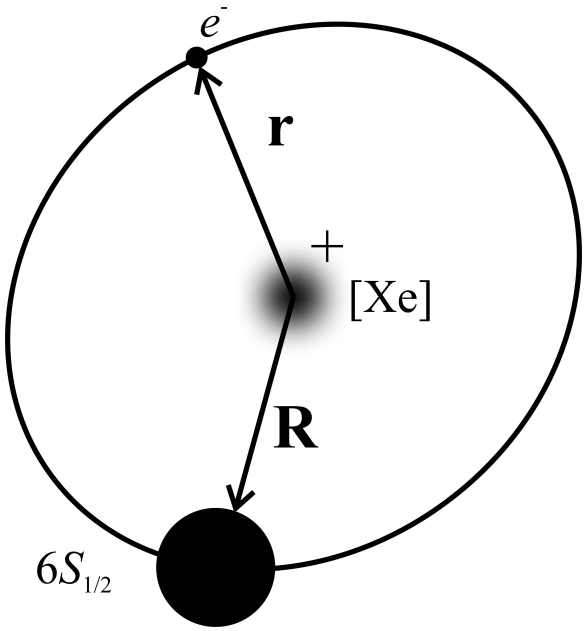

Figure 6.1: Coordinate system used for the pseudopotential. The Rydberg atom electron is at a distance **r** and the ground state atom is at a distance **R** away from the Rydberg atom core.

The kinetic energy of the Rydberg atom electron is simply equal to the binding energy of the nl-Rydberg state and the Coulomb potential at the position of the ground state atom.

The energy dependent s-wave scattering length, $A_s(k)$, is calculated from the scattering phase shift found in [64] and the electron momentum is determined from Eq. 6.2. The cube of the p-wave scattering length, A_p, is related to the p-wave scattering phase shift, η_p, by $A_p(k)^3 = -\tan\eta_p/k^3$. The p-wave scattering length splits into three pieces ($J = 0, 1$ and 2). To account for this, the p-wave

scattering length is taken to be

$$A_p^3 = \sum_{J=0}^{2} \left[c_{10,1M_J}^{JM_J}\right]^2 \; A_{p,J}^3, \tag{6.3}$$

where $c_{L_1M_1,L_2M_2}^{JM_J}$ is a Clebsch-Gordan coefficient and $M_J = \pm 1, 0$ is the projection of the total electron angular momentum. The Clebsch-Gordan coefficient is describing the p-wave scattering between the electron and the ground sate atom so $L_1, L_2 = 1$. The important consequence here is that the Clebsch-Gordan coefficients for the $M_J = \pm 1$ and the $M_J = 0$ cases are different, and therefore lead to slightly different potential energies. The empirical position of the $^3P_1$ resonance in e^-+ Cs($6s$) [25] is used with the splittings of the $^3P_0$ and $^3P_2$ states given in [65]. In order to obtain potential energy curves, a Hamiltonian containing the interaction, Eq. 6.1, is diagonalized with Rydberg atom basis states [23].

To qualitatively understand Eq. 6.1 more clearly, it should be noted that the excited nature of the Rydberg atom electron leaves it with very little kinetic energy. As such, the s-wave scattering of the electron is much more important due to the presence of the potential barrier for $l \neq 0$ partial waves. The first term in Eq. 6.1 describes the s-wave contribution to the potential. The delta function picks out the point in space where the ground state atom and the electron overlap. The question to ask then becomes where is the electron with respect to the Rydberg atom core? The probability of finding the electron is just given by the square of the Rydberg atom wavefunction $|\Psi_{nl}|^2$. The s-wave

portion of the interaction is just selecting the atomic states that maximize the wavefunction at the position of the ground state atom. The p-wave contribution acts to select the states which maximize the derivative of the wavefunction. Because the p-wave contribution is a small correction to Eq. 6.1, the resulting potential curves strongly mimic the oscillations present in the Rydberg atom wavefunction.

An example of the resulting potential energy curves for $n^* = 27$ is shown in Fig. 6.2. The potentials corresponding to $M_J = \pm 1$ are solid curves and the $M_J = 0$ projections are dashed curves. The oscillations seen in the potential energy mimic those of the parent $31S$ Rydberg state. The near-integer quantum defect of the nS cesium Rydberg states places several potential energy curves associated with the degenerate hydrogenic manifold energetically nearby. The proximity of these hydrogenic states produces non-adiabatic couplings between them and the parent nS state which provide potential wells supporting bound states. Because these bound states exist near $R = 1000$ atomic units (a.u.), they are considered ultralong-range molecular states.

The potentials shown in Fig. 6.2 show the asymptotic states to which the potentials correspond, but the wells of interest lie ~ 100 MHz to the blue of the $nS_{1/2}$ thresholds and are barely visible in Fig. 6.2. The potentials are reproduced on a finer scale with the lowest vibrational bound states in Fig. 6.3. The potential wells in blue correspond asymptotically to the $27G + 6S_{1/2}$ pair state, but due to the mixing with the $31S_{1/2}$ state it has $\sim 99\%$ s-character and

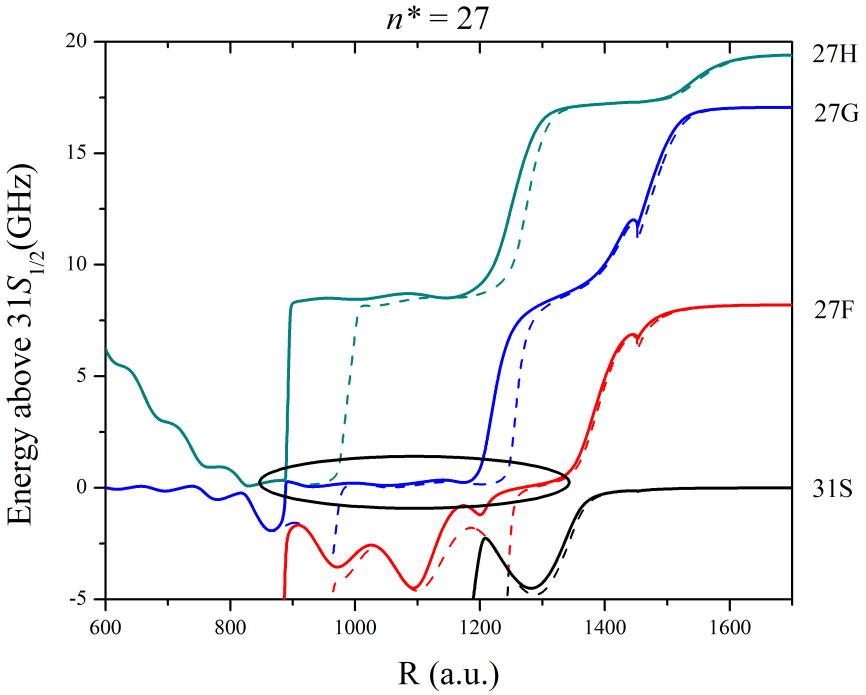

Figure 6.2: The Born-Oppenheimer potential energy curves for the states near $n = 31S$ ($n^* = 27$). Potentials for the $M_J = \pm 1$ projections are solid curves and the $M_J = 0$ potential curves are dashed. The appropriate asymptotically correlating states are labeled on the right. The circled region contains the potential wells of interest, ~ 150 MHz above the nS thresholds.

is accessible from the ground state via two-photon association. The $M_J = \pm 1$ potential energy curves are solid lines and the $M_J = 0$ potential energy curves are the dashed curves. The goal of the present experiment is to observe these ultralong-range, "trilobite", molecules.

The initial prediction of these molecules appeared in 2000 from Greene *et al.* [24]. The paper described that the interaction of the degenerate manifold

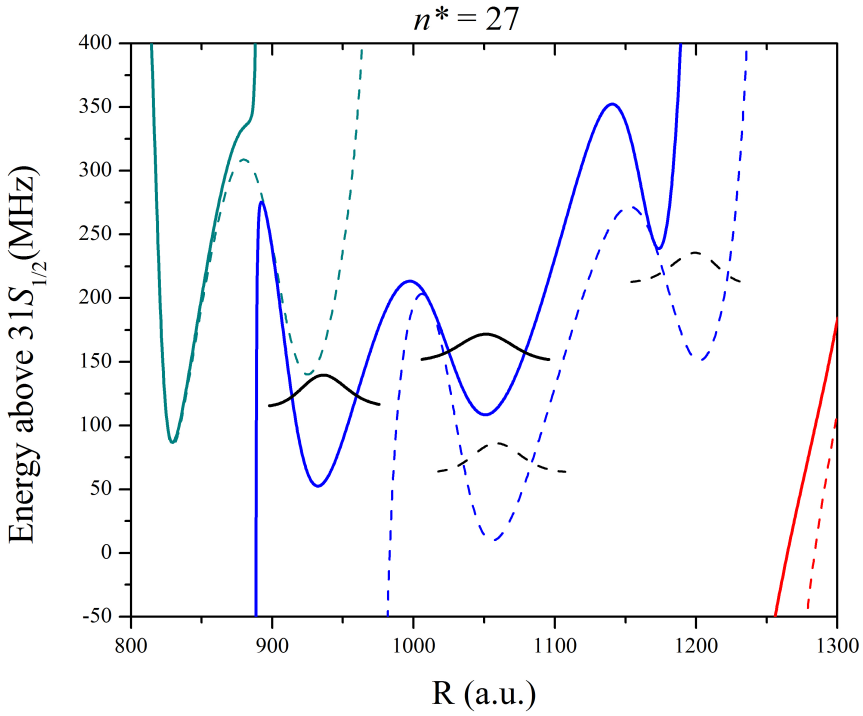

Figure 6.3: Expanded view of the circled region in Fig. 6.2. The lowest supported bound states of the $27G + 6S_{1/2}$ pair potentials are shown. The $M_J = \pm 1$ projections are solid curves and the $M_J = 0$ projection is dashed.

of states causes the states to possess massive permanent dipole moments, D, with magnitude $D \simeq R - \frac{1}{2}n^2$ (a.u.), which are in the kDebye range. If the molecular state can be mostly characterized by s character, the magnitude of the dipole moment can drop by an order of magnitude or so, but the state becomes easily accessible through two-photon association from the ground state. This is case for the cesium ultralong-range molecules studied here. The accidental near degeneracy of the states caused by the near-integer quantum defect gives rise to

mixing of the states, distributing s character and degenerate character among them. This leads to hydrogenic character at the 1% level and gives rise to large permanent dipole moments and easy experimental accessibility. The following Section describes the experiment carried out to observe these ultralong-range, "trilobite", molecules.

6.3 Experiment

6.3.1 Experimental Method

For the ultralong-range states to be created, the Rydberg atom needs to be ~ 1000 a.u. from the ground state perturbing atom. This means the density needs to be sufficiently high that several pairs of atoms separated by this distance are available. The average density available inside of a magneto-optical trap (MOT) is $\sim 1 \times 10^{10}$ cm^{-3}, producing an average atomic separation of $\sim 1 \times 10^{5}$ a.u., which is orders of magnitude larger than the required distance. In the crossed far off-resonance trap (FORT), the number density is increased to $\sim 2 \times 10^{13}$ cm^{-3} and the average separation is decreased to ~ 7000 a.u., or 7 times the required photoassociation distance. This means high densities are needed to observe these molecular states. Furthermore, motion between the Rydberg atom core and the ground state atom is not desirable, so ultracold temperatures are also a requirement. Both of these conditions are satisfied in a crossed FORT, which is employed here. To identify the molecular states, an

absorption spectrum near the parent Rydberg state is acquired by monitoring the number of ions produced as a function of frequency of one of the two photons required for their photoassociation. The details of the crossed FORT preparation and timing sequence follow.

6.3.2 Experimental Details

In order to photoassociate the molecular states, a high density sample of ultracold cesium atoms are prepared in a crossed FORT. The crossing geometry for the two FORT beams was previously described in Section 3.5 and the loading sequence of the crossed FORT was described in Section 3.5.2, but are briefly reproduced here. The two FORT beams intersect at an angle of 22.5°, which create a trapping volume that is cigar shaped with a 2:1 aspect ratio, see Fig. 3.24.

To load the FORT, a sequence identical to Fig. 3.19 is used. Briefly, the MOT is loaded to maximum atom number for 1.36 s and then the laser parameters are changed to provide an additional cooling phase. After this 40 ms cooling phase the atoms are 40 μK and all of the trapping fields for the MOT are extinguished leaving atoms trapped inside of the crossed FORT. The maximum available number density in the crossed region is $\sim 2 \times 10^{13}$ cm^{-3}.

The molecular states are excited inside the crossed FORT using a two-photon process. The first step is an infrared (IR) photon tuned near the $6P_{3/2}$ hyperfine manifold. The second photon is a green photon near 512 nm. The geometry of the excitation beams with respect to the trapping beams is shown in Fig. 6.4.

The IR beam is generated from an external cavity diode laser. The beam is

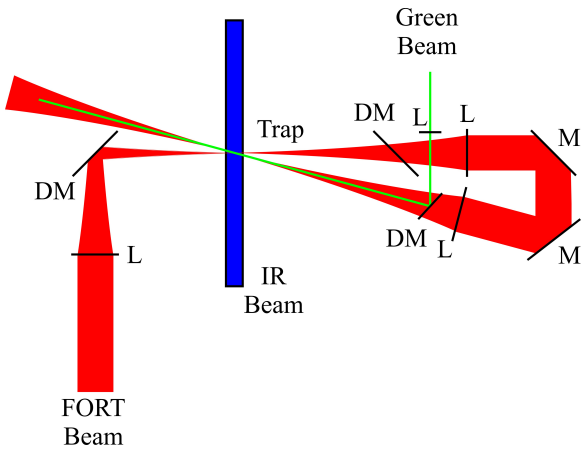

Figure 6.4: Geometry used for excitation of molecular states. The green laser beam is combined with the recycled FORT beam with a dichroic mirror (DM) and focused onto the crossed FORT with a lens (L). The IR beam is collimated and illuminates the entire trap.

sent through an acousto-optic modulator (AOM) and a single-mode polarization-preserving fiber. The output is collimated to a size of 1 mm^2 and intersects the crossed FORT at an angle of 79° with respect to the long axis of the cross. During excitation, the IR beam has 5 mW of power. The green beam is generated from a Coherent 699-21 ring dye laser. This beam is also sent through an AOM and single-mode polarization-preserving fiber. The output is copropagated with the second FORT beam and is focused to a spot size of 44 μm. The power used for excitation is 70 mW.

To locate the positions of the molecular states, the green laser is scanned on the blue side of the nS Rydberg states while the IR laser remains locked 182

MHz below the cesium $6S_{1/2}(F = 3) \rightarrow 6P_{3/2}(F = 2)$ transition, see Fig. 6.5. The two-photon linewidth of the excitation pulses was measured inside of the

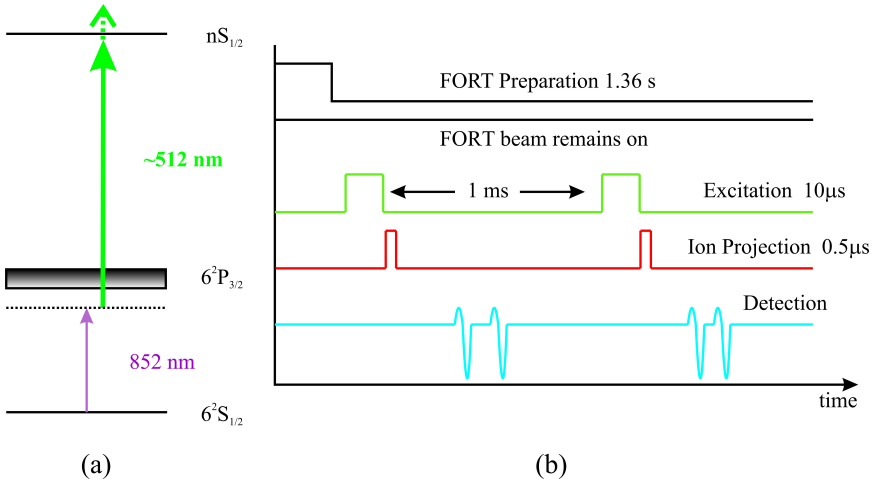

Figure 6.5: (a) Two-photon excitation scheme used for photoassociation of the molecular states. The IR laser frequency is locked and the green laser frequency is scanned to acquire an absorption spectrum. (b) Experimental timing used to acquire the absorption spectrum. Detected ions are counted as a function of green laser frequency.

MOT to be < 3 MHz. Because the molecular states contain Rydberg atoms, the FORT beam can be used to photoionize the Rydberg atom, as described in detail in Chapter 5. An absorption spectrum is acquired by monitoring the number of ions produced as a function of green laser frequency. The excitation pulses begin 20 ms after the crossed FORT has been loaded to let the uncaptured MOT atoms fall away. Each excitation pulse is 10 μs long and is immediately followed by an electric field pulse to project any positive ions onto a microchannel plate detector where they are counted. The excitation step repeats at 1.0 kHz and lasts 500

ms, at which time the green laser frequency is incremented by 1 MHz and the crossed FORT is reloaded. The electric field used to extract the ions, 67 V cm^{-1}, is far below the ionization threshold of any Rydberg states in the experiment [1]. Ion signals corresponding to the Cs_2^+ molecular time-of-flight are simultaneously acquired with the Cs^+ signal. As many as six absorption spectra are averaged together to obtain a single experimental spectrum. Precise knowledge of the absolute frequencies of both excitation lasers is required to correctly describe the energies of the observed molecular transitions. The experimental methods employed to calibrate the laser frequencies appear in the following Section.

6.3.3 Frequency Calibration

Using atomic transitions, the frequencies of both excitation lasers can be calibrated. The IR laser frequency is calibrated with a saturated absorption spectrometer. In the saturated absorption setup, two counterpropagating laser beams (derived from a single beam) are passed through a cesium vapor cell. Their intensities are made very different. The strong beam is used to saturate an atomic transition, while the weak beam is detected on a photodiode. Without the presence of the saturating beam, scanning the weak beam across the D2 transition produces a broad absorption feature due to the room-temperature atoms having Doppler shifts larger than the total hyperfine splitting of the entire D2 manifold, see Fig. 6.6. Atoms moving perpendicular to the laser beam experience no Doppler shift. This means if the strong counterpropagating beam

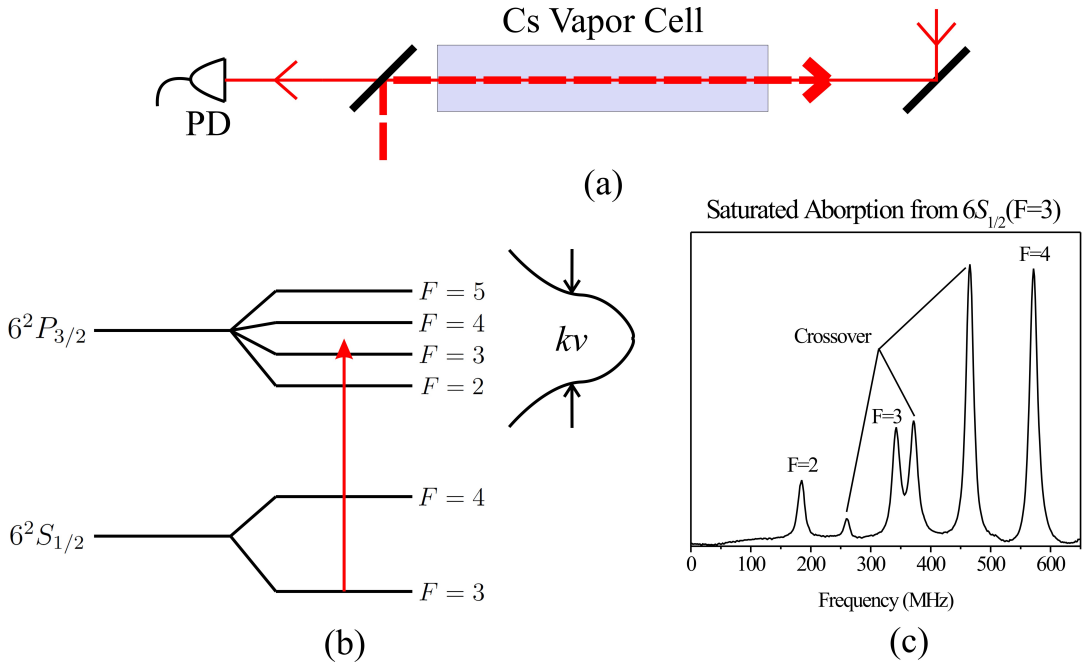

Figure 6.6: (a) Saturated absorption setup used for IR laser frequency monitoring. (b) Hyperfine structure of the cesium D2 transition. The IR laser probes the individual hyperfine levels which have Doppler broadening, kv, that is larger than the $6P_{3/2}$ hyperfine manifold. (c) Resulting saturated absorption spectrum when scanning the IR laser. During the experiment the IR laser frequency is shifted in the saturated absorption setup so that the $F = 3$ transition is on resonance.

is added, those atoms which have no Doppler shift will be resonant with both laser beams. Atoms with Doppler shifts will not be simultaneously resonant with both beams. When the atom is in resonance with both beams, the transition becomes saturated due to the strong beam and fewer atoms are available to absorb the weaker beam. This is detected as an increase in transmission of the

weak beam at the exact resonance position of the individual hyperfine state within the Doppler background. Transmission peaks appear in the Doppler background that map out the hyperfine structure of the manifold, the positions of which are accurately known. Furthermore, since there are multiple levels in the $6P_{3/2}$ manifold that connect to a common ground state, cross-over peaks appear in the spectrum. These peaks are due to Doppler shifted atoms energetically exactly between two hyperfine states. An experimental saturated absorption spectrum with the Doppler background subtracted is shown in Fig. 6.6 (c).

A fraction of the beam used for excitation of the molecular states is sent to the saturated absorption setup. The setup incorporates two AOMs that are used to shift the observed frequency of the peaks in the saturated absorption spectrum with respect to the lock point of the laser. The AOMs shift the light such that the Cs $6S_{1/2}(F = 3) \rightarrow 6P_{3/2}(F = 3)$ transition is on resonance during the experiment. The saturated absorption spectrum determines the IR frequency within ~ 3 MHz.

To monitor the frequency of the green laser, a fraction of the laser output is combined with light from the IR laser to generate an electromagnetically induced transparency (EIT) signal in a room-temperature vapor cell. For a detailed and comprehensive discussion of EIT, the reader is referred to the review by Fleischhauer *et al.* [66]. EIT is a quantum mechanical interference process that involves at least three atomic levels. In Rydberg atom EIT, the three levels involved are the ground state, $6S_{1/2}$, the first excited state, $6P_{3/2}$, and the

target $nS_{1/2}$ Rydberg state, see Fig. 6.7. A quantum mechanical interference can occur because there are multiple pathways present to arrive at the $6P_{3/2}$ state. This can be done two ways. This simplest way to arrive at the first excited state is through the absorption of a single IR photon. Another way to arrive in the same state is through the absorption of an IR photon, followed by subsequent absorption and stimulated emission of a green photon. If the Rabi frequency of the upper transition is made very high compared to that of the lower transition, the two processes have similar probabilities and can interfere with each other. When both of the lasers are in two-photon resonance with the Rydberg state, interference occurs. Absorption of the IR photon brings the atom to the $6P_{3/2}$ state. The two-photon process of absorption and emission of green photons can be thought of as a 2π pulse from the $6P_{3/2}$ state. Because the 2π pulse causes a π phase-shift in the wavefunction, the probability amplitudes cancel and destructive interference occurs. This causes the gaseous medium, which normally absorbs the IR light on resonance, to become transparent on resonance. The signal is detected as an increase in the amount of IR light falling on the photodiode and a peak appears. EIT resonances are expected for all of the accessible hyperfine states in the $6P_{3/2}$ manifold. The green light in the EIT setup is arranged in both co- and counterpropagating configurations with respect to the IR beam. This arrangement produces up to six EIT resonances corresponding to different hyperfine states whose absolute frequency relations are known. The positions of the EIT resonances can be shifted to any desired

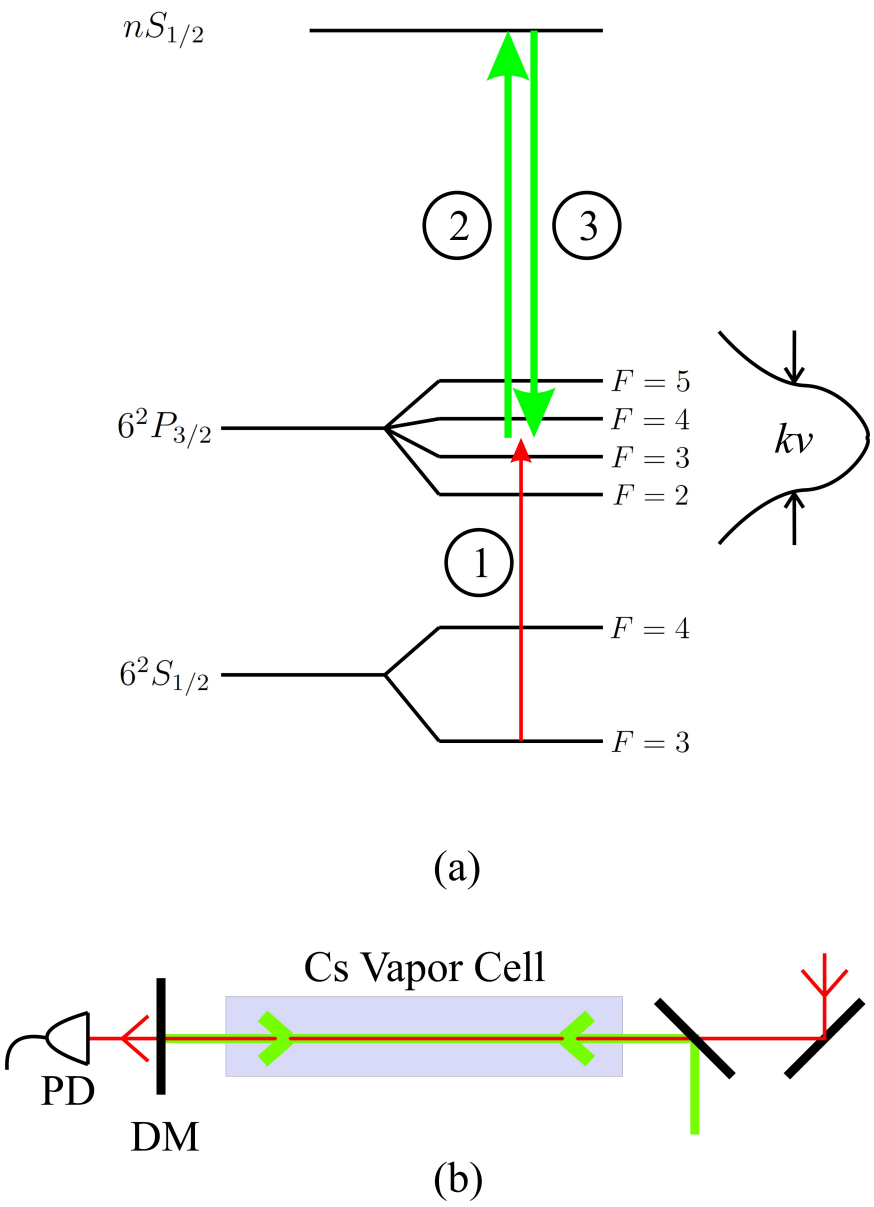

Figure 6.7: (a) Excitation scheme for generation of an electromagnetically induced transparency (EIT) signal. The signal is generated from a quantum mechanical interference process between the absorption of a single IR photon and a three photon process involving the indicated green photons. The Doppler width of the atoms in the vapor cell is indicated. (b) Optical arrangement for generation of EIT. The dichroic mirror (DM) produces co- and counterpropagating beams with respect to the detected IR beam.

location with AOMs to provide spectroscopic markers.

6.4 Results

During the experiment, the EIT spectrum is acquired simultaneously with the absorption spectrum as the green laser is scanned. Because the green laser is frequency stabilized with a Fabry-Pérot cavity, the frequency can unintentionally move with the temperature or pressure in the room. To counteract this effect, the observed separation of the EIT resonances is scaled so that the peaks have the correct spacing. Using the EIT resonances to scale the frequency step of the green laser, many spectra can be averaged together with a minimal amount of blurring due to frequency drift. An example of a single scaled experimental spectrum near $31S_{1/2}$ showing EIT resonances is shown in Fig. 6.8. The two EIT resonances shown in blue are due to the counterpropagating green beam. The red curve is a Lorentzian fit to the EIT spectrum. The large peak is due to the $6S_{1/2}(F = 3) \rightarrow 6P_{3/2}(F = 2)$ transition and the smaller peak is due to the $6S_{1/2}(F = 3) \rightarrow 6P_{3/2}(F = 3)$ transition. The observed splitting of the peaks is scaled so that the two peaks are separated by $\Delta_{hfs}(\lambda_{IR}/\lambda_g - 1)$ MHz, where Δ_{hfs} is the hyperfine splitting between the $F = 2$ and the $F = 3$ states and the λ's are the IR and green wavelengths. The hyperfine splitting of the $F = 2$ and $F = 3$ states is $\Delta_{hfs} = 151.2$ MHz [31], giving a predicted splitting of 100.4 MHz for these two EIT resonances. The Lorentzian fits provide

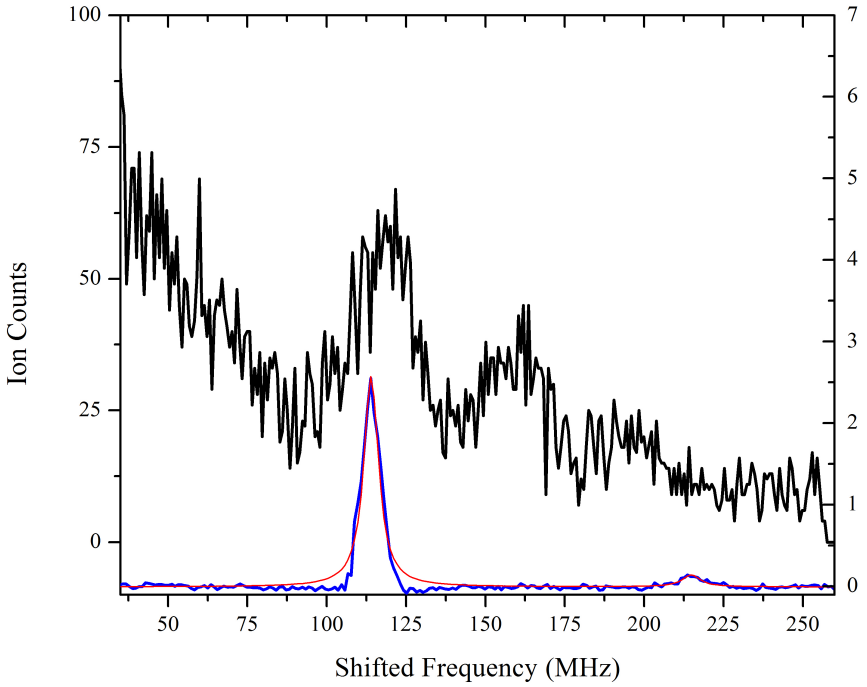

Figure 6.8: A single experimental spectrum near $31S_{1/2}$ is shown in black. The simultaneously acquired EIT spectrum is shown in blue. Lorentzian fits to the EIT peaks are shown in red. The line centers of the fits are used to scale the frequency axis to match the expected splitting of the EIT peaks.

the line centers so that their separation may be scaled to 100.4 MHz. The experimental absorption spectrum is shown in black with a scaled frequency axis. The peaks appearing in the spectrum are due to photoassociation of ultralong-range molecular states. The EIT resonances are shifted with AOMs so that the target molecular resonances lie between them. This allows for accurate location of the molecular resonances with respect to the EIT resonances.

In addition to knowing the separation of the EIT resonances, their location with respect to the bare Rydberg atom transition is also known. Because the experiment takes place inside of a FORT, the Rydberg atoms and ultralong-range molecules experience an ac Stark shift. Because the molecular states consist of a single Rydberg atom and the ac Stark shift of the Rydberg state is only weakly state dependent [1, 67], it is expected that the molecular states exhibit a similar shift and broadening to the bare atomic Rydberg transition. The ac Stark shift of the $31S_{1/2}$ state was measured by taking an absorption spectrum inside the MOT and comparing it to one in the FORT. The average ac Stark shift of the bare atomic transition was measured to be 19 MHz. The minimum linewidth in the FORT is ~ 11 MHz compared to < 3 inside the MOT.

Using the known positions of the EIT resonances and the average value of the ac Stark shift, the frequency axis can be aligned to the nearby $nS_{1/2}$ threshold. As many as six individual absorption spectra are averaged together in this way to produce one single experimental spectrum of the region. An example of an averaged spectrum near $31S_{1/2}$ is shown with the EIT spectrum

in Fig. 6.9. Scaling the frequency axis places the zero directly under the main

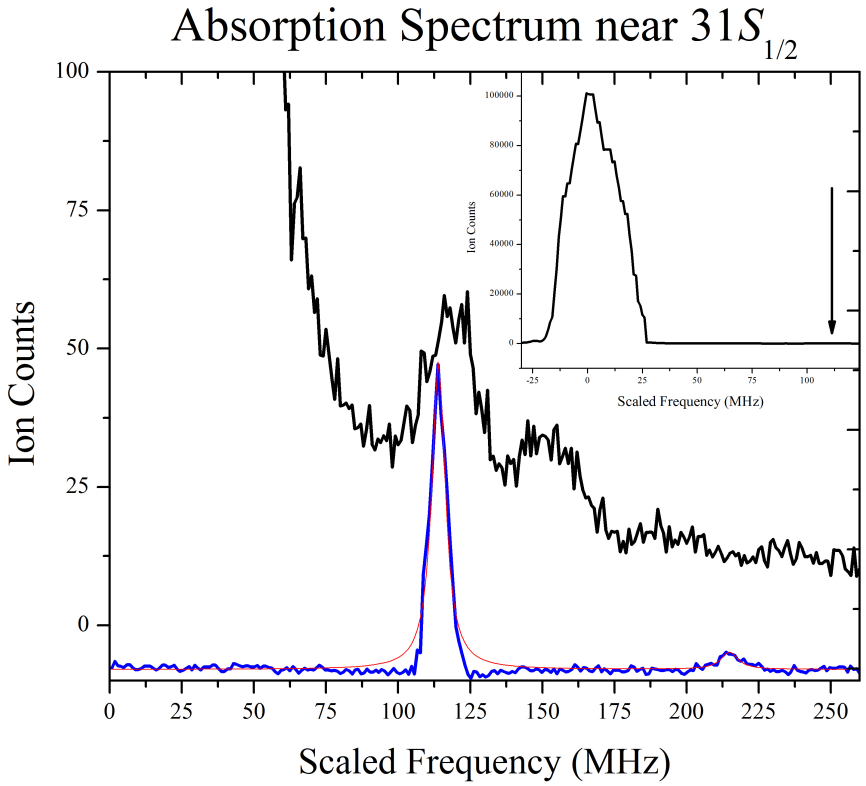

Figure 6.9: Averaged experimental data near $31S_{1/2}$. Clear peaks are seen in the absorption spectrum ~ 50 ion counts high. The inset shows a single spectrum of the same region, but plotted on a scale up to 120,000 ion counts to make the Rydberg atom peak visible. The arrow points to the molecular resonances.

Rydberg atom peak. Peaks appearing at higher energies are visible which are $\sim 10 - 60$ ion counts high. The peaks in the absorption spectrum are due to the photoassociation of ultralong-range molecular states. The height of these peaks are to be contrasted with the height of the main Rydberg atomic line of $> 100,000$ ion counts. The low signal yield for the molecular states is to be

expected due to the requirements of laser intensity and pairs of atoms ~ 50 nm apart. Ion signals corresponding to the molecular time-of-flight were not observed in contrast to the earlier Rb experiment [22].

Once the experimental data are processed, the zero of energy is aligned with ac Stark shifted atomic Rydberg transition. This compensates for the ac Stark shift of the states so that the spectrum may be compared to the theoretical calculations which do not take the FORT beam into account. The main result of this thesis is the comparison between theoretical predictions and experimentally observed locations of the ultralong-range molecular states. Regions with principal quantum numbers $31 \leq n \leq 34$ are compared in Fig. 6.10. The theoretical calculations are shown in Figs. 6.10 (a-d) and the experimental spectra are shown in Fig. 6.10 (e-h). The potential energies corresponding to the $M_J = \pm 1$ potential are solid curves and the $M_J = 0$ are dashed curves. The vibrational wavefunctions are plotted with the appropriate excitation energies shown as lines under the experimental spectrum.

The interactions leading to the observed trilobite states are complex. The potential wells supporting the states are formed by avoided-crossings of nearly degenerate states and appear above the nS thresholds. The potential energy in this region is also sensitive to the empirically entered value of the $^3P_1$ resonance [25]. Furthermore, the experiment takes place inside of a very intense trapping field, which the calculation does not account for. Despite the complexity of the interactions involved, agreement between the theoretical predictions and

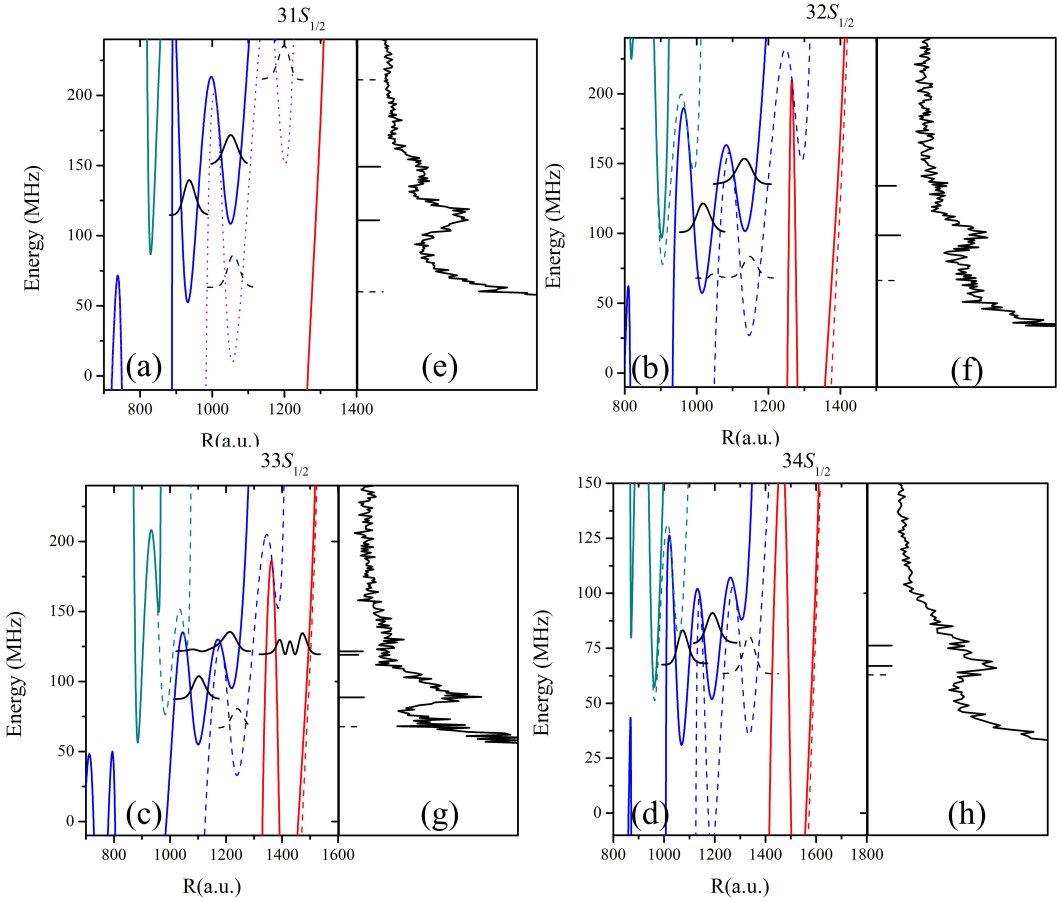

Figure 6.10: Comparison of the theoretical predictions (a-d) and the experimental spectra (e-h). Panels show the potential curves supporting the ultralong-range molecular states and the wavefunctions of the vibrational states that are supported. The zero of energy is set to the value of the field-free $nS_{1/2}$ Rydberg state. The blue potentials asymptotically corresponds to the $(n-4)G+6S_{1/2}$ pair energy. The red potential curves asymptotically correspond to the $(n-4)H+6S_{1/2}$ pair energy. The frequency position of the vibrational states are indicated with lines under the experimental spectra.

experimental results is excellent for each value of n. The ability to predict the correct resonance positions of the molecular states supports the hypothesis that the molecular states experience the same ac Stark shift as the Rydberg atom. The behavior of the potentials near the nS thresholds is also sensitive to the position of the $^3P_1$ e^-+ Cs resonance. As such, the agreement between theory and experiment reported is an indirect confirmation of the accuracy of the resonance position [25].

The observed molecular states are predicted to have giant permanent dipole moments. This is a very peculiar characteristic for a homonuclear diatomic molecule. In a traditional homonuclear diatomic molecule, the binding electron is shared equally among the two atoms. The molecular states here have a binding mechanism which is based on asymmetric electronic excitation between the atoms. The asymmetry in the electronic excitation gives rise to giant permanent dipole moments. To further illustrate this idea, the square of the full electronic wavefunction of the $^3\Sigma(6S + 27G)$ $M_J = \pm 1$ molecular state near $R = 1050$ a.u. is shown in Fig. 6.11. The probability distributions are plotted in cylindrical coordinates, (r, z), where the z-axis is the internuclear axis and r is the radial distance from the z-axis at the position of the Rydberg atom core. The Rydberg atom core sits at $(0, 0)$. The top plot shows the probability distribution from above and the bottom plot show the same distribution at an angle to highlight the structure in the distribution.

The majority of the electronic wavefunction mimics that of the parent $31S$

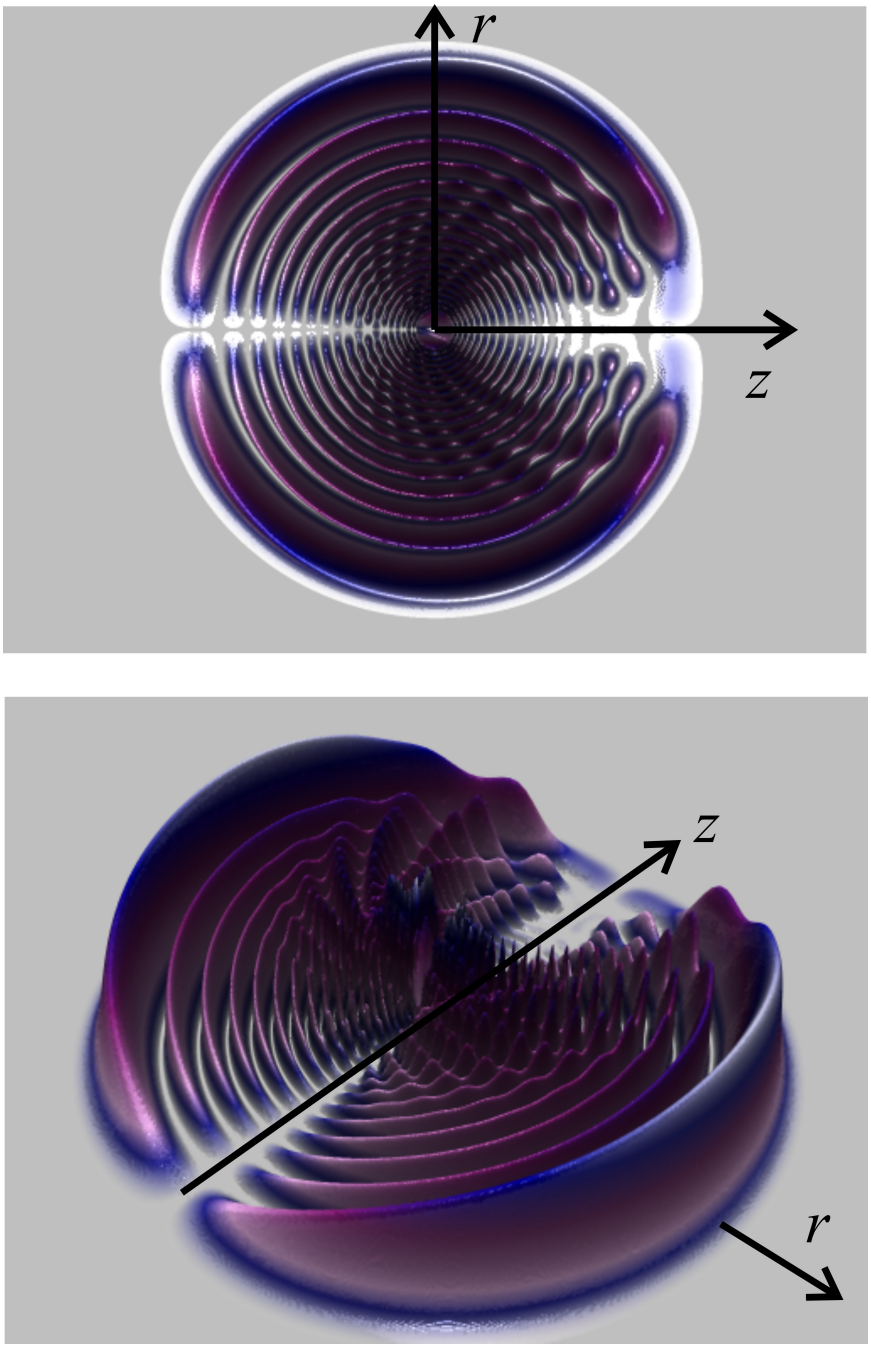

Figure 6.11: Full electronic probability distribution of the $^3\Sigma(6S + 27G)\, M_J = \pm 1$ molecular state near $R = 1050$ a.u. in cylindrical coordinates, (r, z). The lower plot shows the distribution from an angle.

wavefunction. It can be clearly seen that the normally symmetric probability distribution of the $31S$ state has been perturbed on one side. To highlight the effect of this perturbation, the wavefunction of the $31S$ Rydberg state has been subtracted from the full electronic wavefunction before computing the square. The resulting distribution is shown in Fig. 6.12. Removing the contribution from the symmetric $31S$ state reveals a highly localized structure in the electron probability distribution. The structure resembles ancient trilobite fossils and is the reason for the name given to these molecular states. The sphere at the center of the figure represents the Rydberg atom core. The ground state atom is positioned under the two regions of highest electron probability. The electron probability distribution is reproduced in Fig. 6.13 with lighting effects to illustrate the magnitude of the probability distribution in space. The asymmetry in the electron probability distribution is an indication that there is separation of charge and that these trilobite states possess giant dipole moments. Using the wavefunctions of the trilobite states, their dipole moments can be accurately calculated. This was demonstrated to reproduce the experimental dipole moments found in [23]. The dipole moments of two prominent $M_J = \pm 1$ states are 33.5 Debye and 37.4 Debye and generally, the molecular states will have higher dipole moments the further they are from the nS asymptote. The values of these dipole moments are to be compared with a more standard polar molecule, NaCl, with a dipole moment of 9 Debye and the previously observed Rb trilobite states with dipole moments of ~ 1 D [23].

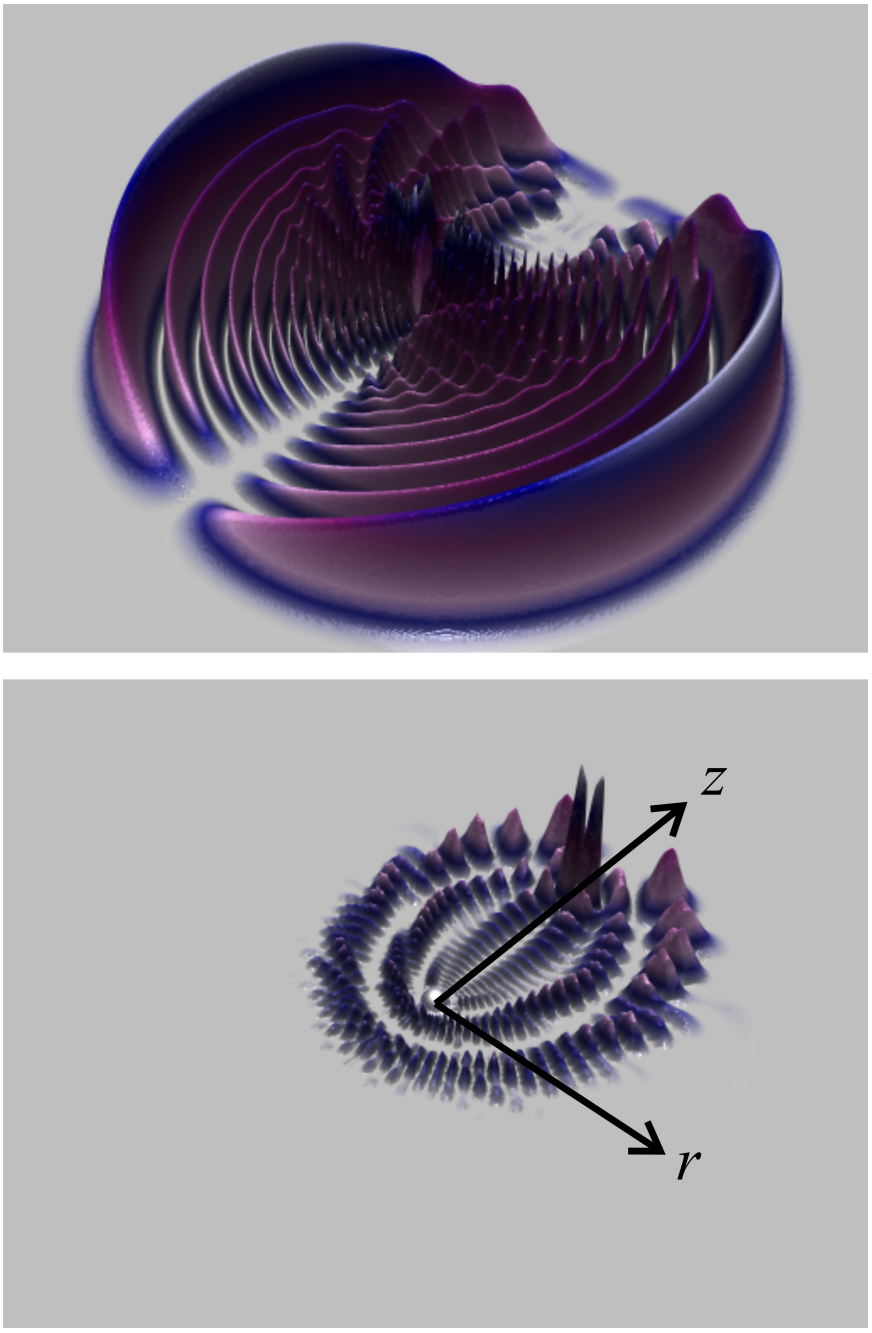

Figure 6.12: *top* Full electronic probability distribution. *bottom* Remaining probability distribution after subtracting off the parent Rydberg state contribution. The Rydberg atom core is at the origin of the cylindrical coordinate system.

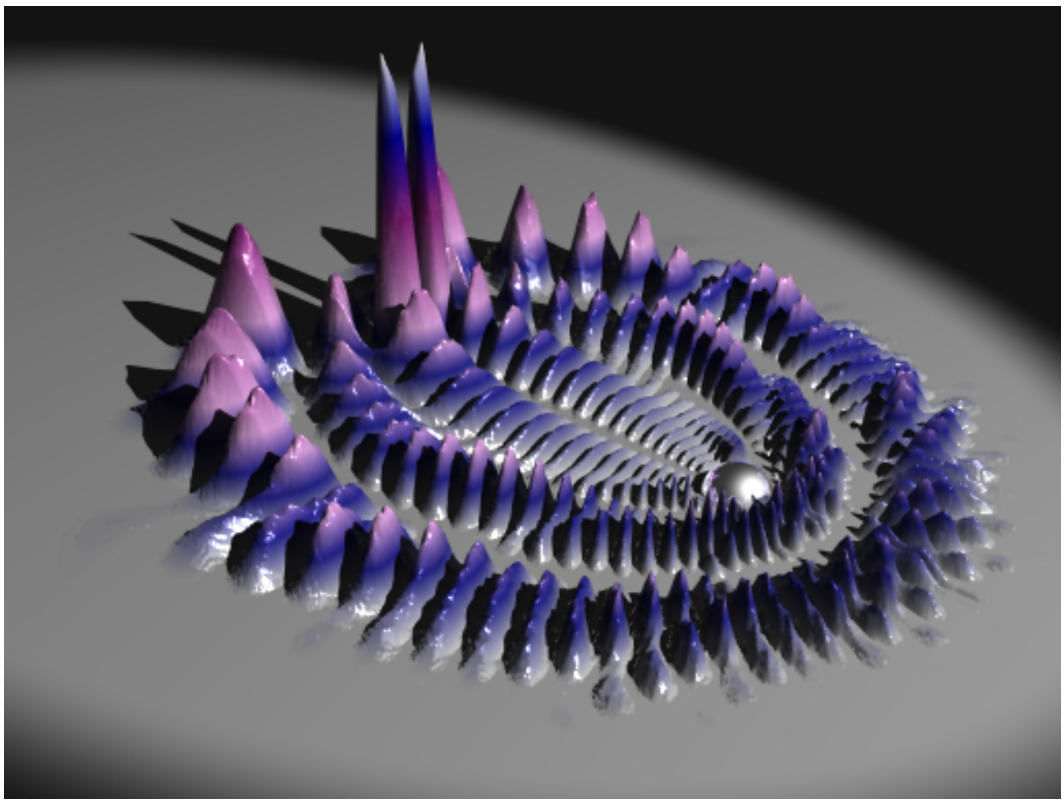

Figure 6.13: Close-up view of the ${}^3\Sigma(6S + 27G)\, M_J = \pm 1$ trilobite state near $R = 1050$ a.u. The Rydberg atom core is represented by the sphere. The peaks of the electron probability coincide with the position of the ground state atom.

A molecule with a dipole moment of ~ 35 D should exhibit a dramatic linear Stark effect. A modest electric field of 240 mV cm^{-1} should cause a measurable shift of a few MHz. To investigate this, small background electric fields were applied during excitation of the two $M_J = \pm 1$ molecular states near $n = 31$. Surprisingly, even electric fields below 100 mV cm^{-1} cause changes in the observed spectrum, see Fig. 6.14. A shift that is described by the linear Stark effect is not observed. The sign of the permanent dipole moments means that they should move to lower energies with higher electric fields. The observed peaks broaden and shift to *higher* energies. Both peaks broaden with increasing field, which is to be expected due to the large dipole moments and vanishingly small rotational constant ($B \simeq 10^{-11}$ a.u.). The small rotational constant causes broadening due to the orientation of the molecular dipole moment with respect to the applied electric field. The blue-shift of the peaks, however, is unexpected. The largest peak shifts only very slightly ~ 2 MHz, but the bluest peak shifts ~ 10 MHz to the blue before it disappears completely. The effect of the background electric field needs to be included in the theory to accurately describe the experiment. The experimental observations cannot be simply described as a linear Stark shift because the potential supporting the bound states are changing appreciably with the applied field. The experimental data suggest that a structural change to the potential wells is the dominating effect in the presence of a background electric field. This is expected to be different than the rubidium case [22] because the molecular states here have significant mixing with the degenerate hydrogenic

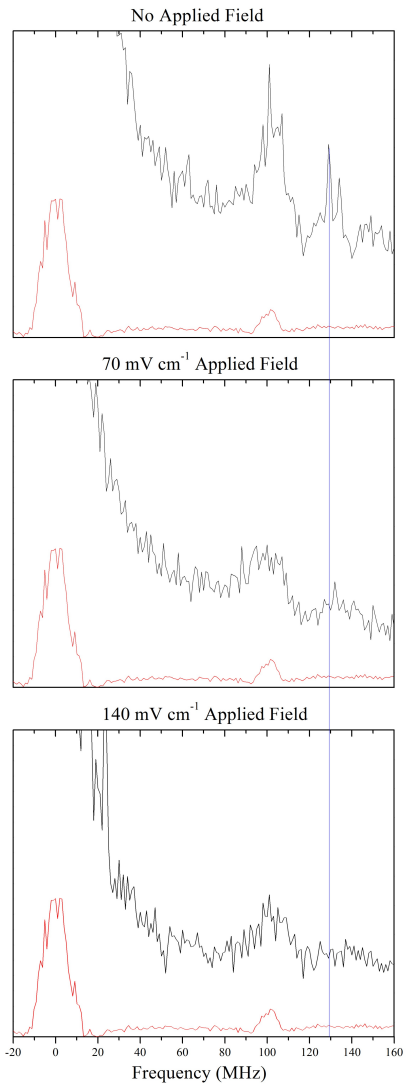

Figure 6.14: Electric field dependence of the molecular states near $n = 31$. The applied field causes significant changes in the spectra.

manifold and are the result of avoided crossings, which are sensitive to the applied electric field. As a consequence, the electric field dependence of the cesium ultralong-range molecules studied is sufficiently complicated that the details are left to a future work.

6.5 Conclusions

To summarize, cesium ultralong-range "trilobite" states were observed in an optical dipole trap and their positions with respect to the nS thresholds were accurately described with theory. The agreement with theory provides experimental evidence for the position of the p-wave e^-+ Cs resonance described in [25]. Both $M_J = \pm 1$ and $M_J = 0$ angular momentum projections were observed, in contrast to the earlier Rb trilobite like molecules observed in a magnetic trap [22]. These molecules also have different properties than those found in the earlier Rb work. The cesium states described here have significantly larger mixing of the nearby hydrogenic manifold of states due to the near-integer quantum defect of the cesium nS Rydberg states. The states are supported by potential wells appearing above the nS thresholds due to the interaction of the hydrogenic states and the nS Rydberg state, which gives rise to giant dipole moments and experimental accessibility via two-photon association. Large changes in the spectrum were observed by applying small electric fields suggesting both large dipole moments and significant structural changes to the potential wells. Also

in contrast to the Rb experiment, molecular ions were not observed suggesting a different decay mechanism.

Future questions to be addressed are to sort out the details of the behavior of these states in electric fields and understand their decay mechanisms. The discovery of spectroscopically accessible cesium trilobite states opens up a new window into these exotic molecules and will help lead to our understanding of them. Perhaps these states can be used to create ion pair states, involving the remaining Rydberg atom core and negatively charged ground state atom. Applications that exploit the giant permanent dipole moments are sure to follow.

Chapter 7

Conclusions and Future Directions

To conclude, exotic cesium trilobite states with giant permanent electric dipole moments, $\sim 20-100$ D, were observed. The positions of the molecular resonances were in agreement with calculations carried out by our collaborators at ITAMP, Harvard University. This experiment represents only the second observation of molecules bound by this unique mechanism, and the first observation in the cesium system. These exotic molecules also have the largest permanent dipole moments of any homonuclear system to date [23] and, to our knowledge, the largest permanent dipole moments of any diatomic molecule. The experiment serves as a benchmark for creating homonuclear diatomic molecules with giant permanent dipole moments and opens a window into how these strange molecules behave. Understanding how trilobite molecules are created and how they interact with background fields allows for future experiments which exploit their giant dipole moments. Furthermore, study of trilobite molecules may lead to a path for the formation of ion pair states.

The design, construction, and implementation of Zeeman slowed atomic beam was described. The design parameters were carefully considered and a Monte Carlo simulation was carried out for their optimization. The Zeeman slower, while not implemented in any experiment in this thesis, enhances the loading rate and steady-state atom number available in the MOT by ~ 1 order

of magnitude, compared to MOTs loaded from background vapor. This will become important for experiments with lower detection rates because the overall repetition rate of the experiment may be increased bye faster loading rates, longer trapping lifetimes and larger traps. An important advantage of the addition of the slowed atomic beam is the differential pumping between the MOT location and the atomic beam oven. This allows for pressures lower by nearly 2 orders of magnitude in the trapping region that will extend the lifetime of trapped atom samples. This again aids in the overall data acquisition rate, but the decrease in pressure is an absolute necessity to achieve temperatures approaching quantum degeneracy.

Perhaps the most significant technical contribution of this thesis is the addition of an optical dipole trapping system to the experiment. The dipole trap has been successfully implemented and characterized. An alignment procedure was developed to properly overlap the dipole trap and MOT to allow for proper loading. The details of the necessary additional cooling phase in the MOT were determined. Loading weaker neutral atom traps from larger traps is generally useful so the cooling techniques used here are applicable to other systems as well. The effect of the trapping field on the lifetimes of Rydberg atoms was systematically studied. In the crossed optical dipole trap configuration, a ground state density of $\sim 2 \times 10^{13}$ cm^{-3} was achieved, an increase in ~ 3 orders of magnitude from the MOT which was used in all experiments before this thesis. The increase in density is an invaluable tool for future experiments. Not only is

the experimental apparatus now sensitive to interactions on the 50 nm scale, few-body events scale as powers of the density, so the signal sensitivity to ultracold two-body events has been increased by 10^6 and that of three-body events has been increased by 10^9 ! Indeed, without this critical addition to the apparatus, trilobite molecules would not have been observable.

The future bodes well for this experiment. The experimental apparatus will most certainly be further improved. The flux of slowed atoms from the Zeeman slower can be improved with larger apertures and the addition of a dedicated slowing laser. The density and atom number of the optical dipole trap can be improved by adding lasers with higher powers and optimizing the trapping volume. A high power CO_2 laser is also available for schemes such as dimple traps, which are used in the condensation of cesium [68]. Future experiments include a closer look at cesium trilobite molecules. The decay of these molecules is a topic of recent interest because they can possibly lead to the formation of ion pair states and the cesium trilobite states were observed to decay differently than those in rubidium [22]. The study of cesium trilobite molecules may be extended by going to Rydberg states with higher principal quantum numbers. The larger orbit of the Rydberg electron guarantees that many ground state atoms lie within its orbit. The interactions are then described by electron scattering off of many ground state atoms. This system has similarities to electron scattering off of defects in semiconductors, leading to magnetic phase transitions. The dependence of the phase transitions on electron spin will be

studied with unpolarized and spin-polarized atoms.

Another exciting cesium experiment soon to be underway is the study of anisotropic interactions of high-lying Rydberg states in the presence of a background electric field. Two Rydberg atoms in high-$l \neq 0$ angular momentum states will show an observable alignment effect in the presence of a background electric field. The angular distributions can be measured by imaging the process in 3D. The detection system, at present, already has position sensitivity in the xy-plane and the third dimension may be obtained by using the time-of-flight. The capability to image processes in 3D will provide this experiment with tools necessary to study more complex processes, such as three-body recombination. Three-body recombination in this context describes the approach of three ultracold cesium atoms recombining to a diatomic molecule and excited atom.

$$\mathrm{Cs} + \mathrm{Cs} + \mathrm{Cs} \rightarrow \mathrm{Cs}^* + \mathrm{Cs}_2 \tag{7.1}$$

This process is of interest because it is the dominating loss process when the density is high, and historically inhibited Bose-Einstein condensation [68, 20, 21]. The molecules that are formed are in very high-lying vibrational states, and the experiment will determine the state-to-state differential cross-sections for the levels involved. Since most BEC experiments require the use of magnetic Feshbach resonances, the cross sections as a function of magnetic field are also of interest. The method of detection is resonant-enhanced multiphoton ionization of the molecules and significant steps have already been made to optimize detection

of photoassociated molecules. With additional improvements to the existing apparatus, the experiment will be able to exploit its full potential in studying systems of ultracold interactions and ultracold chemistry.

References

[1] T. F. Gallagher, *Rydberg Atoms*, 1st ed. (Cambridge University Press, 1994).

[2] D. Jaksch, J. I. Cirac, P. Zoller, S. L. Rolston, R. Côté, and M. D. Lukin, Phys. Rev. Lett. **85**, 2208 (2000).

[3] M. D. Lukin, M. Fleischhauer, R. Côté, L. M. Duan, D. Jaksch, J. I. Cirac, and P. Zoller, Phys. Rev. Lett. **87**, 037901 (2001).

[4] L. Isenhower, E. Urban, X. L. Zhang, A. T. Gill, T. Henage, T. A. Johnson, T. G. Walker, and M. Saffman, Phys. Rev. Lett. **104**, 010503 (2010).

[5] M. Saffman, T. G. Walker, and K. Mølmer, Rev. Mod. Phys. **82**, 2313 (2010).

[6] G. Rempe, H. Walther, and N. Klein, Phys. Rev. Lett. **58**, 353 (1987).

[7] M. Brune, E. Hagley, J. Dreyer, X. Maître, A. Maali, C. Wunderlich, J. M. Raimond, and S. Haroche, Phys. Rev. Lett. **77**, 4887 (1996).

[8] E. Hagley, X. Maître, G. Nogues, C. Wunderlich, M. Brune, J. M. Raimond, and S. Haroche, Phys. Rev. Lett. **79**, 1 (1997).

[9] A. L. d. Oliveira, M. W. Mancini, V. S. Bagnato, and L. G. Marcassa, Phys. Rev. A **65**, 031401 (2002).

[10] V. A. Nascimento, L. L. Caliri, A. L. de Oliveira, V. S. Bagnato, and L. G. Marcassa, Phys. Rev. A **74**, 054501 (2006).

[11] D. B. Branden, T. Juhasz, T. Mahlokozera, C. Vesa, R. O. Wilson, M. Zheng, A. Kortyna, and D. A. Tate, Journal of Physics B: Atomic, Molecular and Optical Physics **43**, 015002 (2010).

[12] M. Brune, F. Schmidt-Kaler, A. Maali, J. Dreyer, E. Hagley, J. M. Raimond, and S. Haroche, Phys. Rev. Lett. **76**, 1800 (1996).

[13] A. Schwettmann, J. Crawford, K. R. Overstreet, and J. P. Shaffer, Phys. Rev. A **74**, 020701 (2006).

[14] K. R. Overstreet, A. Schwettmann, J. Tallant, and J. P. Shaffer, Phys. Rev. A **76**, 011403 (2007).

[15] A. Schwettmann, K. R. Overstreet, J. Tallant, and J. P. Shaffer, Journal of Modern Optics **54**, 2551 (2007).

[16] K. R. Overstreet, A. Schwettmann, J. Tallant, D. Booth, and J. P. Shaffer, Nat. Phys. **5**, 581 (2009).

[17] H. J. Metcalf and P. van der Straten, *Laser Cooling and Trapping*, 1st ed. (Springer-Verlag New York, 1999).

[18] E. Fermi, Nouvo Cimento **11**, 157 (1934).

[19] A. Omont, J. Phys. France **38**, 1343 (1977).

[20] M. H. Anderson, J. R. Ensher, M. R. Matthews, C. E. Wieman, and E. A. Cornell, Science **269**, 198 (1995).

[21] K. B. Davis, M. O. Mewes, M. R. Andrews, N. J. van Druten, D. S. Durfee, D. M. Kurn, and W. Ketterle, Phys. Rev. Lett. **75**, 3969 (1995).

[22] V. Bendkowsky, B. Butscher, J. Nipper, J. P. Shaffer, R. Löw, and T. Pfau, Nature **458**, 1005 (2009).

[23] W. Li, T. Pohl, J. M. Rost, S. T. Rittenhouse, H. R. Sadeghpour, J. Nipper, B. Butscher, J. B. Balewski, V. Bendkowsky, R. Löw, and T. Pfau, Science **334**, 1110 (2011).

[24] C. H. Greene, A. S. Dickinson, and H. R. Sadeghpour, Phys. Rev. Lett. **85**, 2458 (2000).

[25] M. Scheer, J. Thøgersen, R. C. Bilodeau, C. A. Brodie, H. K. Haugen, H. H. Andersen, P. Kristensen, and T. Andersen, Phys. Rev. Lett. **80**, 684 (1998).

[26] T. Hänsch and A. L. Schawlow, Opt. Commun. **13**, 68 (1975).

[27] D. J. Wineland and H. Dehmelt, Bull. Am. Phys. Soc. **20**, 637 (1975).

[28] J. Dalibard and C. Cohen-Tannoudji, J. Opt. Soc. Am. B **6**, 2023 (1989).

[29] P. J. Ungar, D. S. Weiss, E. Riis, and S. Chu, J. Opt. Soc. Am. B **6**, 2058 (1989).

[30] D. S. Weiss, E. Riis, Y. Shevy, P. J. Ungar, and S. Chu, J. Opt. Soc. Am. B **6**, 2072 (1989).

[31] D. A. Steck, Cesium D Line Data, available online at http://steck.us/alkalidata, (revision 2.1.4, December 23, 2010).

[32] I. Estermann, S. N. Foner, and O. Stern, Phys. Rev. **7**, 250 (1947).

[33] G. Scoles, *Atomic and Molecular Beam Methods*, 1st ed. (Oxford University Press, New York, 1987).

[34] W. Ertmer, R. Blatt, J. L. Hall, and M. Zhu, Phys. Rev. Lett. **54**, 996 (1947).

[35] W. Ketterle, A. Martin, M. A. Joffe, and D. E. Pritchard, Phys. Rev. Lett. **69**, 2483 (1992).

[36] R. Gaggl, L. Windholz, C. Umfer, and C. Neureiter, Phys. Rev. A **49**, 1119 (1994).

[37] R. Gaggl, L. Windholz, C. Umfer, and C. Neureiter, Phys. Rev. Lett. **48**, 596 (1982).

[38] T. E. Barrett, S. W. Dapore-Schwartz, M. D. Ray, and G. P. Lafyatis, Phys. Rev. Lett. **67**, 3483 (1991).

[39] R. Grimm, M. Weidemüller, and Y. B. Ovchinnikov, Ad. At. Mol. Opt. Phys. **42**, 95 (2000).

[40] S. Chu, J. E. Bjorkholm, A. Ashkin, and A. Cable, Phys. Rev. Lett. **57**, 314 (1986).

[41] K. L. Corwin, Z.-T. Lu, C. F. Hand, R. J. Epstein, and C. E. Wieman, Appl. Opt. **37**, 3295 (1998).

[42] S. J. M. Kuppens, K. L. Corwin, K. W. Miller, T. E. Chupp, and C. E. Wieman, Phys. Rev. A **62**, 013406 (2000).

[43] C. G. Townsend, N. H. Edwards, C. J. Cooper, K. P. Zetie, C. J. Foot, A. M. Steane, P. Szriftgiser, H. Perrin, and J. Dalibard, Phys. Rev. A **52**, 1423 (1995).

[44] K. Mølmer, L. Isenhower, and M. Saffman, Journal of Physics B: Atomic, Molecular and Optical Physics **44**, 184016 (2011).

[45] J. Sedlacek, A. Schwettmann, H. Kübler, R. Löw, T. Pfau, and J. P. Shaffer, Nature Photonics *to be published* (2012).

[46] K.-H. Weber and C. J. Sansonetti, Phys. Rev. A **35**, 4650 (1987).

[47] P. Goy, J. M. Raimond, G. Vitrant, and S. Haroche, Phys. Rev. A **26**, 2733 (1982).

[48] M. Marinescu, H. R. Sadeghpour, and A. Dalgarno, Phys. Rev. A **49**, 982 (1994).

[49] F. Salvata, J. M. Fernández-Vareaa, and J. W. Williamson, Comp. Phys. Comm. **90**, 151 (1995).

[50] I. I. Beterov, I. I. Ryabtsev, D. B. Tretyakov, and V. M. Entin, Phys. Rev. A **79**, 052504 (2009).

[51] L. Schnieder, W. Meier, K. H. Welge, M. N. R. Ashfold, and C. M. Western, Journal of Chemical Physics **92**, 7027 (1990).

[52] H. Xu, N. E. Shafer-Ray, F. Merkt, D. J. Hughes, M. Springer, R. P. Tuckett, and R. N. Zare, Journal of Chemical Physics **103**, 5157 (1995).

[53] E. Vliegen, H. J. Wörner, T. P. Softley, and F. Merkt, Phys. Rev. Lett. **92**, 033005 (2004).

[54] E. Nikitin, E. Dashevskaya, J. Alnis, M. Auzinsh, E. R. I. Abraham, B. R. Furneaux, M. Keil, C. McRaven, N. Shafer-Ray, and R. Waskowsky, Phys. Rev. A **68**, 023403 (2003).

[55] T. M. Brzozowski, M. Mączyńska, M. Zawada, J. Zachorowski, and W. Gawlik, Journal of Optics B: Quantum and Semiclassical Optics **4**, 62 (2002).

[56] M. Drewsen, P. Laurent, A. Nadir, G. Santarelli, A. Clairon, Y. Castin, D. Grison, and C. Salomon, Appl. Phys. B **52**, 283 (1994).

[57] D. B. Tretyakov, I. I. Beterov, V. M. Entin, I. I. Ryabtsev, and P. L. Chapovsky, Journal of Experimental & Theoretical Physics **108**, 374 (2009).

[58] Z.-G. Feng, L.-J. Zhang, J.-M. Zhao, C.-Y. Li, and S.-T. Jia, Journal of Physics B: Atomic, Molecular and Optical Physics **42**, 145303 (2009).

[59] V. Bendkowsky, B. Butscher, J. Nipper, J. B. Balewski, J. P. Shaffer, R. Löw, T. Pfau, W. Li, J. Stanojevic, T. Pohl, and J. M. Rost, Phys. Rev. Lett. **105**, 163201 (2010).

[60] M. Saffman and T. G. Walker, Phys. Rev. A **72**, 022347 (2005).

[61] A. Gaëtan, Y. Miroshnychenko, T. Wilk, A. Chotia, M. Viteau, D. Comparat, P. Pillet, A. Browaeys, and P. Grangier, Nat. Phys. **5**, 115 (2009).

[62] I. Sobel'man, *Introduction to the theory of atomic spectra*, *International series of monographs in natural philosophy* (Pergamon Press, 1972).

[63] S. M. Farooqi, D. Tong, S. Krishnan, J. Stanojevic, Y. P. Zhang, J. R. Ensher, A. S. Estrin, C. Boisseau, R. Côté, E. E. Eyler, and P. L. Gould, Phys. Rev. Lett. **91**, 183002 (2003).

[64] C. Bahrim, U. Thumm, and I. I. Fabrikant, Journal of Physics B: Atomic, Molecular and Optical Physics **34**, L195 (2001).

[65] U. Thumm and D. W. Norcross, Phys. Rev. Lett. **67**, 3495 (1991).

[66] M. Fleischhauer, A. Imamoglu, and J. P. Marangos, Rev. Mod. Phys. **77**, 633 (2005).

[67] K. C. Younge, B. Knuffman, S. E. Anderson, and G. Raithel, Phys. Rev. Lett. **104**, 173001 (2010).

[68] T. Weber, J. Herbig, M. Mark, H.-C. Ngerl, and R. Grimm, Science **299**, 232 (2003).

[69] R. Loudon, *The Quantum Theory of Light*, 3rd ed. (Oxford University Press, 2000).

[70] S. Stenholm, *Foundations of Laser Spectroscopy*, 1st ed. (Dover, 2005).

[71] C. Cohen-Tannoudji, J. Dupont-Roc, and G. Grynberg, *Atom-Photon Interactions*, 3rd ed. (John Wiley and Sons, 1992).

Appendix A

Appendix A

A.1 Analysis of the Two-Level Atom in a Laser Field

A.1.1 Construction of the Hamiltonian

The two level system consists of a ground state $|g\rangle$, and an excited state $|e\rangle$. The energy is chosen so that the ground state is at zero energy and the states are separated by an energy $\hbar\omega_0$, see Fig. A.1. The atomic Hamiltonian may be

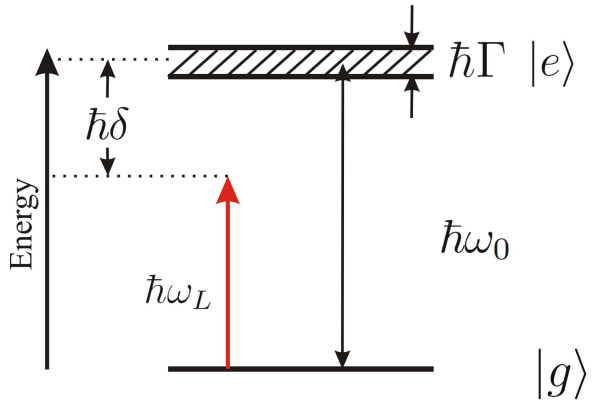

Figure A.1: The Two-level atom.

expressed as $\mathcal{H}_0 = \sum_n E_n |n\rangle \langle n|$, where $n = \{g, e\}$. This Hamiltonian in matrix form is simply

$$\mathcal{H}_0 = \begin{pmatrix} 0 & 0 \\ 0 & \hbar\omega_0 \end{pmatrix}. \tag{A.1}$$

Because the two eigenstates form a complete set, any wavefunction may be expressed as a linear combination of them, shown in Eq. A.2.

$$|\psi(t)\rangle = c_g(t)|g\rangle + c_e(t)|e\rangle \tag{A.2}$$

We now introduce a weak perturbation, $\mathcal{H}^{'}(t)$, which depends on time. The Schrödinger equation may be recast in terms of the coefficients appearing in Eq. A.2 as

$$i\hbar\frac{d}{dt}c_n(t) = \sum_m c_m(t)e^{i\omega_{nm}t}\mathcal{H}^{'}_{nm}(t) \tag{A.3}$$

where $\omega_{nm} \equiv \omega_n - \omega_m$, and $\mathcal{H}^{'}_{nm}(t) = \langle n|\,\mathcal{H}^{'}(t)|m\rangle$. We consider a perturbation that is due to the interaction with an electromagnetic wave coming from a laser that can be considered monochromatic. The electric field is given by

$$\mathbf{E}(t) = E_0\,\hat{\epsilon}\,cos(\omega_L t). \tag{A.4}$$

The photons from the laser have energy $\hbar\omega_L$, polarization $\hat{\epsilon}$, and are detuned from resonance by an amount $\delta = \omega_L - \omega_0$, see Fig. A.1.

In the dipole approximation, the form of the perturbing Hamiltonian is given by $\mathcal{H}^{'}(t) = -eE_0\hat{\epsilon}\cdot\mathbf{r}\,cos(\omega_L t)$. The matrix elements, $\mathcal{H}^{'}_{nm}$, are computed according to $\langle n|\,\mathcal{H}^{'}|m\rangle$. We see that the element $\mathcal{H}^{'}_{eg} = -eE_0\,\langle e|\,\hat{\epsilon}\cdot\mathbf{r}|g\rangle\,cos(\omega_L t)$ can be recast in a simpler form with the Rabi frequency, Ω.

$$\Omega = \frac{-eE_0}{\hbar}\,\langle e|\,\hat{\epsilon}\cdot\mathbf{r}|g\rangle \tag{A.5}$$

The coupling elements now have the form

$$\mathcal{H}^{'}_{eg} = \mathcal{H}^{'*}_{ge} = \frac{\hbar\Omega}{2}(e^{i\omega_L t} + e^{-i\omega_L t}), \tag{A.6}$$

where $cos(\omega_L t)$ has been expanded with exponentials, and Ω is taken as real. The total Hamiltonian is now $\mathcal{H} = \mathcal{H}_0 + \mathcal{H}'(t)$ and is expressed in matrix form as

$$\mathcal{H} = \hbar \begin{pmatrix} 0 & \frac{\Omega}{2}(e^{i\omega_L t} + e^{-i\omega_L t}) \\ \frac{\Omega}{2}(e^{i\omega_L t} + e^{-i\omega_L t}) & \hbar\omega_0 \end{pmatrix}. \tag{A.7}$$

A.1.2 Transformation of the Hamiltonian: The Interaction Picture

The total Hamiltonian expressed in Eq. A.7 now depends on time, where the time dependence has entered in through the perturbing Hamiltonian, $\mathcal{H}'(t)$. The initial wavefunction, $|\psi(t)\rangle$, is represented in the Schrödinger picture, where the operators are time-independent. The interaction picture moves to a frame that rotates with frequencies associated with the bare atomic eigenstates so that the motion of the new states is slow compared to the old states. These new eigenstates evolve solely due the perturbation, or interaction Hamiltonian, and so this picture is aptly named the interaction picture.

The interaction wavefunction, $|\psi_I(t)\rangle$, is obtained through a unitary transformation of the original wavefunction, $|\psi(t)\rangle$. The unitary operator is given by

$$U(t) = e^{-\frac{i}{\hbar}\mathcal{H}_0 t} \tag{A.8}$$

Expanding the exponential gives the unitary operator in matrix form.

$$U(t) = \begin{pmatrix} 1 & 0 \\ 0 & e^{-i\omega_0 t} \end{pmatrix} \tag{A.9}$$

It is easy to verify that $U^\dagger U = \mathbf{1}$. The interaction wavefunction may now be obtained by the following transformation.

$$|\psi_I(t)\rangle = U^\dagger(t)|\psi(t)\rangle \tag{A.10}$$

We may obtain the transformation of a general Hamiltonian in the Schrödinger picture, $\mathcal{H}_S$, into the corresponding interaction Hamiltonian, $\mathcal{H}_I$, by beginning with the Schrödinger equation and using the transformation in Eq. A.10 (time dependence suppressed).

$$i\hbar\frac{d}{dt}U|\psi_I\rangle = \mathcal{H}_S U|\psi_I\rangle \tag{A.11}$$

By using the chain rule and operating on the left with $U^\dagger$, we arrive at the following equation.

$$i\hbar U^\dagger\frac{d}{dt}U|\psi_I\rangle + U^\dagger U i\hbar\frac{d}{dt}|\psi_I\rangle = U^\dagger\mathcal{H}_S U|\psi_I\rangle \tag{A.12}$$

We now exploit unitarity and note $i\hbar\frac{d}{dt}|\psi_I\rangle = \mathcal{H}_I|\psi_I\rangle$ to arrive at the transformation from $\mathcal{H}_S$ to $\mathcal{H}_I$.

$$\mathcal{H}_I = U^\dagger\mathcal{H}_S U - i\hbar U^\dagger\frac{d}{dt}U \tag{A.13}$$

When we apply the transformation A.13 to the total Hamiltonian matrix, $\mathcal{H}$, we obtain time-dependent terms that depend on the detuning of the laser, $\delta = \omega_L - \omega_0$. These terms in the interaction Hamiltonian may be removed by another transformation using the unitary operator of the form

$$U_2(t) = \begin{pmatrix} 1 & 0 \\ 0 & e^{-i\delta t} \end{pmatrix}. \tag{A.14}$$

The transformed Hamiltonian, $\mathcal{H}_{tr}$, is shown below. The only approximation made to this point is the dipole approximation.

$$\mathcal{H}_{tr} = \frac{\hbar}{2}\begin{pmatrix} 0 & (1+e^{-2i\omega_L t})\Omega \\ (1+e^{2i\omega_L t})\Omega & -2\delta \end{pmatrix} \tag{A.15}$$

One can further make the rotating-wave approximation (RWA) to eliminate oscillations at $2\omega_L t$ if the laser detuning is not too large (i.e. ω_L sufficiently high). The RWA is well satisfied in most laboratory situations. This approximation leads to a $\sim 10\%$ error for 1064 nm photons from a FORT. The RWA is not valid, however, when taking into account effects from a CO_2 laser, with photon wavelength of 10.6 μm.

In the RWA, the terms $e^{\pm 2i\omega_L t}$ are set to zero due to the rapid oscillation. In situations where the RWA is satisfied, the new Hamiltonian, $\mathcal{H}_{RWA}$, is given by

$$\mathcal{H}_{RWA} = \frac{\hbar}{2}\begin{pmatrix} 0 & \Omega \\ \Omega & -2\delta \end{pmatrix}. \tag{A.16}$$

A.1.3 Dynamics

In the two-level atom, the state $|\psi(t)\rangle$ is completely described by the form shown in Eq. A.2. To find the expectation value of an observable, $\hat{A}$, one computes $\langle\psi(t)|\,\hat{A}|\psi(t)\rangle$ and arrives at the following expression

$$\langle\hat{A}\rangle(t) = \sum_{n,m} c_n^*(t)c_m(t)A_{nm}. \tag{A.17}$$

The expectation value depends on quadratic expressions of the coefficients, c^*c. Expressions of this form occur naturally when working with the density operator,

$\hat{\rho} = |\psi(t)\rangle \langle\psi(t)|$, with matrix elements in the $\{|g\rangle, |e\rangle\}$ basis given by

$$\begin{pmatrix} \rho_{gg} & \rho_{ge} \\ \rho_{eg} & \rho_{ee} \end{pmatrix} = \begin{pmatrix} |c_g|^2 & c_g c_e^* \\ c_e c_g^* & |c_e|^2 \end{pmatrix}. \tag{A.18}$$

We see that ρ_{gg} and ρ_{ee} represent the probability to be in state $|g\rangle$ or $|e\rangle$, respectively . These elements are called the *populations*, and their time dependence can be calculated using Eq. A.3. The dynamics of the density matrix elements may also be computed by noting that $\dot{\hat{\rho}} = |\dot{\psi}\rangle \langle\psi| + |\psi\rangle\langle\dot{\psi}|$, and using the Schrödinger equation to arrive at the following expression.

$$\frac{d}{dt}\hat{\rho} = -\frac{i}{\hbar}[\mathcal{H}, \hat{\rho}] \tag{A.19}$$

There is a subtle issue in calculating the populations. In the limit of zero coupling field (i.e. $\mathcal{H}'_{eg} = 0$), the populations are constant. This means if the atom finds itself in the excited state, it would remain there forever. This is clearly not the case because atoms in an excited state will spontaneously decay. The spontaneous decay is due to an interaction between the atom and the quantized vacuum field [69], and the rate of spontaneous decay, Γ, is inversely related to the lifetime of the state, $\tau = 1/\Gamma$ [70].

$$\Gamma = \frac{\mu_{eg}^2 \omega_0^3}{3\pi\epsilon_0 \hbar c^3} \tag{A.20}$$

The effect of the vacuum field is to act as a reservoir for the spontaneously emitted photon. This leads to a modification of the dynamics given in Eq. A.19 and we arrive at the so-called master equation [71].

$$\frac{d}{dt}\hat{\rho} = -\frac{i}{\hbar}[\mathcal{H}, \hat{\rho}] + \hat{\mathcal{L}}_d \tag{A.21}$$

$\hat{\mathcal{L}}_d$ is an operator that describes decay and is given by [66],

$$\hat{\mathcal{L}}_d = \sum_{i,j} \frac{\Gamma_{ij}}{2} \left(2\hat{\sigma}_{ji}\,\hat{\rho}\,\hat{\sigma}_{ij} - [\hat{\sigma}_{ii}, \hat{\rho}]\right). \tag{A.22}$$

The $\hat{\sigma}_{ij}$ are projection operators of the form $\hat{\sigma}_{ij} = |i\rangle\langle j|$, where $\{i, j\}$ are state labels. For a two-level atom $\{i, j\} \in \{g, e\}$ and $\Gamma_{eg} = \Gamma$ with all other $\Gamma_{ij} = 0$. In the $\{|g\rangle, |e\rangle\}$ basis, the decay operator becomes

$$\hat{\mathcal{L}}_d = \begin{pmatrix} \Gamma\rho_{ee} & -\frac{\Gamma}{2}\rho_{ge} \\ -\frac{\Gamma}{2}\rho_{eg} & -\Gamma\rho_{ee} \end{pmatrix}. \tag{A.23}$$

Using Eq. A.21 to calculate the dynamics with the Hamiltonian $\mathcal{H}_{RWA}$, we arrive at the optical Bloch equations.

$$\begin{aligned} \frac{d\rho_{gg}}{dt} &= \Gamma\rho_{ee} + \frac{i}{2}\Omega(\rho_{eg} - \rho_{ge}) \\ \frac{d\rho_{ee}}{dt} &= -\Gamma\rho_{ee} + \frac{i}{2}\Omega(\rho_{ge} - \rho_{eg}) \\ \frac{d\rho_{ge}}{dt} &= -\left(\frac{\Gamma}{2} + i\delta\right)\rho_{ge} + \frac{i}{2}\Omega(\rho_{ee} - \rho_{gg}) \\ \frac{d\rho_{eg}}{dt} &= -\left(\frac{\Gamma}{2} - i\delta\right)\rho_{eg} + \frac{i}{2}\Omega(\rho_{gg} - \rho_{ee}) \end{aligned} \tag{A.24}$$

Equations A.24 are, in general, difficult to solve. However, the steady-state quantities are of interest because they provide the equilibrium scattering rates for atoms that can be approximated with two-levels. The steady-state values of the density matrix elements may be computed by setting the equations A.24

equal to zero. The steady-state density matrix elements are

$$\begin{aligned}
\rho_{gg} &= 1 - \frac{\Omega^2}{\Gamma^2 + 4\delta^2 + 2\Omega^2} \\
\rho_{ee} &= \frac{\Omega^2}{\Gamma^2 + 4\delta^2 + 2\Omega^2} \\
\rho_{ge} &= \frac{(i\Gamma + 2\delta)\Omega}{\Gamma^2 + 4\delta^2 + 2\Omega^2} \\
\rho_{eg} &= \frac{(i\Gamma + 2\delta)\Omega}{\Gamma^2 + 4\delta^2 + 2\Omega^2}
\end{aligned} \tag{A.25}$$

The total photon scattering rate, Γ_p, of radiation from the atom or ensemble of atoms is then simply given by

$$\Gamma_p = \Gamma\rho_{ee} = \Gamma\frac{\Omega^2}{\Gamma^2 + 4\delta^2 + 2\Omega^2}. \tag{A.26}$$

Appendix B

B.1 Monte Carlo Simulation Code

The Zeeman slowing process in the atomic beam is simulated by a Monte Carlo simulation. The following pages reproduce the code, which should be easily manipulatable.

Zeeman Slower Simulation

In[120]:=

Initialization

In[4]:=
```
<< PhysicalConstants`
<< Units`
```

Enter atomic parameters in SI units. These are already set for Cs.

In[6]:=
```
atomicparameters =
  {kB → BoltzmannConstant[[1]], ħ → PlanckConstantReduced[[1]],
   μB → Convert[BohrMagneton, Joule / Tesla][[1]],
   m → 133 Convert[AMU, Kilogram][[1]],
   k → 2 π / (852.34727582 × 10^-9), Γ → 2 π 5.22 × 10^6};
```

Oven Speed Distribution

Enter the temperature in Kelvin. The current design is based on a ~50 °C source.

In[7]:=
```
T = 323;
```

Speed PDF

The speeds are described by the Maxwell-Boltzmann distribution.

Definition

In[8]:=
```
speedPDF[v_] = 4 π (m / (2 π kB T))^(3/2) v^2 E^(-m v^2 / (2 kB T)) /. atomicparameters;
```

Test normalization

Distribution Checks

In[9]:=
```
Integrate[speedPDF[v], {v, 0, ∞}, Assumptions → Re[m / k] > 0]
Integrate[speedPDF[v], {v, 0, 4.5}, Assumptions → Re[m / k] > 0]
Integrate[speedPDF[v], {v, 0, 110}, Assumptions → Re[m / k] > 0]
```

Out[9]= 1.

Out[10]= 8.44399×10^{-6}

Out[11]= 0.103393

In[12]:=
```
vave = Integrate[v speedPDF[v], {v, 0, ∞}]
```

Out[12]=
```
226.758
```

To find the cumulative distribution function, the effective zeroes on the sides of the distribution must be defined.

In[13]:=
```
vmin = v /. FindInstance[10^-7 < speedPDF[v] < 10^-6 ∧ speedPDF'[v] > 0, v][[1]];
vmax =
  v /. FindInstance[10^-7 < speedPDF[v] < 10^-6 ∧ speedPDF'[v] < 0 ∧ v > 0, v][[1]];
```

In[15]:=
```
vtop = v /. FindInstance[speedPDF'[v] == 0 ∧ v > 0, v][[1]] // N
```

Out[15]=
```
200.959
```

In[16]:=
```
speedPDF[vtop]
```

Out[16]=
```
0.00413126
```

In[17]:=
```
Plot[speedPDF'[v], {v, 0, vmax}]
```

Out[17]=

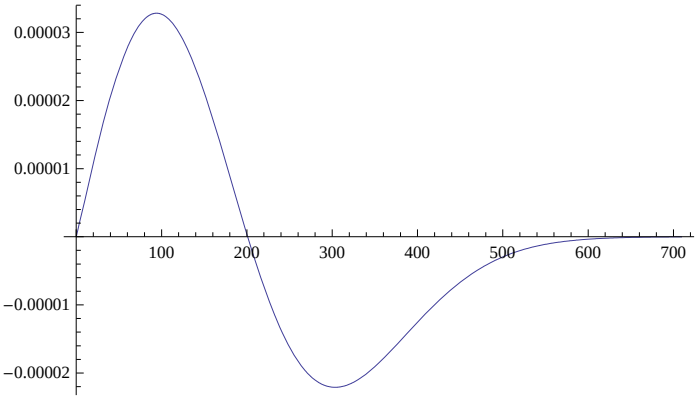

■ Speed CDF

Create a table of cdf points.

Enter the number of points

In[18]:=
```
Npoints = 10 000;
```

In[19]:=
```
cdfpoints =
  Table[{NIntegrate[speedPDF[v], {v, 0, i/Npoints vmax}], i/Npoints vmax},
   {i, 1, Npoints}];
```

Interpolate the results.

In[20]:=
```
cdf = Interpolation[cdfpoints, InterpolationOrder → 3];
```

Random velocities may now be chosen within a Maxwell-Boltzmann distribution.

Atomic Beam Collimation

This section determines the limits on the transverse velocity, given the geometry of the collimation system.
Enter the distance between the collimating holes in meters.

In[21]:=
```
dc = 0.1452372;
```

On average, the atoms will travel through the collimating region at the thermal velocity determined by the oven temperature. This dictates the average amount of time in the region.

In[22]:= $$\texttt{tc} = \frac{\texttt{dc}}{\texttt{vave}}$$

Out[22]= 0.000640494

Choose the atomic beam diameter, just before entering the slower. The design is currently based on a 1 mm diameter.

In[23]:=
```
d = 1. × 10^-3;
```

The maximum transverse velocity allowed by this geometry is given by vtmax in m/s.

In[24]:= $$\texttt{vtmax} = \frac{\texttt{d}}{2\,\texttt{tc}}$$

Out[24]= 0.780647

Random Number Generation

■ Positions

Since the axis of the Zeeman slower is the z axis, random numbers are chosen to represent the x and y coordinates. These coordinates must be within the beam diameter, d. So a uniform disk distribution of atoms is chosen for the intial spatial distribution. The initial z coordinate for the simulation will be set to zero.

This defines the uniform disk spatial distribution.

In[25]:= $$\texttt{randr} := \texttt{RandomReal}\left[\frac{\texttt{d}}{2}\right]$$

```
randang := RandomReal[2 π]
```

In[27]:=
```
randxy := {rad Cos[a], rad Sin[a]} /. {rad → randr, a → randang}
```

■ Distribution Check

In[28]:=
```
circ = Table[randxy, {i, 1, 1000}];
```

In[29]:=
```
ListPlot[circ, PlotRange → {{-.001, .001}, {-.001, .001}},
 Frame → True, FrameLabel → {"x (m)", "y (m)"}, ImageSize → 400]
```

Out[29]=

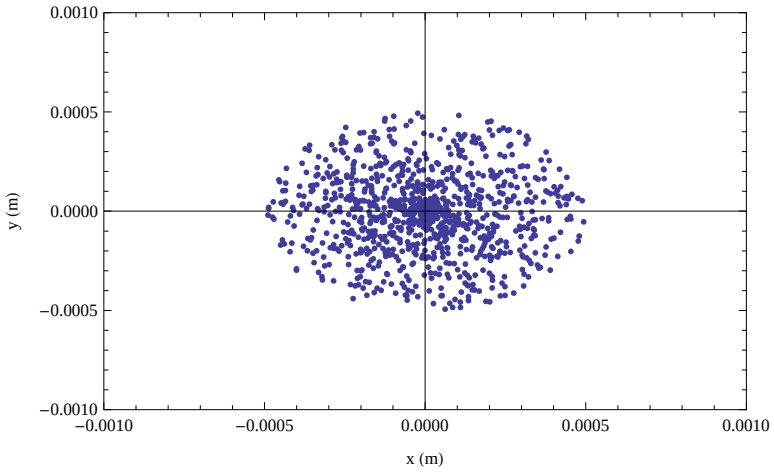

■ Velocities

The transverse speed is set by the collimation geometry (coaxial with the slower). This speed should be the maximum random speed in either the x or y direction. The z velocity component is set by the oven speed distribution.

In[30]:=
```
randvx := RandomReal[{-vtmax, vtmax}]
randvy := RandomReal[{-vtmax, vtmax}]
randvz := cdf[RandomReal[]]
```

■ Distribution Check

In[33]:=
```
speeds = Table[randvz, {i, 1, 10000}];
```

In[34]:=
```
ListPlot[speeds]
```

Out[34]=

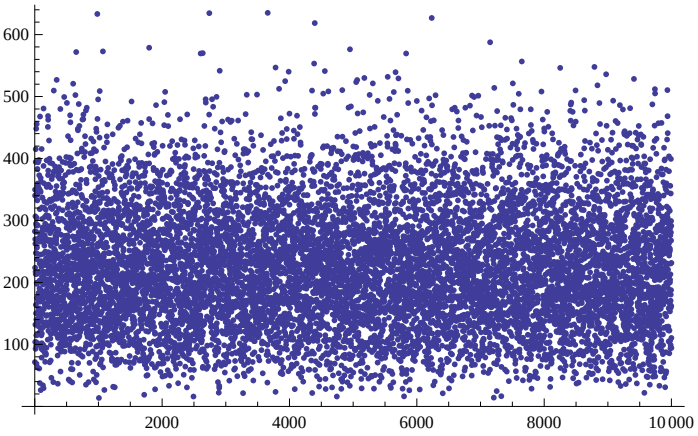

■ Binning

To make sure the distribution is Maxwell-Boltzmann, the results are binned.

In[35]:=
```
binsize = 10;
numbins = Quotient[vmax, binsize];
```

Create a table with 0's to be filled in by the binning results.

In[37]:=
```
binlist = Table[{0, 0}, {i, 1, numbins}];
```

In[38]:=
```
Do[bin = Quotient[speeds[[i]], binsize];
  binlist[[bin, 2]] ++;
  binlist[[bin, 1]] = bin binsize + binsize/2, {i, 1, Length[speeds]}] // Quiet
```

- **Plot**

In[39]:=
```
Show[ListPlot[binlist, Frame → True, FrameLabel → {"v_z (m/s)", "Number"}],
 Plot[Max[Max[binlist[[1 ;;, 2]]]/speedPDF[vtop]] speedPDF[v]], {v, 0, vmax},
 Axes → {True, False}, Frame → True], ImageSize → 400]
```

Out[39]=

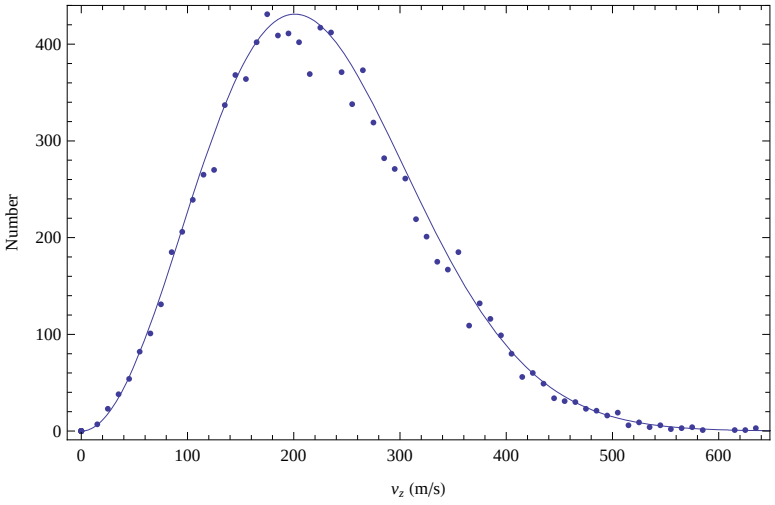

Slower Length

Set the slower length in meters. The experimental value of the slower length is ~85.5 cm.

In[40]:=
```
Clear[z0]
z0 = 0.855;
```

Magnetic Field

Initial Guess

Define the bias and the taper magnetic fields (in SI) to be used in the slower region. A good guess at the taper field is

In[42]:=
$$\text{BtguessSI}[v0\_] = \frac{\hbar\, k\, v0}{\mu B} \text{ /. atomicparameters;}$$

In[43]:=
```
BtguessGauss[v0_] = Convert[BtguessSI[v0] Tesla, Gauss];
```

In[44]:=
```
BtguessGauss[vave]
```

Out[44]=
```
190.079 Gauss
```

For T=350K, a good guess at the taper field is 200 Gauss.

Parameters

Enter the ideal magnetic field parameters. The current values have been determined by a dynamic simulation of the atomic motion that maximizes the capture rate. The values are 250 Gauss for the bias and 220 Gauss for the taper.

In[45]:=
```
Clear[Bb, Bt]
Bb = 250 Convert[Gauss, Tesla][[1]];
Bt = 220 Convert[Gauss, Tesla][[1]];
```

Function

Ideal

Define the ideal magentic field.

In[48]:=
$$\text{Bslow}[z\_] = Bb - Bt\sqrt{1 - \frac{z}{z0}}\ ;$$

Define a piecewise function to represent the magnetic field between slower and MOT.

In[49]:=
$$\text{Btot}[z\_] = \begin{cases} \text{Bslow}[z] & z < z0 \\ 0 & z > z0 \end{cases};$$

Make an interpolating function that avoids discontinuities.

In[50]:=
```
Bpoints = Table[{i, Btot[i]}, {i, 0, 10 z0, .001}];
```

In[51]:=
```
B = Interpolation[Bpoints, InterpolationOrder → 5];
```

In[52]:=
```
Plot[B[z], {z, 0, 1.01 z0}, PlotStyle → AbsoluteThickness[2]]
```

Out[52]=

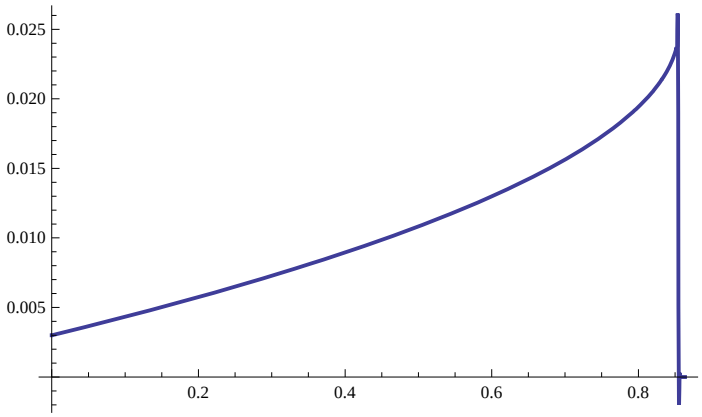

- **Wire Wrapped Calculation**

Input list with the number of turns used for wrapping the slower tube. The units of length should be one wire width. (total number of entries should be z0/w, where w is the width of the wire. **The modified newturn list may be calculated with Optimize.nb. Just copy and paste.**

In[53]:=
```
newturn = {1, 1, 1, 1, 1, 1, 1, 1, 1, 1, 1, 1, 1, 1, 1, 1, 1, 1, 1, 1, 1, 1, 1,
   1, 1, 1, 1, 1, 1, 1, 1, 1, 2, 2, 2, 2, 2, 2, 2, 2, 2, 2, 2, 2, 2, 2,
   2, 2, 2, 2, 2, 2, 2, 2, 2, 2, 2, 2, 2, 2, 2, 2, 2, 2, 2, 2, 2, 2, 2,
   2, 2, 2, 2, 2, 2, 2, 2, 2, 2, 2, 2, 2, 2, 2, 2, 2, 2, 2, 2, 2, 2, 2,
   2, 2, 2, 2, 2, 2, 3, 3, 3, 3, 3, 3, 3, 3, 3, 3, 3, 3, 3, 3, 3, 3, 3,
   3, 3, 3, 3, 3, 3, 3, 3, 3, 3, 3, 3, 3, 3, 3, 3, 3, 3, 3, 3, 3, 3, 3,
   3, 3, 3, 3, 3, 3, 3, 3, 3, 3, 3, 3, 3, 3, 3, 3, 3, 4, 4, 4, 4, 4, 4,
   4, 4, 4, 4, 4, 4, 4, 4, 4, 4, 4, 4, 4, 4, 4, 4, 4, 4, 4, 4, 4, 4, 4,
   4, 4, 4, 4, 4, 4, 4, 4, 4, 4, 4, 4, 4, 4, 4, 4, 4, 5, 5, 5, 5, 5, 5,
   5, 5, 5, 5, 5, 5, 5, 5, 5, 5, 5, 5, 5, 5, 5, 5, 5, 5, 5, 5, 5, 5, 5,
   5, 5, 5, 5, 5, 5, 5, 5, 5, 5, 6, 6, 6, 6, 6, 6, 6, 6, 6, 6, 6, 6, 6,
   6, 6, 6, 6, 6, 6, 6, 6, 6, 6, 6, 6, 6, 6, 6, 6, 6, 7, 7, 7, 7, 7, 7,
   7, 7, 7, 7, 7, 7, 7, 7, 7, 7, 7, 7, 7, 8, 8, 8, 8, 8, 8, 8, 8, 8, 8};
```

These are the parameters for the wire that will be used. These values are quoted from Alpha-Core, but the wire will likely change shape during wrapping.

This next piece of code is generates the magnetic field due to the wire wrapping configuration above.

In[54]:=
```
w = 1.0 × 2.67 × 10^-3;
t = 1.35 × 10^-3;
r = 19 × 10^-3;
sollength = .85974;
passesmod[number_] := Round[Count[newturn, x_ /; x ≥ number]];
sollengthmod[number_] := passesmod[number] w;
Bturnsmod[z_, n_] := 2 π 10^-7 (6.0/w) ( (sollength - z)/√((sollength - z)^2 + (r + (2 n - 1) t / 2)^2) +
    (z - (sollength - sollengthmod[n])) /
     (√(((sollength - sollengthmod[n]) - z)^2 + (r + (2 n - 1) t / 2)^2)) );
Btotmod[z_] = Table[Bturnsmod[z, n], {n, 1, Max[newturn]}];
Bfinalmod[z_] = Sum_{i=1}^{Max[newturn]} Btotmod[z][[i]];
Remove[t]
```

- **Plots**

This is the wrapped field vs. the ideal field.

In[64]:=
```
Plot[{B[z], Bfinalmod[z]},
 {z, .001 z0, 1.01 z0}, PlotStyle → AbsoluteThickness[4]]
```

Out[64]=

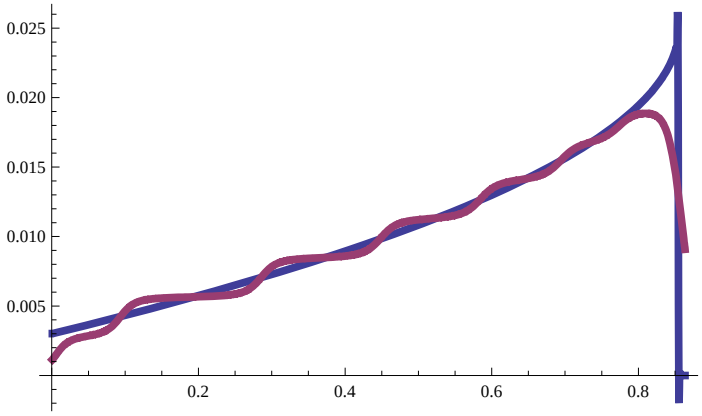

Forces

- **Radiation Pressure**
- **Laser Parameters**

The radiation pressure force is due to a single beam, whose intensity distribution is uniform across the atomic beam. Enter the laser parameters below.

In[65]:=
```
laserparameters = {s → 16, δ → -2 π 325 × 10^6};
```

■ Function

The force should be directed in the -z direction. **Fz[z,vz] is the radiation pressure force from the IDEAL field.**

In[66]:=
```
Fz[z_, vz_] := -(ħ k Γ)/2 s/(1 + s + (4/Γ^2) (δ + k vz + μB B[z]/ħ)^2) /.
  Flatten[{laserparameters, atomicparameters}];
```

In[67]:=
```
vr[z_, δ_] = (-δ/k - μB B[z]/(ħ k)) /. Flatten[{laserparameters, atomicparameters}];
```

In[68]:=
```
Plot3D[s/(1 + s + (4/Γ^2) (δ + k vz + μB B[z]/ħ)^2) /.
  Flatten[{laserparameters, atomicparameters}], {z, 0, 2},
 {vz, 20, 300}, PlotRange → Full, AxesLabel → Automatic]
```

Out[68]=

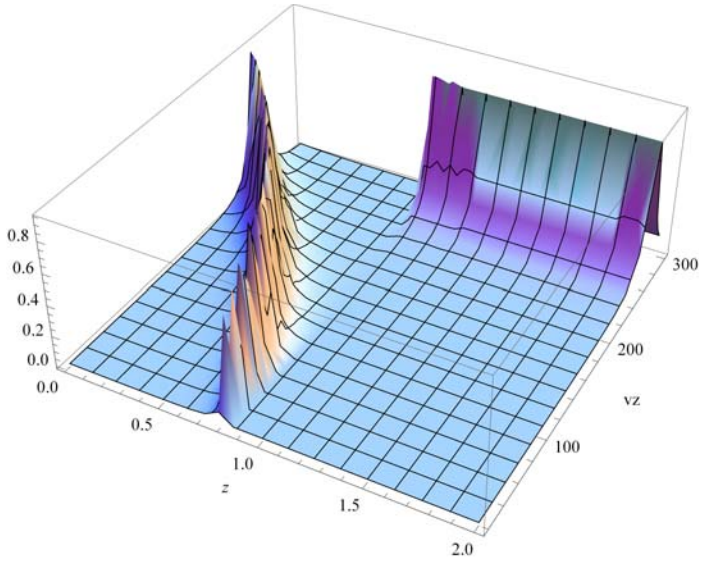

Fzmod[z,vz] is the radiation pressure force from the WIRE WRAPPED field.

In[69]:=
```
Fzmod[z_, vz_] := -(ħ k Γ)/2 s/(1 + s + (4/Γ^2) (δ + k vz + μB Bfinalmod[z]/ħ)^2) /.
  Flatten[{laserparameters, atomicparameters}];
```

■ Gravity

The coordinate system is such that gravity acts in the -y direction.

In[70]:=
```
Fy = -m * 9.8 /. atomicparameters;
```

■ Net Force

Define the net force as a vector. **Force[z,vz] is the force from the IDEAL field.**

In[71]:=
```
Force[z_, vz_] = {{0}, {Fy}, {Fz[z, vz]}} // Flatten;
```

Forcemod[z,vz] is the force from the WIRE WRAPPED field.

In[72]:=
```
Forcemod[z_, vz_] = {{0}, {Fy}, {Fzmod[z, vz]}} // Flatten;
```

Dynamics

- ## Single Atom Evolution
- ### Equations

Define the equations of motion for a single atom. **eqns is for the IDEAL field.**

In[73]:=
```
eqns = Module[{r, v, a},
  r = {{x[t]}, {y[t]}, {z[t]}} // Flatten;
  v = {{x'[t]}, {y'[t]}, {z'[t]}} // Flatten;
  a = {{x''[t]}, {y''[t]}, {z''[t]}} // Flatten;
  Table[
   133 Convert[AMU, Kilogram][[1]] a[[i]] == Force[z[t], z'[t]][[i]], {i, 1, 3}]];
```

eqnsmod is for theWIRE WRAPPED field.

In[74]:=
```
eqnsmod = Module[{r, v, a},
  r = {{x[t]}, {y[t]}, {z[t]}} // Flatten;
  v = {{x'[t]}, {y'[t]}, {z'[t]}} // Flatten;
  a = {{x''[t]}, {y''[t]}, {z''[t]}} // Flatten;
  Table[133 Convert[AMU, Kilogram][[1]] a[[i]] ==
    Forcemod[z[t], z'[t]][[i]], {i, 1, 3}]];
```

Define the initial conditions from the random numbers defined earlier.

In[75]:=
```
vave
```

Out[75]=
```
226.758
```

In[76]:=
```
initialconditions := {
    x[0] == randxy[[1]],
    y[0] == randxy[[2]],
    z[0] == 0,
    x'[0] == randvx,
    y'[0] == randvy,
    z'[0] == vave};
```

Here is where the equations of motion for a single atom are calculated. The single atom trajectory uses the average velocity defined by the oven temperature for the initial velocity, so it is representative of the majority of atoms. If these results do not look promising, don't go on to the system evolution. **To solve for the ideal vs. wire wrapped field trajectories, just change eqns to eqnsmod or vice versa.**

In[77]:=
```
sols = NDSolve[Join[eqnsmod, initialconditions], {x, y, z, x', y', z'},
    {t, 0, 0.02}, InterpolationOrder → 10, MaxSteps → 100000];
```

Define the length from the MOT to the flange where the slower will be connected.

In[78]:=
```
Lchamber = Convert[11 Inch, Meter][[1]] // N;
```

Now, the total distance that the atoms must move from the beginning of the slower to the trapping region is defined by ztot.

In[79]:=
```
ztot = z0 + Lchamber;
```

texit is the time it takes for an atom to exit the slower and tMOT is the time it takes to reach the MOT.

In[80]:=
```
texit = t /. FindRoot[Evaluate[z[t] /. sols[[1]]] == z0, {t, .005}][[1]];
tMOT = t /. FindRoot[Evaluate[z[t] /. sols[[1]]] == ztot, {t, .02}][[1]];
```

Here is the velocity of the atoms as they exit the slower. If this value is between 5 and 30 m/s, the atom will likely be trapped. (If it's below 5 m/s, it tends to miss the trap).

- **Results**

Here are the component trajectories of one atom in time. The x coordinate (blue) should be constant, the y coordinate (magenta) should fall a bit with time (due to gravity), and the z coordinate (yellow/brown) should decelerate until it reaches the end of the slower, then move with a constant velocity to the trapping region.

In[82]:=
```
Plot[{x[t] /. sols, y[t] /. sols, z[t] /. sols},
 {t, 0, .02}, PlotRange → Full, PlotStyle → AbsoluteThickness[3]]
```

Out[82]=

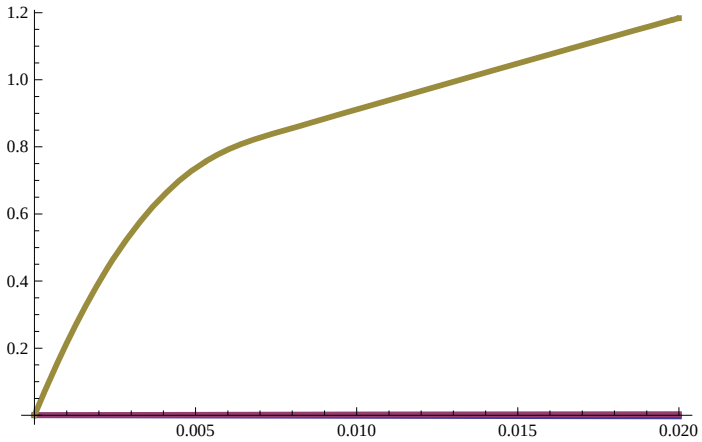

This is the final velocity.

In[83]:=
```
z'[texit] /. sols[[1]]
```

Out[83]=
```
27.9047
```

Here is the plot of the axial velocity as a function of time. There should be a constant(ish) deceleration until it becomes constant after exiting the slower.

In[84]:=
```
Plot[z'[t] /. sols, {t, 0, tMOT},
 PlotRange → Full, PlotStyle → AbsoluteThickness[3]]
```

Out[84]=

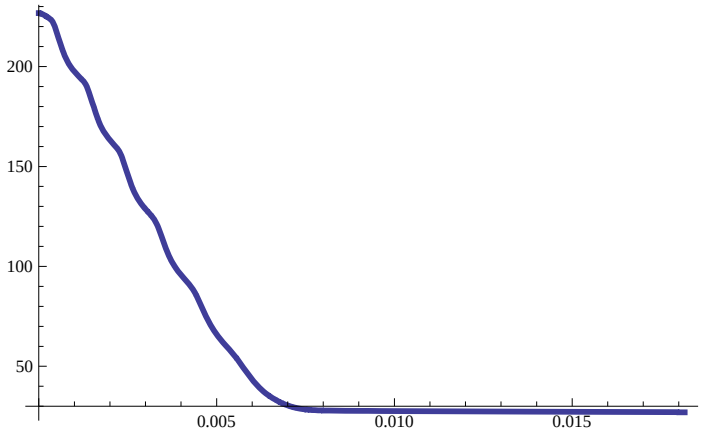

In[85]:=
```
Plot[z[t] /. sols, {t, 0, tMOT},
 PlotRange → Full, PlotStyle → AbsoluteThickness[3]]
```

Out[85]=

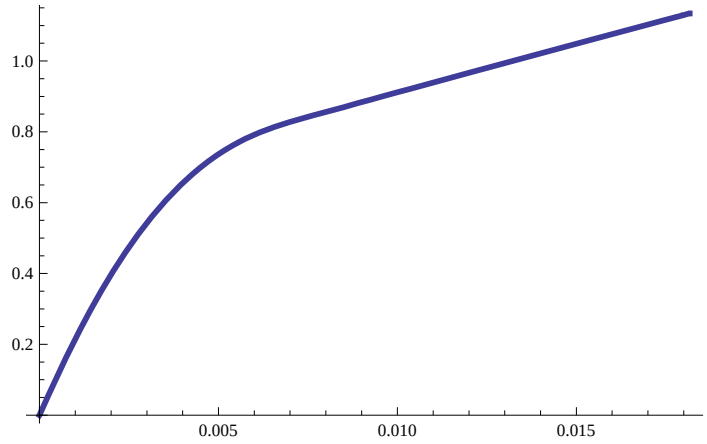

In[86]:=
```
time = Table[{z[t] /. sols[[1]], t}, {t, 0, tMOT, .0001}];
```

In[87]:=
```
timez = Interpolation[time]
```

Out[87]=
```
InterpolatingFunction[{{0., 1.13264}}, <>]
```

In[88]:=
```
z'[0] /. sols
```

Out[88]=
```
{226.758}
```

In[89]:=
```
Plot[z'[timez[x]] /. sols[[1]], {x, 0, 1.2}]
```

Out[89]=

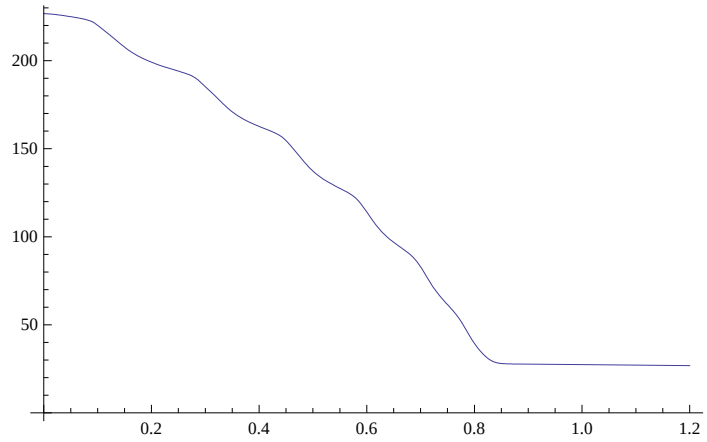

Here's the percentage of velocity lost.

In[90]:=
$$\left(\frac{z'[0] - z'[\text{texit}]}{z'[0]}\right) /. \text{sols}$$

Out[90]=
```
{0.876941}
```

■ Shifts

In[91]:=
$$\omega\text{Doppler}[l\_] = \left(\frac{2\pi}{852.35\times 10^{-9}}\right) z'[\text{timez}[l]] /. \text{sols}[[1]]$$

Out[91]=
$$7.3716\times 10^{6}\ \text{InterpolatingFunction}[\{\{0.,\ 0.02\}\},\ <>][\text{InterpolatingFunction}[\{\{0.,\ 1.13264\}\},\ <>][l]]$$

In[92]:=
$$s1 = \text{Plot}\left[\frac{\omega\text{Doppler}[x]}{2\pi 10^{6}},\ \{x,\ 0,\ 1.2\},\ \text{AxesLabel}\to\{\text{"z"},\ \text{"Doppler Shift (MHz)"}\}\right]$$

Out[92]=

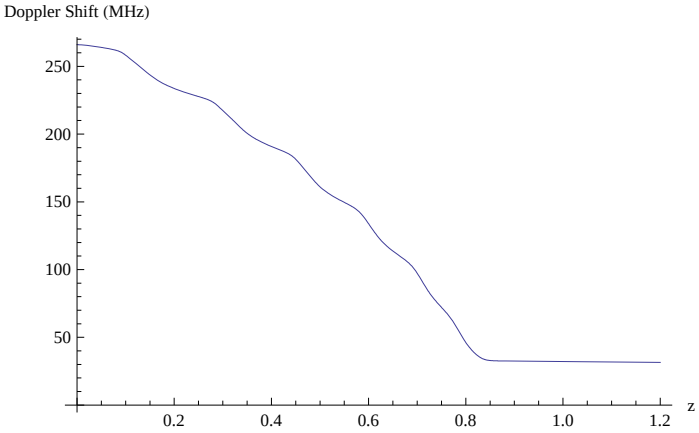

In[93]:=
$$\omega\text{Zeeman}[l\_] = \frac{\mu B}{\hbar}\ \text{Bfinalmod}[l] /.\text{atomicparameters};$$

In[94]:=
$$s2 = \text{Plot}\left[\frac{\omega\text{Zeeman}[x]}{2\pi 10^{6}},\ \{x,\ 0,\ 1.2\},\ \text{AxesLabel}\to\{\text{"z"},\ \text{"Zeeman Shift (MHz)"}\}\right]$$

Out[94]=

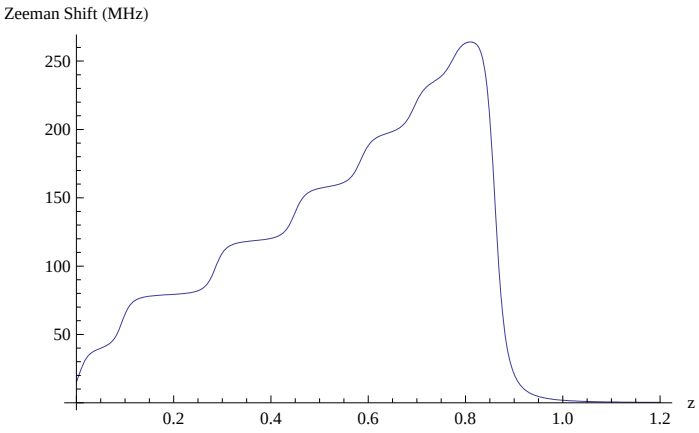

In[95]:=
```
Show[s1, s2]
```

Out[95]=

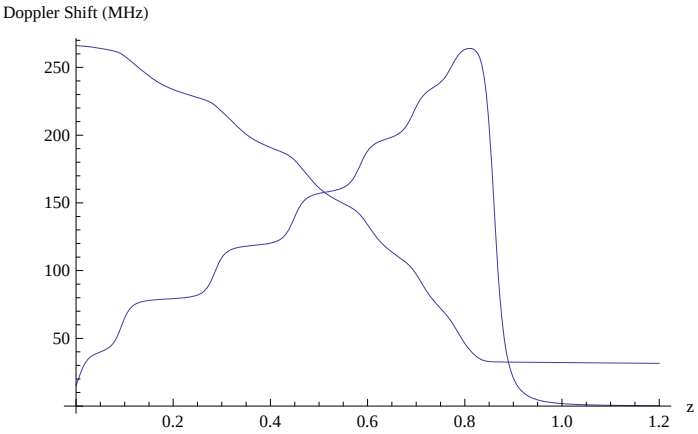

The next graph is the total detuning from resonance the atom feels as it moves down the slower.

In[96]:=
```
s3 = Plot[ωZeeman[x]/(2 π 10^6) + ωDoppler[x]/(2 π 10^6) + δ/(2 π 10^6) /. laserparameters,
  {x, 0, 1.2}, AxesLabel → {"z", "Total Detuning (MHz)"}]
```

Out[96]=

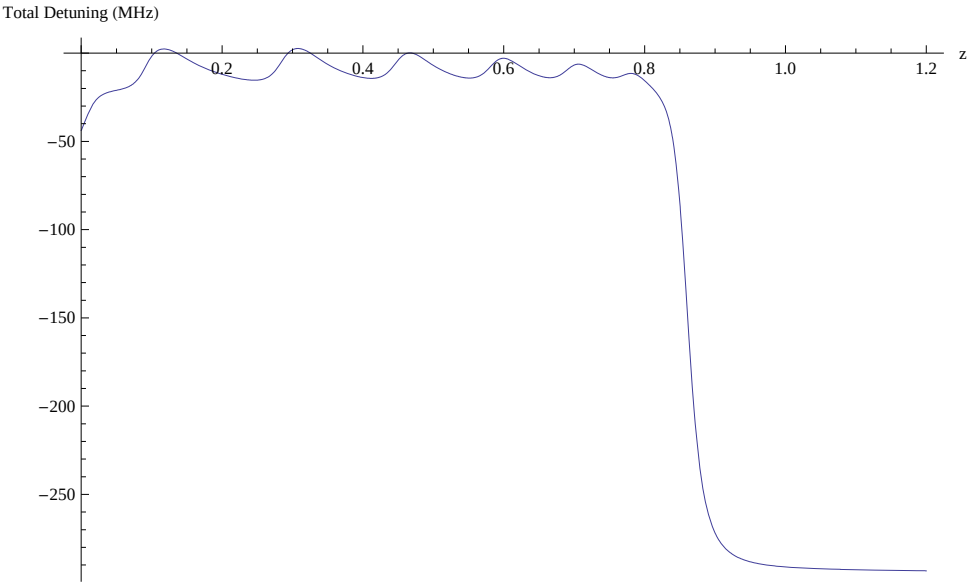

- **System Evolution**
- **Equations**

Choose the number of atoms entering the slower and enter the capture range (in meters) for the MOT. **If you want to run the ideal theoretical data,set eq=eqs. If you want to run the calculated field from the wrapping, set eq=eqsmod.**

In[97]:=
```
(*eq=eqns;*)
eq = eqnsmod;
numatoms = 1000;
rcapture = .015;
```

In[100]:=
```
evolve := Module[{positions, velocities, initialconditions, result},
  result = Table[0, {i, 1, numatoms}];
  positions = Table[Flatten[{randxy, 0}], {i, 1, numatoms}];
  velocities = Table[{randvx, randvy, randvz}, {i, 1, numatoms}];
  initialconditions = Table[
    {x[0] == positions[[i, 1]],
     y[0] == positions[[i, 2]],
     z[0] == positions[[i, 3]],
     x'[0] == velocities[[i, 1]],
     y'[0] == velocities[[i, 2]],
     z'[0] == velocities[[i, 3]]}, {i, 1, numatoms}];
  Do[
   sols = NDSolve[Join[eq, initialconditions[[i]]], {x, y, z, x', y', z'},
     {t, 0, .1}, InterpolationOrder → 3, MaxSteps → 100 000];
   tmot = t /. FindRoot[z[t] == ztot /. sols[[1]], {t, .02}];
   result[[i]] = {x[tmot], y[tmot], z[tmot], z'[tmot]} /. sols[[1]],
   {i, 1, numatoms}
  ];
  result
 ]
```

This is where the system dynamics get calculated. For 1000 atoms, this typically takes ~ 2 min. to calculate. There are normally some pesky errors here, but all errors should get automatically suppressed (eventually).

In[101]:=
```
Clear[results]
results = evolve // Quiet;
```

These four lists separate the results into different groups of atoms. Collisionresults are atoms that experience little slowing if any and will lead to the loss-rate in the trap. Slowedresults are atoms that have been slowed down, but may not be in the trapping region when they arrive at the MOT plane.

In[103]:=
```
collisionresults = Cases[results, {x_, y_, z_, vz_} /; vz > 100];
slowedresults = DeleteCases[results, {x_, y_, z_, vz_} /; vz > 35];
lostresults = Cases[results,
   {x_, y_, z_, vz_} /; z == ztot ⋀ 0 < vz < 35 ⋀ √(x^2 + y^2) > rcapture];
trappedresult = Cases[results, {x_, y_, z_, vz_} /;
    z == ztot ⋀ 0 < vz < 35 ⋀ √(x^2 + y^2) < rcapture];
```

In[107]:=
```
Length[trappedresult] + Length[lostresults] + Length[collisionresults]
```

Out[107]= 986

■ Results

Here is a plot of the spatial distribution of the atoms in the plane of the MOT. The blue dots will lead to losses, the magenta dots have been effectively slowed by the slower, but their transverse speed has taken them out of the trapping region. The yellow/brown dots will be caught in the molasses and loaded into the MOT.

In[108]:=
```
Length[slowedresults]
```

Out[108]= 575

In[109]:=
```
ListPlot[{collisionresults[[1 ;;, ;; 2]],
  slowedresults[[1 ;;, ;; 2]], trappedresult[[1 ;;, ;; 2]]},
 PlotStyle → PointSize[.015], PlotRange → {{-.02, .02}, {-.02, .02}}]
```

Out[109]=

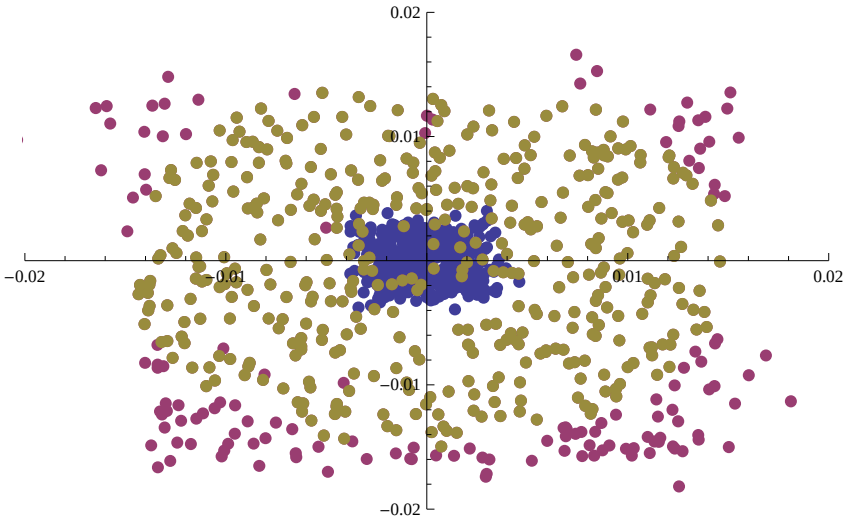

Just the slowed results here.

In[110]:=
```
ListPlot[{trappedresult[[1 ;;, ;; 2]], lostresults[[1 ;;, ;; 2]]},
 PlotRange → {{-5 rcapture, 5 rcapture}, {-5 rcapture, 5 rcapture}},
 PlotStyle → PointSize[.01]]
```

Out[110]=

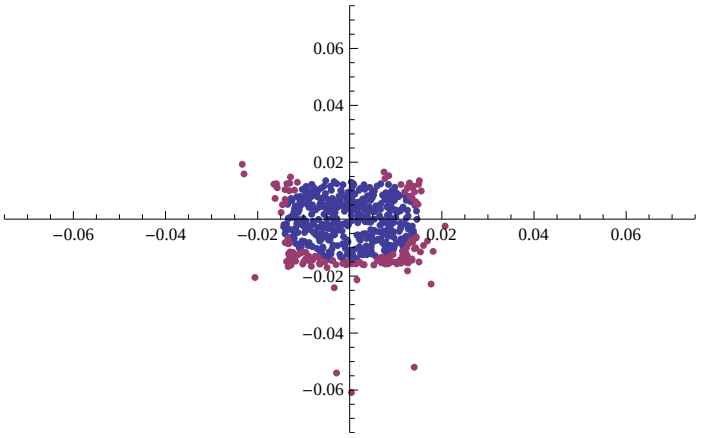

This is the percentage of atoms that get caught in the trap. It is taken relative to the number of atoms that enter the slower.

In[111]:=
```
Length[trappedresult]
---------------------- // N
Length[results]
```

Out[111]=
```
0.422
```

In[112]:=
```
Length[collisionresults]
------------------------ // N
Length[results]
```

Out[112]=
```
0.425
```

Heres an idea of the distribution. The ordered pairs are (ztot, vzfinal).

In[113]:=
```
results[[10 ;; 40, 3 ;;]]
```

Out[113]=
```
{{1.1344, 329.231}, {1.1344, 26.4912}, {1.1344, 336.396}, {1.1344, 27.0005},
 {1.1344, 26.8014}, {1.1344, 27.0005}, {1.1344, 27.0005}, {1.1344, 27.0005},
 {1.1344, 308.497}, {1.1344, 336.174}, {1.1344, 26.9488}, {1.1344, 27.0005},
 {1.1344, 27.0005}, {1.1344, 393.491}, {1.1344, -220470.},
 {1.1344, 457.427}, {1.1344, 26.9995}, {1.1344, 27.0005}, {1.1344, 303.487},
 {1.1344, 243.612}, {1.1344, 27.0005}, {1.1344, 26.9993}, {1.1344, 346.06},
 {1.1344, 249.951}, {1.1344, 239.525}, {1.1344, 24.7138}, {1.1344, 337.094},
 {1.1344, 26.969}, {1.1344, 498.881}, {1.1344, 27.0005}, {1.1344, 26.9993}}
```

In[114]:=
```
ListPlot[{lostresults[[1 ;;, ;; 2]]},
 PlotRange → {{-10 rcapture, 10 rcapture}, {-10 rcapture, 10 rcapture}},
 PlotStyle → PointSize[.01]]
```

Out[114]=

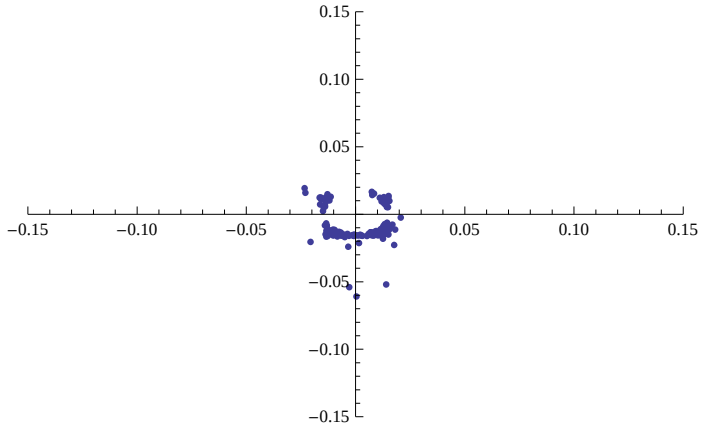

■ Binning

This section recovers the final velocity distribution of the atoms that entered the slower.

In[115]:=
```
binsizefinal = 1;
numbinsfinal = Quotient[vmax, binsizefinal];
```

In[117]:=
```
binlistfinal =
  Table[{i binsizefinal + binsizefinal/2, 0}, {i, 1, numbinsfinal - 1}];
```

In[118]:=
```
Do[bin = Quotient[results[[i, 4]], binsizefinal];
  binlistfinal[[bin, 2]] += 1;
  , {i, 1, Length[results]}] // Quiet
```

In[119]:=
```
ListPlot[binlistfinal, PlotRange → All, Joined → True,
 Frame → True, FrameLabel → {"v_z  (m/s)", "Number"},
 PlotStyle → {AbsoluteThickness[2], PointSize[.015]}]
```

Out[119]=

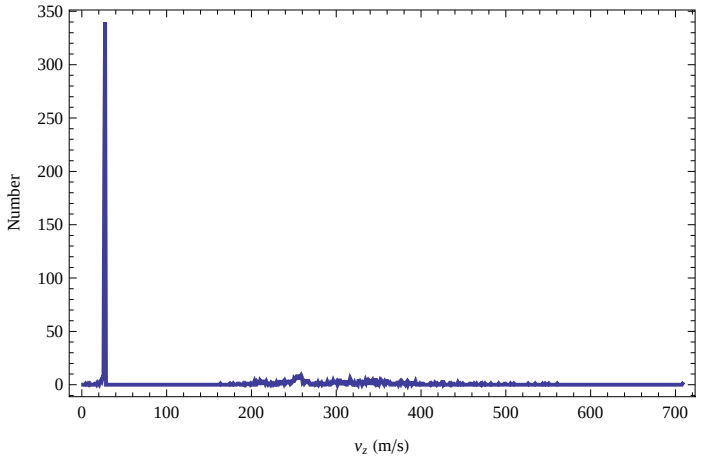

Appendix C

Appendix C

C.1 List of Publications

Below is a list of peer-reviewed publications in which I was either author or co-author. The list is in reverse chronological order.

9. J. Tallant, S. T. Rittenhouse, D. Booth, H. R. Sadeghpour and J. P. Shaffer, "Observation of blue-shifted ultralong-range Cs_2 Rydberg Molecules," Submitted to Phys. Rev. Lett., preprint available at arXiv:1205.4974.

8. J. S. Cabral, J. M. Kondo, L. F. Gonçalves, V. A. Nascimento, L. G. Marcassa, D. Booth, J. Tallant, A. Schwettmann, K. R. Overstreet, J. Sedlacek and J. P. Shaffer, "Effects of electric fields on ultracold Rydberg atom interactions," J. Phys. B: At. Mol. Opt. Phys. **44**, 184007 (2011).

7. J. Tallant, D. Booth, and J. P. Shaffer, "Photoionization rates of Cs Rydberg atoms in a 1064-nm far off- resonance trap," Phys. Rev. A **82**, 063406 (2010).

6. J. S. Cabral, J. M. Kondo, L. F. Gonalves, L. G. Marcassa, D. Booth, J. Tallant, and J.P. Shaffer, "Manipulation of quantum state transfer in cold Rydberg atom collisions ," New J. Phys. **12**, 093023 (2010).

5. K. R. Overstreet, A. Schwettmann, J. Tallant, D. Booth and J. P. Shaffer, "Observation of electric-field-induced Cs Rydberg atom macrodimers," Nature Physics **5**, 581 - 585 (2009).

4. A. Schwettmann, K. R. Overstreet, J. Tallant, and J. P. Shaffer, "Analysis of long-range Cs Rydberg potential wells," J. Mod. Opt. **54**, 2551-2562 (2007).

3. K. R. Overstreet, A. Schwettmann, J. Tallant, and J. P. Shaffer, "Photoinitiated collisions between cold Cs Rydberg atoms," Phys. Rev. A **76**, 011403(R) (2007).

2. J. Tallant, K. R. Overstreet, A. Schwettmann, and J. P. Shaffer, "Sub-Doppler magneto-optical trap temperatures measured using Rydberg tagging," Phys. Rev. A **74**, 023410 (2006).

1. K. Overstreet, P. Zabawa, J. Tallant, A. Schwettmann, and J. P. Shaffer, "Multiple scattering and the density distribution of a Cs MOT," Optics Express **13**, 9672 (2005).

C.2 Presentations

Below is a list of the presentations that I have either presented or been co-author of the presentation.

27. D. Booth, J. Tallant, A. Schwettmann, and J. P. Shaffer, "Anisotropic Rydberg Interactions," DAMOP, Anaheim, CA (2012). (Talk)

26. J. Tallant, D. Booth, and J. P. Shaffer, "Ultralong-range Cs Trilobite Molecules in a Crossed 1064 nm Dipole Trap," DAMOP, Anaheim, CA (2012). (Talk)

25. J. Tallant, D. Booth, and J. P. Shaffer, "Theoretical and Experimental evidence for the observation of trilobite states in Cs," DAMOP, Anaheim, CA (2012). (Poster)

24. J. Tallant, D. Booth, Bruno Marangoni, Luis Marcassa, and J. P. Shaffer, "Long-Range Trilobite-like Cs Molecules in a Crossed 1064 nm Dipole Trap," DAMOP, Atlanta, GA (2011). (Talk)

23. D. Booth, J. Tallant, Bruno Marangoni, Luis Marcassa, and J. P. Shaffer, "Few-body Cs Rydberg Atom Interactions in a 1064nm Dipole Trap," DAMOP, Atlanta, GA (2011). (Poster)

22. A. Schwettman, J. Sedlacek, C. Gentry, J. Tallant, and J. P. Shaffer, "Probing RF electric fields with Rydberg atoms," DAMOP, Atlanta, GA (2011). (Talk)

21. D. Booth, J. Tallant, and J. P. Shaffer, "Few-body Cs Rydberg Atom Interactions in a 1064nm Dipole Trap," International Workshop on Ultracold Rydberg Physics, Recife, Brazil (2010). (Poster)

20. J. Tallant, D. Booth, and J. P. Shaffer, "Rydberg Atom-Rydberg Atom Molecules in Background Electric Fields," International Workshop on Ultracold Rydberg Physics, Recife, Brazil (2010). (Talk)

19. J. S. Cabral, J. M. Kondo, L. F Gonçalves, L. G. Marcassa, D. Booth, J. Tallant, and J. P. Shaffer, "Manipulation of quantum state transfer in cold

Rydberg atom collisions," International Workshop on Ultracold Rydberg Physics, Recife, Brazil (2010). (Talk)

18. J. Tallant, D. Booth, A. Schwettmann, and J. P. Shaffer, "Rydberg tagging time-of-flight imaging: An improved apparatus for studying many-body processes," DAMOP, Houston, TX (2010). (Poster)

17. D. Booth, J. Tallant, A. Schwettmann, J. P. Shaffer, J. Cabral, J. Kondo, L. Gonçalves, and L. Marcassa, "Electric field effects on decay of Rb Rydberg atom pairs," DAMOP, Houston, TX (2010). (Talk)

16. A. Schwettmann, J. Tallant, D. Booth, C. E. Savell and J. P. Shaffer, "Decoherence of a Rb BEC caused by stray magnetic fields and surface effects," DAMOP, Charlottesville, VA (2009). (Poster)

15. D. Booth, A. Schwettman, J. P. Shaffer, J. S. Cabral, L. F. Gonçalvez, L. G. Marcassa, "Electric field effects on cold Rydberg atom nD-nD pair collisions," DAMOP, Charlottesville, VA (2009). (Poster)

14. A. Schwettmann, K. R. Overstreet, J. Tallant, D. Booth and J. P. Shaffer, "Observation of Cs Rydberg atom macrodimers," DAMOP, Charlottesville, VA (2009). (Talk)

13. J. Tallant, A. Schwettmann, D. W. Booth, and J. P. Shaffer, "Rydberg tagging time-of-flight imaging to study 3-body recombination," DAMOP, Charlottesville, VA (2009). (Poster)

12. A. Schwettmann, V. A. Nascimento, L. L. Caliri, J. P. Shaffer, and L. G. Marcassa, "Electric field effects on cold Rydberg atom pair excitation," DAMOP, State College, PA (2008). (Talk)

11. K. R. Overstreet, A. Schwettmann, J. Tallant, and J. P. Shaffer, "Long Range, Cold Cs Rydberg Atom-Rydberg Atom Molecules," DAMOP, State College, PA (2008). (Talk)

10. J. Tallant, K. R. Overstreet, A. Schwettmann, and J. P. Shaffer, "Dipole-Dipole Interactions in a Cold Cs Rydberg Gas," DAMOP, State College, PA (2008). (Talk)

9. A. Schwettmann, K. R. Overstreet, J. Tallant, and J. P. Shaffer, "Long-range Cs Rydberg molecules," DAMOP, Calgary, CA (2007). (Talk)

8. K. R. Overstreet, A. Schwettmann, J. Tallant, and J. P. Shaffer, "Resonant collision processes in a Cs Rydberg gas," DAMOP Calgary, CA, (2007). (Talk)

7. J. Tallant, K. R. Overstreet, A. Schwettmann, and J. P. Shaffer, "Rydberg tagging time-of-flight imaging to study ultracold collisions," DAMOP, Calgary, CA (2007). (Poster)

6. A. Schwettmann, J. Crawford, K. R. Overstreet, and J. P. Shaffer, "Rydberg Atom - Rydberg Atom Interaction Potentials," DAMOP, Knoxville, TN (2006). (Talk)

5. K. R. Overstreet, P. Zabawa, J. Tallant, A. Schwettmann, J. Crawford, and J. P. Shaffer, "Abel Inversion for study of multiple scattering in a Cs magneto-optical trap," DAMOP, Knoxville, TN (2006). (Poster)

4. A. Schwettmann, J. Franklin, K. R. Overstreet, J. Tallant, and J. P. Shaffer, "Stark Slowing Asymmetric Rotors," DAMOP, Knoxville, TN (2006). (Talk)

3. J. Tallant, K. R. Overstreet, A. Schwettmann, and J. P. Shaffer, "Temperature Measurements Using Rydberg Tagging," DAMOP, Knoxville, TN (2006). (Poster)

2. A. Schwettmann, J. Franklin, K. R. Overstreet, J. Tallant, J. Crawford, and J. P. Shaffer, "Stark Slowing Asymmetric Rotors: Weak Field Seeking States and Nonadiabatic Transitions," DAMOP, Lincoln, NE (2005). (Poster)

1. K. R. Overstreet, J. Tallant, J. Crawford, A. Schwettmann, and J. P. Shaffer, "Cold Cs Rydberg Atom Collisions: Line Shifts, Broadening and Inelastic Collisions," DAMOP, Lincoln, NE (2005). (Talk)